



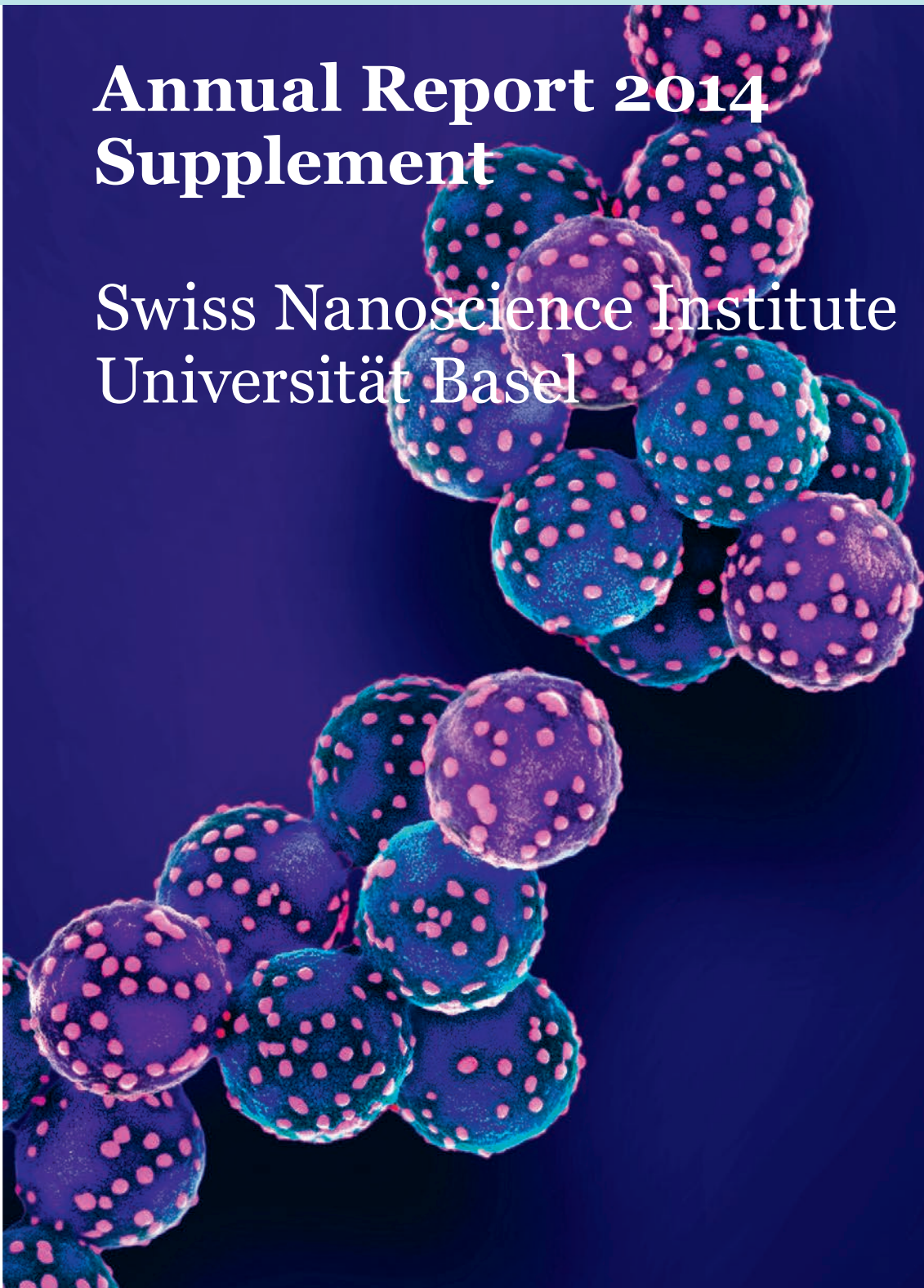
Universität
Basel

Swiss Nanoscience Institute



Annual Report 2014 Supplement

Swiss Nanoscience Institute
Universität Basel



The Swiss Nanoscience Institute is a research initiative of the Canton of Aargau and the University of Basel.

This report summarizes the work conducted within the Swiss Nanoscience Institute in 2014.

Swiss Nanoscience Institute
Klingelbergstrasse 82
CH-4056 Basel

March 2015

Cover illustration: Virus-imprinted nanoparticles (Martin Oeggerli, www.micronaut.ch)

Contents

■ SNI PhD Project Reports	2
P1201 New tools to study protein nano-crystallization	2
P1202 Nanofluidic trapping devices with increased trapping and detection performance	4
P1203 Functionalizing 4,2':6',4"-terpyridine building blocks for their staged assembly into distinct porous on-surface architectures	6
P1204 Modifying reactivity, assembly and molecule-substrate magnetic exchange coupling of square-planar complexes	8
P1205 Peering into the nuclear pore complex using a high-speed atomic force microscope	10
P1206 Hybrid spin-nanomechanics with diamond cantilevers	12
P1207 Powering-up: Using proteorhodopsin to drive a molecular Hoover	14
P1208 Scanning probe microscopy on graphene	16
P1209 Design of polymer nanoreactors with triggered activity	18
P1210 Nanowires as cantilevers: exploiting nonlinearities	20
P1211 Electron optics in encapsulated graphene	22
P1212 A low-loss, broadband optical antenna for a single color center in diamond	24
P1213 Hydrogen production based on molecular nanofactories	26
P1214 Ultracold atoms and ions on a chip	28
P1215 Nanoelectronics at ultra-low temperatures on a cryogen-free dilution refrigerator	30
P1301 Energy dissipation on moiré patterns on graphene/HOPG	32
P1302 Probing the initial steps of bacterial biofilm formation	33
P1303 Molecular muscles: A modular approach	34
P1305 Clearing the view: Highly transparent window supports for serial protein crystallography	35
P1304 Hydrogen bond formation during folding of an integral membrane protein	36
P1306 Nano-pills for mosquitoes to interrupt malaria transmission	38
P1307 First steps towards optoelectronic nanojunctions	40
P1310 Nanostructures of nuclear pore complex	41
P1308 Calixarene-based Langmuir-Blodgett film stabilization by inorganic supramolecular clips	42
■ Argovia Project Reports	44
A7.4 Low-temperature bonding of multichip modules by nano-size silver sintering	44
A7.5 Nano-capsules for active textile cooling	46
A7.6 Nanostructured surfaces for the control of polymorphism of active pharmaceutical ingredients	48
A7.7 Real-time viscosity and mass density sensors	50
A8.1 Bio-DURABLE self-cleaning paint: development of dirt repellency coatings for large surfaces	52
A8.3 Synthesis and mobility properties of new nanoparticles for colored e-readers	54
A8.7 Silver-based catalyst development	56
A9.2 Polymer emulsion-segmented electroconductive nanofibers for antistatic textile finishing	58
A9.6 Functionalized nanofiber-enhanced filter media for fine particles and heavy metal removal in flue gases	60
A9.7 Simulations and fabrication of novel 4H-SiC nano-trench MOSFET devices	62
A9.9 NANOzyme: Nanobiocatalysts based on artificial metalloenzymes	64
A9.10 Targeting selective cell response by topographical structuring of resorbable polymer implants	66
A9.12 Single-cell nanoanalytics	68
A9.15 SINAPIS – Slurry injection of nano-scale particles into implant surfaces	70

New tools to study protein nano-crystallization

Project P1201 Microfluidics to study nano-crystallization of proteins

Project Leader: T. Braun and H. Stahlberg

Collaborators: S. Arnold (SNI-PhD Student), T. Maier, T. Pfohl, and C. Padeste

Introduction

Structural biology currently experiences an accelerated technological development: First, X-ray-free electron lasers (XFEL) and, second, transmission electron microscopy (TEM) using direct electron detection (DED) cameras emerged during recent years. DED cameras now allow the structure determination of large biomolecules to atomic resolution by a single particle approach without crystallization [1]. For both techniques, new and improved sample preparation methods are required. This project aims (i) to establish an infrastructure to study protein nano-crystallization and protein aggregation *in situ* (microfluidics) and *in vivo* (cells), and, (ii) to develop new sample preparation methods on solid support for XFEL as well as TEM.

Nano-crystals are not only important for structure determination, e.g., of small proteins, but also play a crucial role in many biological processes. As an example, stereotypic spreading of protein nano-crystals through the nervous system is a hallmark of many neurodegenerative diseases [2]. To date, the spreading mechanisms are unknown, but a prion-like transmission via an intrusion of protein nanoparticles imprinting their specific folding onto native host proteins is most likely.

Setup to study *in-vitro* and *in-vivo* nano-crystallization

During the last two years we developed a versatile tool to study nano-crystallization *in cell* and in microfluidics (Fig. 1). The set-up consists of a (i) microfluidic crystallization system, a (ii) cell cultivation platform (see also project A9.12, SCellNA, p. 68) and (iii) an automated nano-crystal conditioning and hand-over device for *ex-situ* analysis by TEM and/or XFEL. The set-up is controlled by an openBEB plugin and can be automated by the openBEB macro language [3].

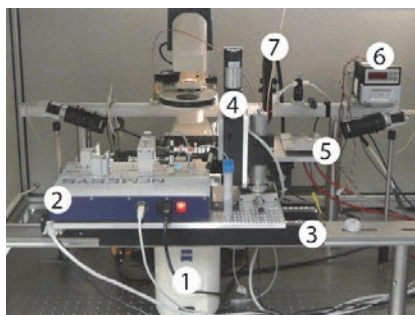


Fig. 1: Crystallization and sample preparation platform. Light microscope (1), high precision pump-system (2), X-axis motor (3), Z-axis (4), Dew-point controlled stage (5), Dew-point controller (6), Plasma generator (7).

Microfluidics to study crystallization

The principles of the microfluidic crystallization and assay platform is shown in Fig. 2.

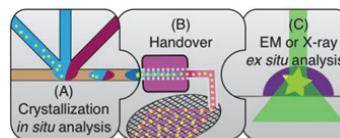


Fig. 2: Principle of microfluidic nano-crystallization platform and ex-situ analysis. A) Crystallization droplets are formed by a T-junction (see Fig. 3) and encapsulated in a two-phase microfluidic system. B) Crystallization droplets are transferred to a hand-over module consisting of a conditioning module (pink box) and a writing nozzle. This transfer module can prepare standard EM grids or new sample supports developed by the project P1305 for XFEL. C) Ex-situ analysis by TEM or XFEL.

A PDMS chip comprising a T-junction for the formation of crystallization droplets in two phase microfluidics was developed. However, an almost identical microfluidic device has been commercialized in the meantime and we now use these chips for our experiments (Fig. 3).

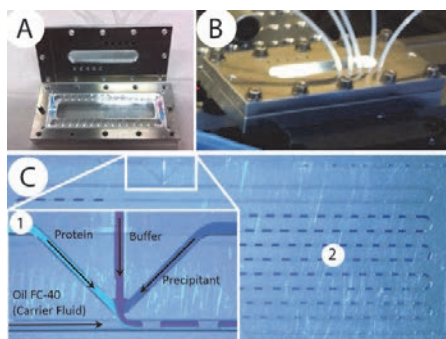


Fig. 3: Two-phase microfluidics to screen for protein aggregation and crystallization. A) Open chip holder with crystallization chip. B) Closed chip holder with connections. Chip filling can be observed with a CCD camera C) Crystallization chip seen through the camera. Inset (1): Mixing unit, where protein can be mixed with effector gradients, controlled by the change of the relative pump-speeds between the buffer and effector solutions (e.g., precipitant) inlets. The crystallization droplets are encapsulated in a fluorinated carrier oil. (2) Linear gradient of a dye (effector) in the crystallization unit.

First crystallization results looked promising. *In-situ* analysis by light-microscopy (LM) is feasible. Fig. 4 shows lysozyme crystals imaged by bright-field light-microscopy and two photon excited fluorescence (UV-TPEF) microscopy. Limitations we observed: (i) after crystal formation, the droplets are difficult to extract for subsequent *ex-situ* analysis (hand-over, Fig. 6); (ii) the chip material is birefringent, limiting *in-situ* analysis; (iii) Difficulties to establish a coordi-

nate system on the chip for subsequent comparison of the *in-situ* and *ex-situ* analysis. Therefore, we currently experiment with a new chip design to overcome these limitations.

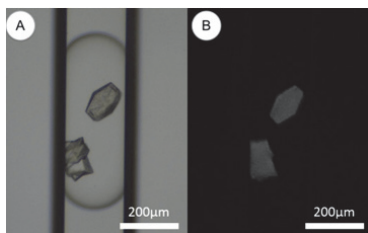


Fig. 4: In-situ visualization of lysozyme crystals in a crystallization droplet (around 20 nl) surrounded by carrier oil. A) bright-field LM and B) by UV-TPEF LM. The latter visualizes the intrinsic fluorescence present in proteins by the aromatic rings. It uses two photons at 532 nm for excitation and measures fluorescence between 340 and 400 nm. The protein concentration in crystals is higher than in the surrounding solution. Note, that nano-crystals are seen as diffuse background.

Studying aggregation of neurodegenerative protein assemblies *in situ* and *in cell*

We now use the crystallization set-up presented in Fig. 3 to study protein aggregation of α -synuclein, a major player in the progression of the Parkinson's disease. α -Synuclein builds regular aggregates in the form of filaments. Preliminary tests indicate that we can use second-order nonlinear optical imaging [4] of the chiral filaments to detect the formation of the nano-crystals by optical means.

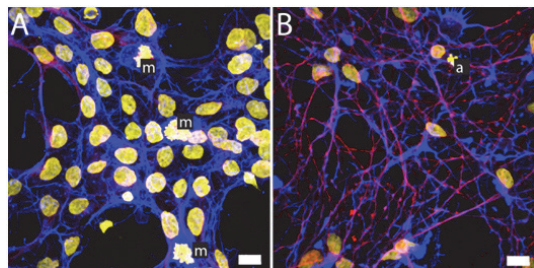


Fig. 5: Fluorescence labeling of LUHMES cells. A) *in proliferation state*, B) *differentiated (6 days)*. Blue: Actin filament (Alexa Fluor® 647 Phalloidin); yellow: dsDNA (DAPI); red: Tubulin Beta III (immunofluorescence with TUJ rabbit and antirabbit). Condensed, mitotic DNA is denoted by an (m); (a) marks DNA of cells undergoing apoptosis. Note that no mitotic cells were observed after differentiation. Scale bar: 10 μ m.

α -Synuclein nano-crystals can spread from cell to cell by a prion-like mechanism. Small protein aggregates (proto-filaments) are suspected to be the "infectious" agent acting as seeds. We use a model cell line of dopaminergic neuron-like cells (LUnd Human MESencephalic or LUHMES) to study this cell-to-cell spreading. These conditionally immortalized cells can be differentiated to dopaminergic "neurons", similar to the ones affected by the Parkinson's disease (Fig. 5). Subsequent, the LUHMES cells can be seeded with fragments of α -synuclein to "infect" the cells. *In-cell* nano-crystal formation is

then studied by visual proteomics (see Argovia project A9.12, SCellNA, p. 68).

Sample conditioning and hand-over

Recently, we developed a hand-over system connecting microfluidics and EM [5]. The same conditioning method can be used to prepare nanocrystals embedded in sugar (trehalose, Fig. 6). However, the set-up used in Fig. 6 consumed large sample volumes in the μ l range. The new device (Fig. 1) uses the same nozzle for sample uptake and dispensing and can handle volumes as small as 1 nl [6]. Unfortunately, employing a conditioning unit with these small volumes introduces significant sample loss by unspecific adsorption of the analyte. This problem can be solved by cryo-preparation methods, also enabling high-resolution EM. We developed and integrated a new cryo-preparation method in our set-up to prepare 5 nl samples.

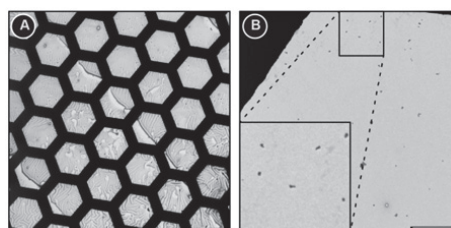


Fig. 6: Sample conditioning and hand-over module to immobilize nano-crystals on thin carbon films suitable for EM. The sample was conditioned using a micro-dialysis module to desalt the sample and add trehalose sugar for structural preservation. A) First writing test of nano-crystals in trehalose. The written stripes are visible. Scale bar: 200 μ m. B) Enlarged regions reveal individual and clustered nano-crystals (black dots). Scale bar: 20 μ m. The inset shows a 2.5x enlargement.

Involved scientists: Stefan Arnold, Jan Burri, Andrej Bieri, Philipp Fischer, Rosmarie Sütterlin (C-CINA, Biozentrum). Nadia Linda Opara (PSI), Prof. Marcel Leist (Universität Konstanz, Germany).

References for Project P1201:

- [1] W. Kühlbrandt, "The resolution revolution", *Science* **343**, 1443 (2014)
- [2] M. Costanzo and C. Zurzolo. "The cell biology of prion-like spread of protein aggregates: mechanisms and implication in neurodegeneration". *Biochem. J.* **452**, 1 (2013)
- [3] C. Ramakrishnan *et al.*, "openBEB: open biological experiment browser for correlative measurements". *BMC Bioinformatics* **15**, 84 (2014)
- [4] D. J. Kissick, D. Wanapun and G. J. Simpson, "Second-order nonlinear optical imaging of chiral crystals", *Annu. Rev. Analyt. Chem.* **4**, 419 (2011)
- [5] S. Kemmerling *et al.* "Connecting μ -fluidics to electron microscopy", *J. Struct. Biol.* **177**, 128 (2012)
- [6] S. A. Arnold, S. Kemmerling *et al.*, "Single-cell lysis for visual analysis by electron microscopy", *J. Struct. Biol.* **183**, 467 (2013)

Nanofluidic trapping devices with increased trapping and detection performance

Project P1202 Electrostatic Nanotrapping for Single-Macromolecule Analysis

Project Leader: Y. Ekinici and T. Pfohl

Collaborators: M. Gerspach (SNI-PhD Student) and N. Mojarad

Contact-free trapping of nano-objects in solution is of great scientific interest in various fields. Although several methods have been developed, such as optical and magnetic tweezers, stable and high throughput trapping of nanometer-sized particles in a straightforward manner remains challenging. One method of trapping and detecting objects smaller than 100 nm is geometry induced electrostatic (GIE) trapping [1]. In GIE trapping, negatively charged nano-objects are confined in a nanofluidic system that hosts topographically modified surfaces, resulting in electrostatic potential wells (Fig. 1). For detecting trapped nano-objects, we use interferometric scattering detection (iSCAT), a method that significantly increases the signal-to-noise ratio in comparison to other imaging methods that are based on detecting only the signal scattered by the nano-object [2].

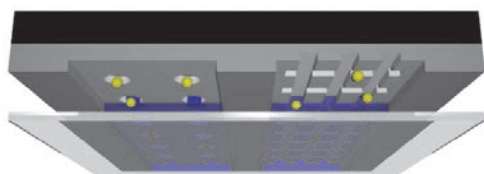


Fig. 1: Schematic of a geometry-induced electrostatic trapping device. Nano-objects are trapped within the pockets and grooves of the micro-channels.

Current GIE trapping devices are fabricated on silicon dioxide substrates using e-beam lithography and top-down nanofabrication (Fig. 2A). The channels etched into SiO₂ are tens of micrometers in width and a few hundred nanometers in height. Within these channels, nanopockets of 100-500 nm in diameter are etched in a second step about 100 nm deep into the channels. The device is finally bound to a cover glass to seal the fluidic channels and provide optical access.

When a water droplet is placed at the ends of the channels, the channels are easily filled by capillary forces. When exposed to water, the channel walls get negatively charged due to the dissociation of hydrogen ions of the silicon dioxide surface. Negatively charged nano-objects in the micro-channels experience a higher repulsion from the walls (case II in Fig 2B) all over the channel than within the smaller pockets (I) where they are pushed into these and are trapped for several milliseconds to minutes.

Towards trapping of smaller nano-objects and biomolecules

As reported in the SNI Annual Report 2013, stable trapping of 80 nm gold particles for several seconds was achieved. For trapping smaller gold particles carrying fewer charges, the trap strength of the devices has to be increased. This can be achieved by increasing the surface potential of the channel walls or by fabricating thinner micro-channels. Our current goal is to push GIE trapping technology for smaller nano-objects by fabricating thinner channels. Several challenges exist when reducing the channel height, such as collapsing of the micro-channels. By fabricating GIE trapping devices with channel heights down to 95 nm, trapping of 40 nm gold nanoparticles could be achieved.

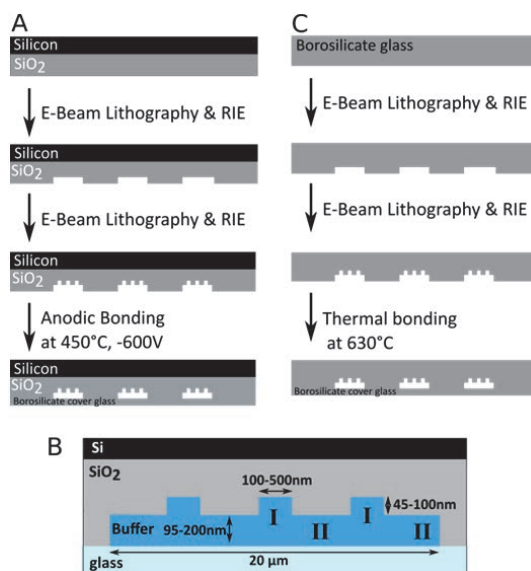


Fig. 2: A) Fabrication steps of current silicon-based GIE trapping devices, B) Cross section of the device, where the distance between the charged surfaces defines the potential well of the charged nano-objects in solution, C) Fabrication steps of new generation glass-based GIE trapping devices for higher contrast in the optical detection of nano-objects.

Reducing the channel height of the micro-channels becomes especially important for our future studies, i.e. trapping of biomolecules. By nature, biomolecules are stable and functional in physiological salt concentrations. Increasing the salt concentration of the solution leads to screening of the surface charges by free counter ions. Therefore, the traps become looser and the residence times, the average time a particle dwells in a trap, become shorter. This is shown in Fig. 3 for 60 nm gold particles trapped in a chip with a channel height of 160 nm.

For a low salt concentration of < 0.05 mmol, a mean residence time of 3.10 s is measured. If the salt concentration is increased to 0.1 and 1 mmol NaCl solution, the residence time of the 60 nm gold particles is decreased to 0.44 s and 0.047 s, respectively. By fabricating thinner channels of 130 nm channel height, the residence time can be increased to 19.5 s at a concentration of 1 mmol NaCl solution. For lower salt concentration, stable trapping of single 60 nm gold particles is increased to about 180 s at 0.1 mmol and even more than 180 s at 0.02 mmol NaCl solution.

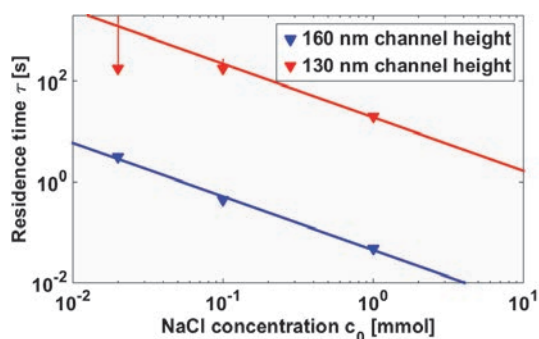


Fig. 3: Concentration and channel height dependent residence times of 60 nm gold particles trapped in pockets of 200 nm diameter.

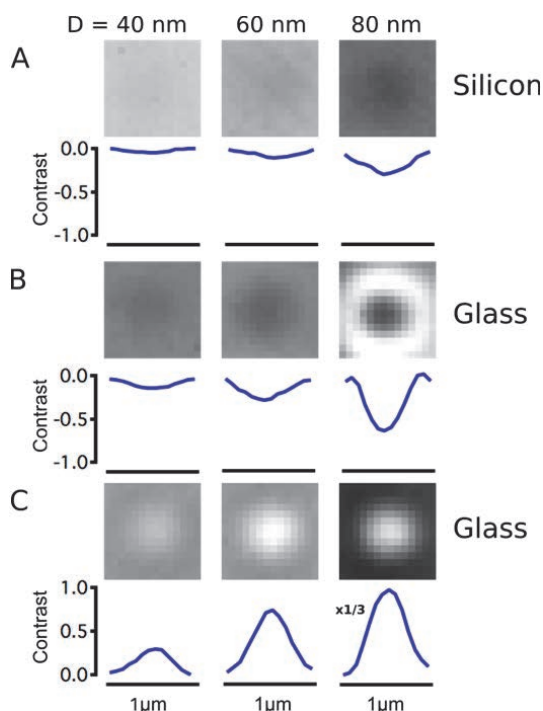


Fig. 4: iSCAT images of freely moving 40, 60 and 80 nm gold particles and plotted contrast in A) conventional silicon-based devices, B) glass-based devices with negative contrast, C) glass-based devices with positive contrast. In C) the contrast of the 80 nm gold particle was multiplied by 1/3 for better visualization.

Glass-based GIE trapping devices for higher contrast

In conventional devices made on SiO_2 grown on silicon, gold nanoparticles smaller than 60 nm are very difficult to detect due to the background noise caused by the high reflection of the Si-SiO₂ interface as seen in Fig. 4A. If the laser power is increased to gain a higher signal, overexposure of the image and loss of contrast is observed.

To overcome this limit, we developed new functional GIE trapping devices fabricated from glass substrate using thermal bonding (Fig. 2C) [3]. Due to the reduced reflection at the water-glass interface compared to the conventional silicon-based devices, higher incident laser power can be used to image the nano-objects resulting in higher contrast of the gold nanoparticles (Fig. 4B and C). Comparing the absolute contrast of the 80 nm gold particles in the glass-based devices with the 80 nm gold particles in the Si-based devices, an increased contrast by a factor of 14 was achieved. In Fig. 5, stable trapping of 60 nm gold particles with high contrast in a glass-based device in pockets of 100 nm diameter can be observed.

Thus, glass-based GIE trapping devices enable the detection of much smaller trapped nanoparticles and can also be extended to other nanofluidic systems in our future studies.

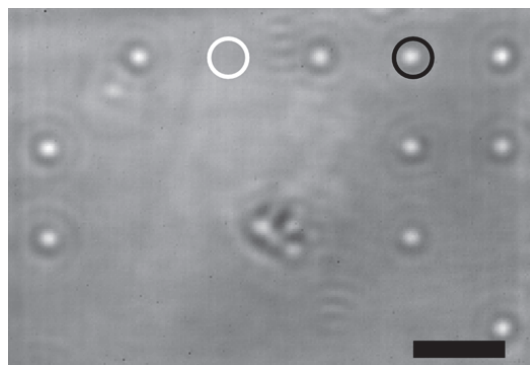


Fig. 5: iSCAT image of 60 nm gold particles trapped in a new generation glass-based GIE trapping device with a channel height of 135 nm. The particles were trapped in 100 nm pockets at low salt concentration. The black circle highlights a trapped particle whereas the white circle highlights an unoccupied pocket. The scale bar equals 3 μm .

References for Project P1202:

- [1] M. Krishnan, N. Mojarad, P. Kukura and V. Sandoghdar "Geometry-induced electrostatic trapping of nanometric objects in a fluid", *Nature* **467**, 692 (2010)
- [2] J. Ortega-Arroyo, P. Kukura, "Interferometric scattering microscopy (iSCAT): new frontiers in ultrafast and ultrasensitive optical microscopy", *Phys. Chem.* **14**, 15625 (2012)
- [3] M. A. Gerspach, N. Mojarad, Y. Ekinici and T. Pfohl, *Microelectron. Eng.*, submitted

Functionalizing 4,2':6',4"-terpyridine building blocks for their staged assembly into distinct porous on-surface architectures

Project P1203 On-surface covalent assembly of coordination polymers with integrated read and write functions

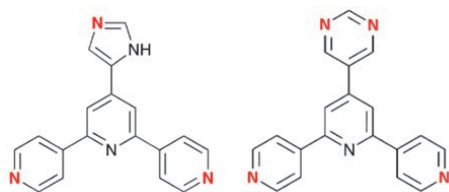
Project Leader: C.E. Housecroft and E.C. Constable

Collaborators: T. Nijs (SNI-PhD Student), Th. Jung, S. Fatayer, A. Wäckerlin, S. Nowakowska, A. Ahsan, F. J. Malzner, Y. M. Klein, and S. Vujovic

Introduction

Structural design provides one of the keys for the control of chemical reactions in general, and in particular for catalysis. Tunable scaffold architectures such as 'metal organic frameworks' (MOFs) and the 2D 'surface metal organic networks' (SurfMOFs) offer themselves for preparing highly functional architectures for performing biochemical processes such as light harvesting or site and shape selective chemical reactions [1,2]. In this work, we investigate the structure and the assembly mechanisms of surface-supported assemblies of different dimensionality using building blocks comprising different linker groups which can be activated in stages.

Here, we present a study on the self-organization of 4,2':6',4"-terpyridine derivatives on metallic single crystal substrates. Specifically, we investigated the imidazole functionalized **1** and the pyrimidine functionalized **2** (see scheme 1) [3,4]. In contrast to the well-established chelating 2,2':6',2"-terpyridines, these terpyridines possess inherent design features to facilitate their metal coordination through the N atoms.



Scheme 1: Imidazole **1** and pyrimidine **2** functionalized 4,2':6',4"-terpyridines.

Binding motif change

Deposition of **1** on Au(111) results in the formation of an extended 6-fold nanoporous hydrogen bonded network exhibiting a regular pore size of 1.4 nm. High-resolution STM micrographs recorded at 5 K show the presence of dimeric building blocks in the form of 2 molecules rotated by 180° towards each other (see green rectangle in Fig. 1a). Upon Cu-adatom supply, the intermolecular binding motif changes characteristically: the hexagonal H-bonded network transforms to Cu-coordinated heterocyclic chains as depicted by STM and evidenced by the X-ray photoelectron spectroscopy (XPS) data presented in table 1. The heterocyclic chains contain 4, 5 and 6 membered rings in irregular arrangement and follow the fcc domains of the Au(111)(22x√3)

reconstruction (Fig. 1b). Fig. 1c shows a tentative model of the different macrocycles.

XPS	-N= [eV]	-NH- [eV]
H-bonded	398.4	399.6
Cu-coord.	399.0	399.9

Table 1: XPS data of **1** on Au(111) show a clear increase of the binding energy upon metal coordination.

1 on Cu(111) – role of substrate

By changing the substrate from Au(111) to Cu(111) and depositing the same molecule **1** on samples held at room temperature, periodic hexagonal patterns appear exhibiting a similar albeit different arrangement (see green rectangle denoting a dimer in Fig. 1a vs. 1d). Notably, the distance between the dimeric building blocks is increased on Cu(111), possibly due to ligating Cu adatoms. XPS measurements which reveal the composition of this intermolecular binding motif are planned. On the Cu(111) substrate, the 2D packing density of the molecules increases and the network periodicity decreases.

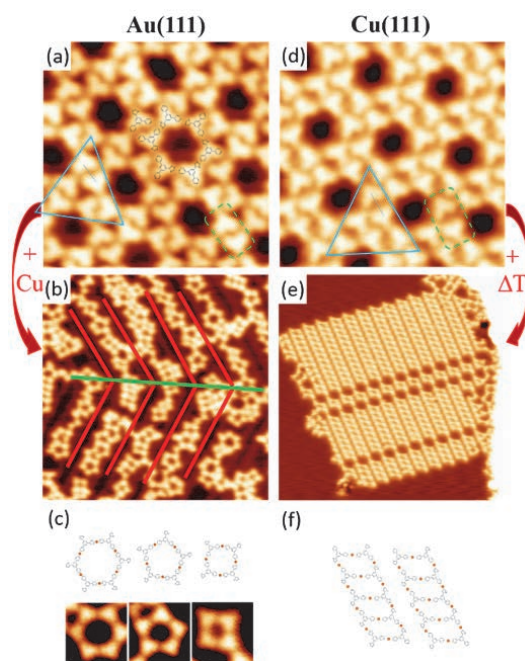


Fig. 1: Comparison of the self-assembly of **1** on Au(111) vs Cu(111). (a) Extended hydrogen-bonded network with superimposed molecular scheme (10x10 nm²). (b) The Cu-

coordinated assembly of **1** on Au(111) arranges irregular heterocycles in chains following the fcc domains of the herringbone reconstruction (red highlight)(40x40 nm²). (c) Schemes and STM micrographs of the resulting differently numbered macrocycles as they can be recognized in b. (d) Extended nanoporous network of **1** on Cu(111) (10x10 nm²). (e) Metal coordinated self-assembly obtained by annealing of d (40x40 nm²). (f) Tentative structural assignment of the on-surface coordination polymer formed after thermal release of Cu-adatoms.

Annealing of this network phase of **1** on Cu(111) supplies Cu-adatoms by thermal release from kink and step edge sites and is expected to maximize Cu coordination. The symmetry of the now even more compact adlayer becomes rectangular. A regular double row pattern (Fig. 1e) which is interrupted by line defects occurs. Note the higher uniformity in comparison to the patterns formed by **1** after annealing on Au(111). Fig. 1f represents the tentative model of this assembly. Further in-depth investigations need to be undertaken to analyze the degree of Cu coordination for **1** on Cu(111) before and after annealing.

2 on Au(111) – role of ligand

The importance of the chemical functionalization in on-surface supramolecular and coordination arrangements is here studied by replacing the imidazole functionalization **1** by the pyrimidine **2**. On Au(111), the nanoporous network observed for the imidazole functionalization results in an extended close-packed phase (Fig. 2a). This is attributed to the introduction of a symmetry axis in the molecule, allowing a higher packing density in a 2D arrangement (see tentative model Fig. 2c left). Next to hydrogen bonds, attractive dipole forces could be of relevance here.

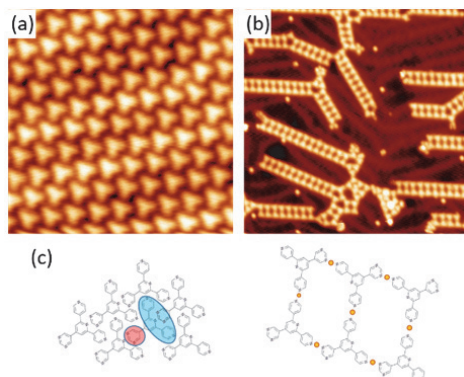


Fig. 2: Self-assembly of **2** on Au(111). (a). Extended closed-packed structure (10x10 nm²). (b) Metal coordinated ladder-like chains (40x40 nm²). (c) Tentative models for a and b, respectively.

Upon Cu adatom supply, straight ladder-like chains are formed (Fig. 2b), consisting of rectangular pores (see Fig. 2c right for the provisional model). XPS data again support the change in the binding motif

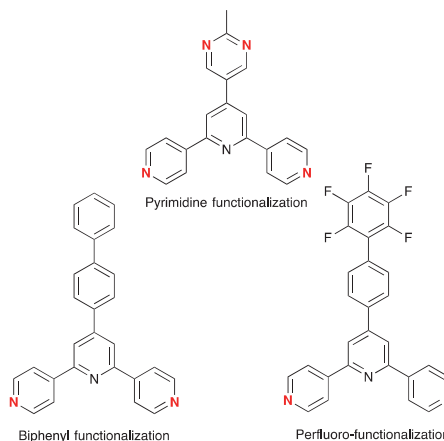
upon metal coordination by the chemical transition of the N1s state (see table 2).

XPS	-N= [eV]
H-bonded	398.8
Cu-coord.	399.6

Table 2: XPS data of **2** on Au(111) show also a clear increase of the binding energy upon metal coordination, in analogy to **1**.

Outlook

Regarding 2D on-surface assemblies, we are able to specifically switch the intermolecular binding motif from hydrogen-bonded to metal-coordinated. This is due to the special designed ligands. Scheme 2 shows different ligands which will be synthesized to investigate the influence of the molecular building blocks and the functional groups on the specific architecture of on-surface assemblies and coordination polymers. The extent to which proton switching at the imidazole leads to a variability of binding motifs is also an open question that shall be investigated with such compounds.



Scheme 2: Based on the 4,2':6',4''-terpyridine core, different functionalizations are able to be accomplished in near future.

Ultimately, we aim at understanding the designing rules for molecular building blocks towards the controlled assembly of supramolecular scaffolds at surfaces with well-defined and functional architecture as they are desired e.g. for catalysis.

References for Project P1203:

- [1] A. Shchyrba, et al. J. Am. Chem. Soc. **135**, 15270 (2013)
- [2] A. Shchyrba, et al. J. Am. Chem. Soc. **136**, 9355 (2014)
- [3] E.C. Constable, et al. CrystEngComm **14**, 3554 (2012)
- [4] Y. M. Klein, et al. Polyhedron **81**, 98 (2014)

Modifying reactivity, assembly and molecule-substrate magnetic exchange coupling of square-planar complexes

Project P1204 Site-specific magnetic studies and control of large self-assembled spin systems

Project Leader: T.A. Jung and A. Kleibert

Collaborators: J. Nowakowski (SNI-PhD Student), J. Girovsky, and M. Baljovic

Controlling on-surface metalation and molecular assembly

Interactions of square-planar complexes with substrates covered by an atomically thin superstructure have been extensively studied, especially their magnetic and spintronic properties in regard to applications [1,2]. Not as much attention, however, has been devoted to the influence of atomic overlayers on the reactivity and molecular assembly of square-planar complexes. In our previous work [3] we have shown that the presence of a $(\sqrt{2} \times \sqrt{2})R45^\circ$ reconstruction of a Cu(001) surface facilitates the on-surface metalation reaction of 5,10,15,20-tetraphenylporphyrin (2HTPP), i.e. the insertion of a metal atom into metal-free 2H-porphyrins, to occur below room temperature (RT). On bare Cu(001), in contrast, this effect will only occur above ~ 450 K. Our study concluded that the exothermal reaction between the two H atoms originally bound to the center of 2HTPP and one O atom from the reconstruction resulting in the creation of a water molecule promotes the metalation process. In absence of an oxygen-overlayer on Cu(001), H₂ is created upon metalation of 2HTPP in a reaction with a significantly less supportive enthalpy.

To better understand the phenomenon of adsorbate-facilitated on-surface metalation, we now studied the influence of N- and Cl-overlayers on metalation reactions occurring on Cu(001). Both these elements create a $c(2 \times 2)$ superstructure. Their influence on the reactivity of 2HTPP towards metalation is, however, entirely different. X-ray photoelectron spectroscopy (XPS) is used to monitor the progress of the metalation reaction by analyzing the chemical bonding state of the nitrogen atoms of the precursor and the product molecules, which can be conveniently assessed in the N1s lines. The initial molecule, i.e. 2HTPP comprises two N species which are visible in XPS as two separate peaks of different binding energies (BEs), namely the pyrrolic ($-\text{NH}-$, ~ 400 eV) and iminic ($=\text{N}-$, ~ 398 eV) nitrogen. The metalated reaction product, i.e. CuTPP, on the other hand comprises equivalent N atoms characterized by a single N1s peak at ~ 398.8 eV. Fig. 1 shows N1s and C1s XPS spectra of 2HTPP deposited on N/Cu(001) and Cl/Cu(001) substrates. After deposition of 2HTPP on both, substrates held at 100 K the two N1s peaks originating from the pyrrolic and the iminic nitrogen are present, indicating that no metalation has occurred (note that the N1s peak at 396.7 eV in Fig. 2a arises from the N superstructure).

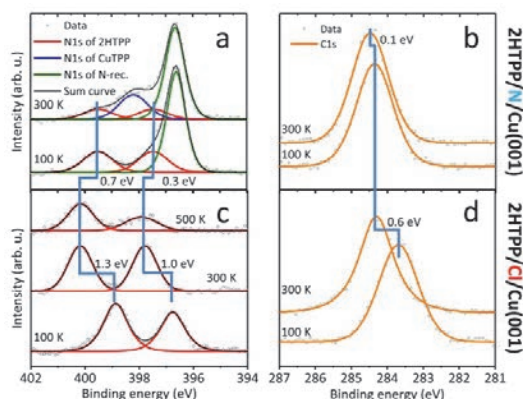


Fig. 1: Temperature-dependent N1s and C1s XPS spectra of 2HTPP molecules deposited on N/Cu(001) (a, b) and on Cl/Cu(001) (c, d). The former facilitates the metalation reaction to occur below RT, whereas the latter prevents metalation before desorption starts at ~ 500 K.

After warming up the 2HTPP/N/Cu(001) sample to 300 K, the signatures of the pyrrolic (~ 399.5 eV) and iminic (397.5 eV) nitrogen atoms decrease significantly in intensity, with a new peak appearing at ~ 398.1 eV, which we attribute to the newly created CuTPP. This indicates that the N superstructure on Cu(001) facilitates the metalation, with a yield of $\sim 50\%$, as concluded from the relative ratios of the different N1s signatures. With this result, an interesting question arises regarding the mechanism of the reaction. On the O-reconstructed surface, the exothermal creation of H₂O modified the energy balance of the metalation reaction. Since the release of an NH₂ radical is not as likely as of H₂O we propose, based on recent results obtained by temperature-programmed desorption of 2DTPP on Cu(111) [4], that the created NH₂ molecules diffuse to one of the phenyl rings of the porphyrin molecule, partially dehydrogenate it and desorb as ammonia (NH₃).

The presence of the Cl superstructure has a remarkably different influence on the reactivity of 2HTPP towards metalation. As shown in Fig. 1c & d, the BE of both N1s peaks and the C1s peak after cold-deposition of 2HTPP are significantly lower than the respective BEs on N/Cu(001) (c.f. Fig. 1a,b) and O/Cu(001) [1]. After warming the sample to 300 K, a large shift towards higher BE of all three signatures is observed. Interestingly, the Cl superstructure inhibits the metalation reaction, as after annealing the sample to ~ 500 K precursor molecules start to desorb from the substrate. The uncommon peak positions are caused by the much higher surface

dipole of the Cl superstructure layer in comparison with the N superstructure, which is caused by a significantly larger Cl-Cu bond length.

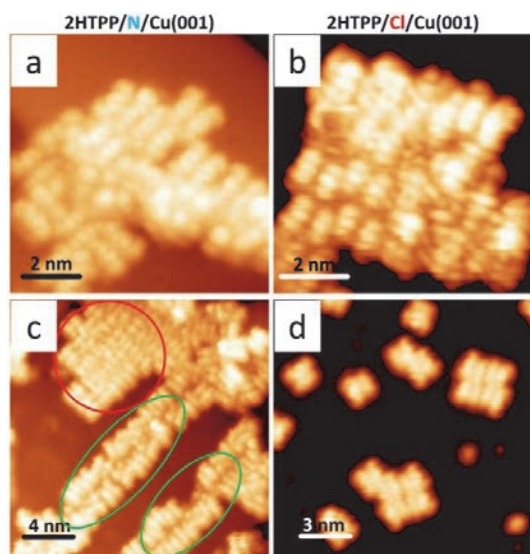


Fig. 2: STM data after deposition of 2HTPP molecules on a N/Cu(001) substrate (a, c) and a Cl/Cu(001) substrate (b, d) after cold deposition (a, b) and after warming up the substrate (c, d). 2HTPP molecules self-assemble on N/Cu(001) substrate at both temperatures; interestingly, on Cl/Cu(001) molecules create extended islands at low temperature, but adsorb strongly and create magic clusters at room temperature.

The studied N- and Cl- superstructures on Cu(001) have a contrasting influence also on the assembly of the studied 2HTPP molecules. As shown in the Scanning Tunneling Microscopy (STM) image (Fig. 2), 2HTPP self-assemble at both 100 K (Fig. 1a) and at RT (Fig. 1c). Interestingly, 2HTPP molecules on Cl/Cu(001) self-assemble only at 100 K (Fig. 1b), but create small clusters after reaching room temperature. Moreover, assemblies of 2 and 4 molecules are found to be the most favorable and thus can be described as magic clusters. STM also helps to understand why the metalation reaction yield on N/Cu(001) surface is low: Those molecules that adsorb on defects of the N superstructure appear differently than the other ones adsorbed on dislocation-free areas of the surface. We ascribe the former molecules to 2HTPP and the latter to the metalated CuTPP. This assignment supported by the observation of the feature in the center of the latter molecules.

Modifying molecule-substrate magnetic exchange coupling

We had shown earlier that we are able to modify the magnetic coupling strength of porphyrins to ferromagnetic Co substrates by using different substituents and thereby modifying the metal ion to substrate distance. We studied three molecules, namely MnOEPCI (smallest, ethyl substituent), MnTPPCI (phenyl substituent) and MnTTBPPCI (biggest, di-tertiarybutyl substituent). Here, we show

new results of the same molecules coupled to an oxygen-covered Co substrate: The present O superstructure adlayer modifies the influence of the three different substituents. On Co(001), as expected, molecules with larger substituents couple weaker to the substrate (Fig. 3, top panel). Interestingly, MnOEP and MnTPP molecules on the oxygen-terminated substrate couple to the substrate with nearly the same strength (Fig. 3, bottom panel). We tentatively attribute this observation to the molecules' modified ability to bend and flex on the less reactive substrate.

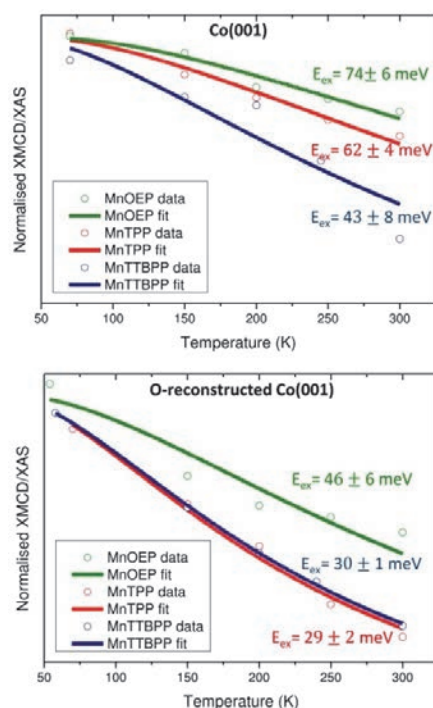


Fig. 3: Temperature-dependent XMCD data on Mn-porphyrins adsorbed on bare Co(001) and O-covered Co(001). The data has been fitted using a Brillouin function, from which the values of magnetic exchange coupling strength have been deducted.

To prove or disprove this assumption and to provide quantitative analysis on the effect of distance on magnetic coupling strength we collaborate with theoreticians performing density functional theory calculations on the studied systems. We are also currently performing X-ray photoelectron diffraction experiments that can allow us to measure the metal ion-substrate distance directly.

References for Project P1204:

- [1] D. Chylarecka et al., J. Phys. Chem. Lett., 2010, 1, 1408
- [2] C. F. Hermanns et al., Adv. Mater., 2013, 25, 3473
- [3] J. Nowakowski et al., Chem. Commun., 2013, 49, 2347
- [4] M. Röckert, J. Phys. Chem. C, 2014, 118, 267

Peering into the nuclear pore complex using a high-speed atomic force microscope

Project P1205 Watching the nanomachinery of the nuclear pore complex at work by high-speed AFM

Project Leader: R. Lim and C. Gerber

Collaborators: Y. Sakiyama (SNI-PhD Student)

Nanobiophysics of the nuclear pore complex

Nuclear pore complexes (NPCs) form the sole passageways between the nucleus and cytoplasm in eukaryotic cells [1]. The functional role of each ~100 nm-diameter NPC is to ensure that only specific molecules (i.e., cargo) gain access to the nucleus. To do so, the NPC *a priori* inhibits macromolecules above 40 kDa from traversing its channel. Exclusive access is given to specific cargoes that are accompanied by nuclear transport receptor proteins (i.e., karyopherins or Kaps) that interact with the NPC nanomachinery. These consist of ~200 intrinsically disordered proteins known as phenylalanine-glycine (FG)-repeat nucleoporins or FG Nups) that generate a permeability barrier within the NPC [2].

Over the last 5 years, my laboratory has worked intensely to resolve how NPCs mediate nucleocytoplasmic transport. In particular, we have (i) studied how multivalent NTR-FG Nup binding impacts on FG Nup barrier function and transport kinetics at the nanoscale using surface plasmon resonance [3-6], (ii) implemented selective transport control in two dimensions using a scaled-up biomimetic platform [7], and (iii) have verified the role of NTRs at the cellular level (*manuscript in preparation*). Taken together, our findings indicate that NTRs act in a concentration-dependent manner to regulate the NPC permeability barrier as bona fide constituents of the pore (Fig. 1).

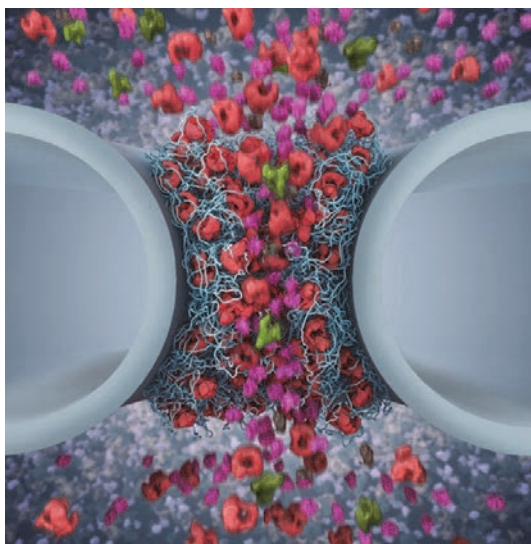


Fig. 1: Karyopherin-centric model of the nuclear pore complex (Artwork: Immanuel Wagner).

Revealing the molecular dynamics of functional NPCs by high-speed AFM

Still, the fact is that the permeability barrier has never actually been directly visualized with molecular detail inside functional NPCs.

To resolve this bottleneck, we have started using high-speed AFM (HS-AFM) as the only possible means to watch the nanomachinery of the NPC at work. Here, our goal is to visualize molecular-scale conformational changes in the NPC during transport *in situ* at the sub-nm and sub-100 ms spatiotemporal resolution. This offers a marked improvement over limitations of acquisition time in conventional AFM for NPC imaging. In this regard, single molecule fluorescence microscopy (SMFM) closely rivals HS-AFM given a spatiotemporal resolution of ~10 nm and ~1 ms. However, it is important to bear in mind that the proteins of interest (e.g. FG Nups, NTRs and cargo) themselves remain invisible in SMFM observations.

Getting started with high-speed AFM

Thanks to combined financial support from the SNI and the Biozentrum, I acquired an “Ando”-designed HS-AFM that was installed in March 2014. This is the same instrument that had resolved the true molecular dynamics of molecular motors and other biological nanomachines [8-10]. I had also acquired a scanning electron microscope (SEM) that is dedicated to constructing electron beam-deposited amorphous carbon tips (EBD tips). EBD tips are not only essential for producing tips of various aspect ratio and tip radii, but also allow for recycling HS-AFM cantilevers, which cost approximately 100 CHF per cantilever (Fig. 2).

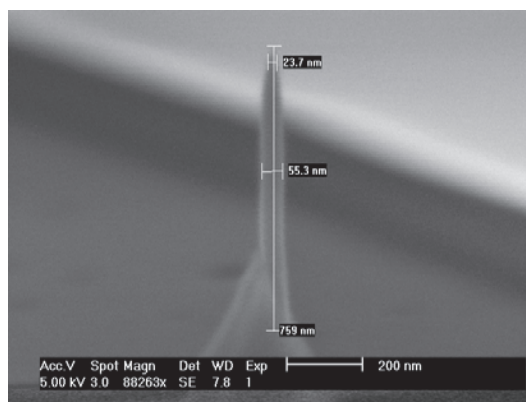


Fig. 2: EBD tip grown in a SEM. Length = 760 nm; Tip radius = 24 nm.

Peering into the pore by high-speed AFM

Around the same time, I had also successfully recruited Yusuke Sakiyama as a PhD student under the SNI Fellowship. Importantly, Yusuke had worked with HSAFM during his MSc work with Ando. Upon his arrival in April 2014, Yusuke quickly established, optimized and mastered the many interdisciplinary aspects of this project, including:

- (i) extracting live nuclei from *Xenopus* oocytes;
- (ii) attaching nuclei on HSAFM sample stages (2 mm-diameter glass rods);
- (iii) SEM modification for EBD tip preparation;
- (iv) preparing various reagents and recombinant proteins;
- (v) operating HSAFM to locate and visualize functional NPCs (Fig. 3).

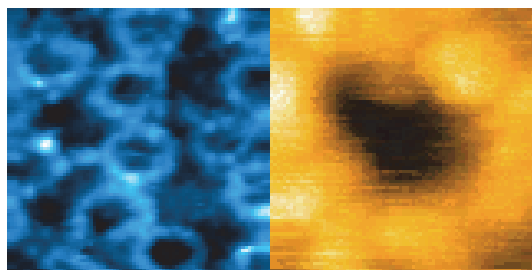


Fig. 3: (Left) Snapshot taken from a HSAFM movie of NPCs in action obtained at 440 ms per frame. The image is 400 nm x 400 nm. Each NPC is approx. 80 nm in diameter. (Right) Peering into a single NPC at 40 ms per frame. The image is 100 nm x 100 nm. Sakiyama and Lim, unpublished.

In this relatively short time, Yusuke has already started to reproducibly visualize NPCs at a spatial and temporal resolution that surpasses previous work [11]. Given his tremendous progress, I am confident that we should be able to achieve our goal of watching *in situ* FG Nup dynamics and NTR-cargo translocation within single NPCs in the coming months.

Needless to say, a highly anticipated manuscript is currently being prepared.

References for Project P1205:

- [1] M. Beck, F. Forster, M. Ecke, J.M. Plitzko, F. Melchior, G. Gerisch, W. Baumeister and O.

Medalia. Nuclear pore complex structure and dynamics revealed by cryoelectron tomography. *Science* **306**, 1387 (2004)

- [2] D. Grunwald, R.H. Singer and M. Rout, Nuclear export dynamics of RNA-protein complexes. *Nature* **475**, 333 (2011)
- [3] R.L. Schoch, L.E. Kapinos, and R.Y.H. Lim, “Nuclear transport receptor binding avidity triggers a self-healing collapse transition in FG-nucleoporin molecular brushes”, *Proc. Natl. Acad. Sci. USA* **109**, 16911 (2012)
- [4] R.L. Schoch and R.Y.H. Lim, “Non-interacting molecules as innate structural probes in surface plasmon resonance”, *Langmuir* **29**, 4068 (2013)
- [5] L.E. Kapinos, R.L. Schoch, R.S. Wagner, K.D. Schleicher and R.Y.H. Lim. “Karyopherin-centric control of nuclear pores based on molecular occupancy and kinetic analysis of multivalent binding with FG-Nucleoporins”. *Biophys. J.* **106**, 1751 (2014)
- [6] R.S. Wagner, L.E. Kapinos, N.J. Marshall, M. Stewart and R.Y.H. Lim, “Promiscuous binding of Karyopherin β 1 modulates FG Nucleoporin barrier function and expedites NTF2 transport kinetics”, *Biophys. J.*, *in press*
- [7] K.D. Schleicher, S.L. Dettmer, L.E. Kapinos, S. Pagliara, U.F. Keyser, S. Jeney and R.Y.H. Lim. “Selective transport control on molecular velcro made from intrinsically disordered proteins. *Nature Nanotechnol.* **9**, 525 (2014)
- [8] N. Kodera, D. Yamamoto, R. Ishikawa and T. Ando. “Video imaging of walking myosin V by high-speed atomic force microscopy”. *Nature* **468**, 72 (2010)
- [9] M. Shibata, H. Yamashita, T. Uchihashi, H. Kandori and T. Ando. “High-speed atomic force microscopy shows dynamic molecular processes in photoactivated bacteriorhodopsin”. *Nature Nanotechnol.* **5**, 208 (2010)
- [10] T. Uchihashi, R. Iino, T. Ando and H. Noji. “High-Speed Atomic Force Microscopy Reveals Rotary Catalysis of Rotorless F-1-ATPase”. *Science* **333**, 755 (2011)
- [11] D. Stoffler, K.N. Goldie, B. Feja and U. Aebi. “Calcium-mediated structural changes of native nuclear pore complexes monitored by time-lapse atomic force microscopy.” *J. Mol. Biol.* **287**, 741 (1999)

Hybrid spin-nanomechanics with diamond cantilevers

Project P1206 Nanomechanical oscillators for diamond spin-optomechanics

Project Leader: P. Maletinsky and R. Warburton

Collaborators: A. Barfuss (SNI-PhD Student), J. Teissier, E. Neu, and P. Appel

Introduction and motivation

The goal of this project is to establish and study a novel hybrid system consisting of a single electronic spin, which is coherently coupled to a nanomechanical oscillator. Such hybrid opto-mechanical systems are highly interesting candidates for studying the crossover from quantum to classical physics; additionally, they have the potential to yield novel types of high-performance sensing devices. Furthermore, such hybrid systems could be exploited for efficient, coherent manipulation of a quantum system by purely mechanical means – an approach which could be highly advantageous over established methods due to its compactness and potential efficiency.

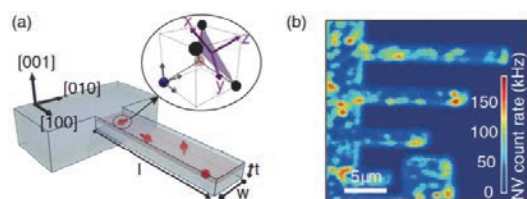


Fig. 1: (a) Schematic of the hybrid spin-mechanical system under investigation: We are studying the coupling of single electronic spins (red arrows) to nanomechanical oscillators. In our approach, the spin system is an “NV defect center” in diamond (see inset) and the nanomechanical oscillator is directly fabricated from high-purity, single-crystalline diamond material. Coupling between the spin and the oscillator is achieved through crystalline strain, which develops at the spins’ position when the cantilever bends. (b) Confocal optical image of our cantilever devices showing individual, implanted NV centers scattered across the sample surface [1].

In this project, we explore a purely diamond-based system, where the mechanical oscillator consists of a vibrating diamond beam with nanoscale dimensions and the spin system is formed by a particular lattice-defect, the Nitrogen-Vacancy center (NV center) in diamond. Coupling between the two entities is achieved by exploiting crystalline strain, which is induced by the cantilever’s vibration. This coupling mechanism is in itself novel and is efficient enough to potentially bring our system into the „strong coupling“ regime, where the coupling strength between spin and oscillator exceeds the dephasing rates of each individual component of this hybrid system. Furthermore, strain-coupling is intrinsic to our system and thus robust and virtually drift-free – an aspect which brings tremendous practical advantages for the highly sensitive, spectroscopic experiments we envisage.

The individual sub-systems in our devices (the spin and the oscillator) are highly attractive for the experiments we envisage: NV centers spins can be conveniently read out and initialized using optical means and they are known for exceedingly high coherence times up to one second, even at room temperatures. Diamond nanomechanical resonators, on the other hand, have been shown to exhibit very high quality-factors up to $Q \sim 10^6$ [2], and therefore form a well-isolated mechanical system, which is ideal to study the subtle effects a single spin could have on its oscillatory motion.

In the starting phase of this project we have successfully fabricated diamond nanomechanical resonators using dedicated nanofabrication technologies developed in our labs [3,4]. Using these structures, we explored the strain-induced spin-oscillator coupling and achieved a first quantitative measurement of the corresponding spin-strain coupling constants [1]. As a Hallmark for spin-oscillator coupling, we also observed for the first time motionally induced sidebands in the electron spin resonance signature of a solid state spin system.

Our results demonstrate first essential steps towards further studies of the quantum-dynamics of hybrid spin-oscillator systems. Examples include spin-based sideband cooling of a mechanical oscillator [5] or the recently proposed generation of spin-squeezing mediated by the diamond nanomechanical oscillator [6].

Key experimental results achieved

The single crystalline diamond nanomechanical oscillators we employed in our experiments were fabricated in house using electron-beam lithography and reactive ion etching techniques. In order to obtain highly coherent NV spins in these structures, we worked with ultraclean diamond starting material and controllably generated NV centers close to the sample surface by Nitrogen ion implantation and subsequent annealing. Fig. 1 summarizes the main aspects of our sample and in particular shows the presence of single NV centers (bright spots in the optical image shown in Fig. 1b) in our diamond cantilevers.

A central goal of our activities last year was to quantitatively determine the strength of the NV’s strain-coupling to our diamond cantilevers. To that end, we performed beam-bending experiments, where we examined the NV’s electron spin resonance (ESR) response as a function of applied strain. Fig. 2 shows the main result of these experiments and demonstrates successful spin-oscillator coupling through strain. In particular, the optically

detected ESR lines (dark contrast in the figure) split and shift as a function of strain transverse and longitudinal to the NV axis, respectively. A fit (yellow dashed lines) of the data to the eigenenergies of the strain-coupling Hamiltonian then allowed us to quantitatively determine the strain-coupling constants, which we determined to be on the order of few GHz/strain.

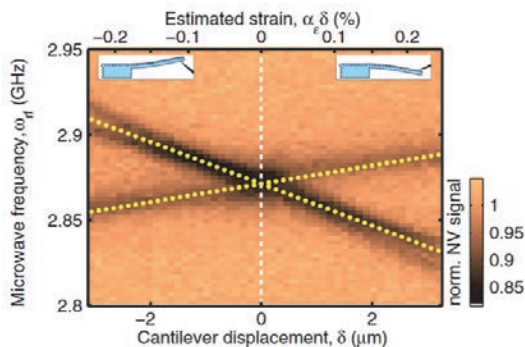


Fig. 2: Strain splitting of NV ESR lines as a function of static cantilever displacement δ . Positive and negative values of δ correspond to two different data sets (separated by the dashed line) and represent tensile and compressive strain at the NV location, respectively (see inset). Yellow dashed lines represent a fit to the strain-coupling Hamiltonian and allowed us to determine the previously unknown strain-coupling constants for the NV.

Our measurements of strain coupling constants are relevant for two reasons. First, these constants had never been measured before and constitute a fundamental property of NV centers, whose knowledge is important for a complete understanding of the NV's non-trivial electronic structure. Second, these strain-coupling constants allow us to estimate the expected spin-oscillator coupling strength, g_0 , per excitation quantum (phonon) in the cantilever – an essential figure of merit for the quantum-application envisaged in this project. While for our current devices, we found an estimated $g_0 \sim 0.1$ Hz, realistic improvements should allow us to achieve $g_0 \sim 1$ kHz in the future. This number compares favorably to dephasing rates of NV spins ($\gamma_{\text{spin}} \sim \text{few Hz}$) and of high-Q [2] nano-mechanical resonators at ultralow temperatures ($\gamma_{\text{osc}} < 1$ kHz). Based on our findings, we thus conclude that achieving the strong coupling regime with our novel, strain-coupled spin-oscillator device is a realistic goal for the future. Even if this goal should be too challenging on a short timescale, achieving a cooperativity $\kappa > 1$ (where $\kappa = g_0^2 / \gamma_{\text{osc}} \gamma_{\text{spin}}$) is a far less demanding goal and will already open the door to many of the quantum applications we envisage.

Outlook

Our findings form the basis for several follow-up experiments, which we will conduct in the next phase of this project. In particular, we will study how

strain-driving can be employed to coherently manipulate the NV spin, and we will explore the influence of our hybrid coupling on NV spin dephasing processes. Furthermore, we are interested in studying the effects of strain-coupling on orbital excited states of the NV by performing high-resolution spectroscopy. An important prerequisite for this are NVs with well-defined, sharp optical transitions close to the diamond surface – an important technical achievement that we have accomplished this year [7]. Based on such transitions and the strain-coupling we established, resonator sideband cooling [5] could be envisaged and might bring our system close to the motional quantum ground state. In the long run, we will extend our setup for operation in vacuum and ultimately under cryogenic conditions, to achieve maximal quality factors for our nanomechanical oscillators and obtain cryogenic pre-cooling of the mechanical oscillator.

References for Project P1206:

- [1] J. Teissier, A. Barfuss, P. Appel, E. Neu, and P. Maletinsky. “**Strain Coupling of a Nitrogen-Vacancy Center Spin to a Diamond Mechanical Oscillator**”, *Phys. Rev. Lett.* **113**, 020503 (2014)
- [2] Ovarchaiyapong, P., Pascal, L. M. A., Myers, B. A., Lauria, P. & Bleszynski Jayich, A. C. “**High quality factor single-crystal diamond mechanical resonators**”, *Appl. Phys. Lett.* **101**, 163505 (2012)
- [3] P. Maletinsky, S. Hong, M. S. Grinolds, B. Hausmann, M. D. Lukin, R. L. Walsworth, M. Loncar, A. Yacoby, “**A robust, scanning quantum system for nanoscale sensing and imaging**”, *Nature Nano.* **7**, 320 (2012)
- [4] E. Neu, P. Appel, M. Ganzhorn, J. Miguel-Sánchez, M. Lesik, V. Mille, V. Jacques, A. Tallaire, J. Achard, and P. Maletinsky. “**Photonic nano-structures on (111)-oriented diamond**”, *Appl. Phys. Lett.* **104**, 153108, (2014)
- [5] I. Wilson-Rae, P. Zoller, and A. Imamoglu, “**Laser Cooling of a Nanomechanical Resonator Mode to its Quantum Ground State**”, *PRL* **92**, 075507 (2004)
- [6] S. D. Bennett, N.Y. Yao, J. Otterbach, P. Zoller P. Rabl, and M. D. Lukin, “**Phonon-Induced Spin-Spin Interactions in Diamond Nanostructures: Application to Spin Squeezing**”, *PRL* **101**, 156402 (2012)
- [7] Y. Chu, N. P. de Leon, B. J. Shields, B. Hausmann, R. Evans, E. Togan, M. J. Burek, M. Markham, A. Stacey, A. S. Zibrov, A. Yacoby, D. J. Twitchen, M. Loncar, H. Park, P. Maletinsky, and M. D. Lukin. “**Coherent Optical Transitions in Implanted Nitrogen Vacancy Centers**”, *Nano letters* **14**, 1982 (2014)

Powering-up: Using proteorhodopsin to drive a molecular hoover

Project P1207 Design of a polymer membrane-based molecular “hoover”

Project Leader: W. Meier and D.J. Müller

Collaborators: R. Goers (SNI-PhD Student), J. Thoma, D. Harder, and D. Fotiadis

Introduction

The emerging field of synthetic biology aims at the creation of novel devices with functionalities not found in nature. In the present project, we plan to engineer nanocells and -layers that are composed of chemically and mechanically robust block copolymer membranes and act as light-driven molecular hoovers. This requires the development of strategies for functional insertion of membrane proteins into polymer membranes.

Over the last decade, several artificial devices have been developed that can function as nano-reactors. The transport of molecular compounds into their reaction compartment was achieved by passive diffusion [1]. In order to achieve control over this transport process, we aim for the reconstitution of light-triggered proton pumps together with transport proteins which utilize the proton gradient. Fig. 1 illustrates the gradient formation schematically.

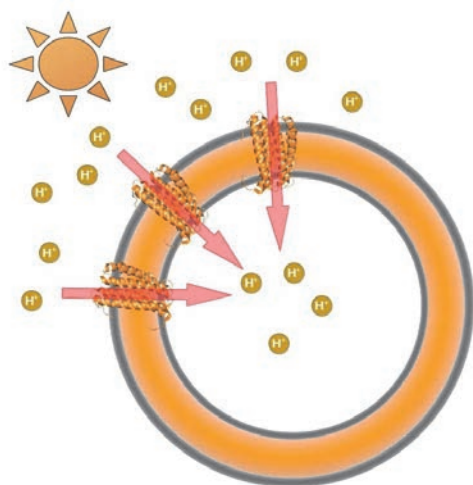


Fig. 1: Illustration of the proton transport process into a polymer vesicle by proteorhodopsin.

The scaffold can be formed by membrane-forming amphiphilic block copolymers, such as poly(2-methyloxazoline)-block-poly(dimethylsiloxane)-block-poly(2-methyloxazoline) (or, PMOXA-PDMS-PMOXA, ABA-type), which exhibit superior mechanical properties and are less permeable for small molecules than phospholipids [2]. Under these conditions, a gradient can be maintained for a longer period of time.

In this project, the membrane protein proteorhodopsin (PR) is used, a type I microbial rhodopsin, which translocates protons upon illumination similar to the well-known bacteriorhodopsin (BR). While they have

many structural and functional similarities, PR and BR have a different phylogenetic origin and utilize different wavelengths to activate their proton transport [3]. In the study presented here, PR was reconstituted into an artificial membrane composed of a PMOXA-PDMS-PMOXA triblock copolymer membrane. The proton pumping functionality was verified and the presence and orientation of the protein investigated.

Results & Discussion

In 2003, Rigaud et al. described a systematic approach for the reconstitution of membrane proteins into liposomes, and they determined optimal detergent concentrations for functional insertion [4]. These techniques were adapted here to the reconstitution of PR into polymersomes.

Similar to liposome formation, polymers dissolved in ethanol were dried under vacuum and subsequently rehydrated with an aqueous buffer which contained the pH-dependent fluorescent dye pyranine. This molecular probe enables the measurement of the internal pH of the vesicles. In order to break-up multilamellar structures, the solution was extruded through 200 nm pores. Subsequently the membrane was destabilized through the addition of 0.5 % n-octyl- β -D-glucoside (OG), which corresponds to its critical micelle concentration, and PR was added at a polymer/protein ratio of 25 (w/w). After incubation, the detergent was removed by the addition of biobeads following a protocol from literature [4]. Finally, the polymersomes were purified using size exclusion chromatography.

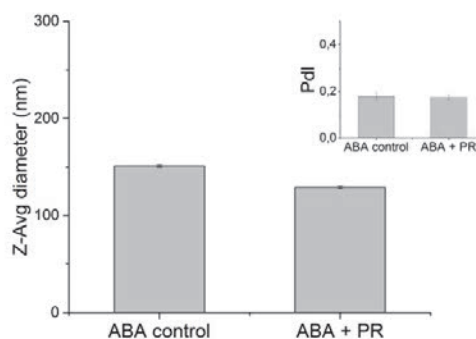


Fig. 2: Polymersome sizes without (left) and with PR (right). The inset shows the polydispersity index of the corresponding samples

The resulting vesicles were characterized by DLS. ABA control polymersomes without PR exhibit diameters of circa (151 ± 1) nm (Fig. 2), whereas proteopolymersomes have a slightly smaller diameter of (129 ± 2) nm (Fig. 2). However, in both cases the polydispersity index is low, 0.18 in case of the controls and 0.17 for the proteopolymersomes (Fig. 2, insert).

Importantly, these results show that the reconstitution only has a very small effect on the size of the vesicular structures and the treatment with OG does not induce structural changes.

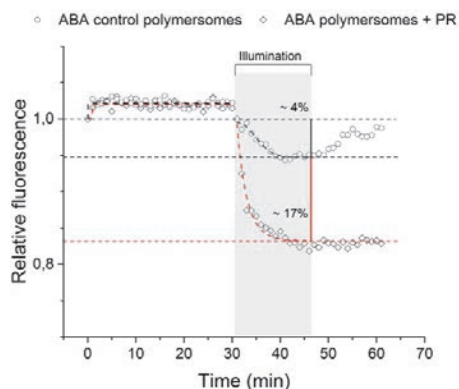


Fig. 3: Light-induced pH change in ABA polymersomes and PR-proteopolymersomes.

Besides an intact vesicular structure, the most important feature of the system is its capability to transport protons. The fluorescence of the pH responsive dye pyranine contained in the inner cavity of the polymersome was measured over time. To induce proton pumping, the sample was illuminated at a wavelength of 525 nm. Without illumination (Fig. 3) in the first 30 minutes, the control without PR and the proteopolymersomes do not show any change in their fluorescence signal. Subsequently, the samples were illuminated and the control shows a slight decrease in fluorescence by approximately 4%. After 15 minutes, the light is turned off and the decrease recovers. In contrast, the ABA PR proteopolymersomes show a stronger decrease of 17%, which corresponds to a decrease of the internal pH by 0.4 units. Here, the signal does not recover, indicating the dense packaging of the polymer membrane. These results lead to the assumption that PR is oriented with its C-terminus facing outwards and transports protons into the inside of the vesicles. It is known from literature that the termini of PR exhibit an asymmetric charge distribution around pH 6 [5]. Thus, zeta potential measurements could be used to study the orientation of the protein.

Indeed, the surface charge increases after reconstitution of PR as can be seen in Fig. 4. The control polymersomes show nearly no charge on their membrane surface whereas in case of the

proteopolymersomes the zeta potential increases to 21 ± 2 mV, which indicates the presence of PR and supports the assumption that PR is mainly oriented with its C-terminus facing outwards.

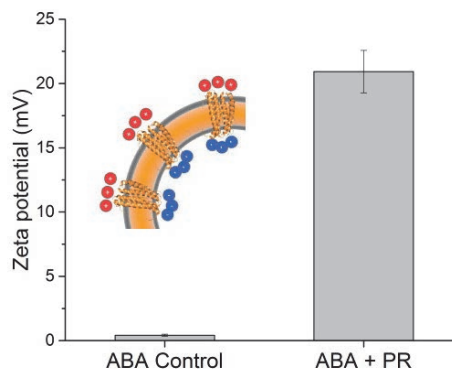


Fig. 4: Zeta potential measurements show the increase of the surface charge after PR reconstitution. The insert illustrates the charge of PR in the membrane.

Conclusion

In this work, we present a functional reconstitution of PR into ABA triblock copolymersomes. A reconstitution strategy from liposomes was adapted and a decrease of the internal pH could be observed. To our knowledge, it is the first time that the gradient formation over a polymer membrane has been shown for PR. Exploiting the asymmetric charge distribution of PR has been shown to be a valuable tool to determine its orientation. These results provide the necessary platform for more complex systems like a molecular Hoover. In further experiments we plan to investigate the folding of PR and its photocycle in the polymer membrane. Taken together, these results should lead to a publication in early 2015.

References for Project P1207:

- [1] Malinova, V., Meier, W. & Sinner, E. Synthetic biology, inspired by synthetic chemistry. *FEBS Lett.* (2012)
- [2] Broz, P. *et al.* Toward Intelligent Nanosize Bioreactors: A pH-Switchable, Channel-Equipped, Functional Polymer Nanocontainer. *Nano Lett.* **6**, 2349–2353 (2006)
- [3] Bèjà, O. *et al.* Bacterial Rhodopsin: Evidence for a New Type of Phototrophy in the Sea. *Science* **289**, 1902–1906 (2000)
- [4] Rigaud, J.-L. & Lévy, D. Reconstitution of Membrane Proteins into Liposomes. *Liposomes, Part B* **372**, 65–86 (2003)
- [5] Tunuguntla, R. *et al.* Lipid Bilayer Composition Can Influence the Orientation of Proteorhodopsin in Artificial Membranes. *Biophys. J.* **105**, 1388–1396 (2013)

Scanning probe microscopy on graphene

Project P1208 Ultra-sensitive force detection and molecular manipulation

Project Leader: E. Meyer and M. Poggio

Collaborators: M. Schulzendorf (SNI-PhD Student), S. Kawai, Th. Glatzel, A. Hinaut, R. Pawlak, U. Gysin, Y. Pellmont, and S. Decurtins

Current status of the LT beam deflection AFM

The low-temperature (LT) beam deflection Atomic Force Microscope (AFM) is in the final phase of construction. Most of the components for the ultra-high vacuum (UHV) system have now been purchased and were set up in the lab. Fig. 1 gives a first impression of the new system. The microscope head is now assembled and will be tested soon.



Fig. 1: Current status of the new LT-AFM, shown from left to right: analysis chamber with the housing for the microscope head and the cryostats on top and preparation chamber. Not visible here is the manipulator which was recently mounted to the right site of the preparation chamber. Inset showing the outer cryostat for liquid nitrogen (right) and inner cryostat for liquid helium (left).

The main transfer manipulator – which will also allow heating and cooling samples – was recently mounted into the system's preparation chamber. A mechanical support is now being built in-house.

The next important steps will be the mounting of the microscope head, including a suspension and damping system, the cryostats and the wiring of the electronics.

Measurements at the Swiss Light Source (SLS)

Last year, we reported a change of graphene's work function on Cu(111) induced by the deposition of alkali halides. It is known that graphene on metal surfaces can be intercalated by atoms [1] and molecules [2]. Despite the change of graphene's electronic properties, the actual origin remained unknown. This effect was either attributed to chemical interactions at the graphene/salt boundary or by intercalation and hence decoupling of the graphene from the metal. By AFM at room temperature, we found the graphene islands to be surrounded by alkali halide thin films. Lacking sub-surface resolution, intercalation – the continuation of the surrounding thin film underneath the graphene flakes – could not be proven.

Our findings encouraged us to further study the properties of this system at the SLS, located at the PSI. Within the SLS is the Photoemission and Atomic Resolution Laboratory (PEARL). There the sub-surface properties can be explored by angle-resolved and photon-energy-scanned X-ray photoelectron diffraction (XPD) experiments using synchrotron radiation. With this powerful techniques the molecular orientation, as well as binding lengths and angles within molecules can be determined [3]. Thus, XPD experiments should enable us to get an insight into the arrangement of the alkali halide thin films in respect to the graphene flakes. In addition the local surface properties can be probed at PEARL by scanning tunneling microscopy (STM). The usage of another scanning probe technique like STM allows for a comparison between the samples prepared at PEARL and those prepared in our lab, which were evaluated by means of (AFM).

Four major goals have been approached during the measurement time in autumn 2014 at PEARL. A new sample plate, suitable for the angular resolved photoelectron experiments and the STM measurements, had to be designed and constructed. The Cu(111) sample had to be cleaned, and well-defined graphene islands were deposited by a new local ethylene deposition system (nozzle setup) at PEARL. Finally the evaporation of the alkali halides, the STM and photoelectron spectroscopy measurements have been tested for the next measurement time.

New sample for PEARL

To meet the high requirements for angle-resolved photoelectron experiments a new copper single crystal with a special sample holder had to be bought and assembled, Fig. 2. The crystal surface had to be flat in respect to the sample holder plate and accurate in height as well.

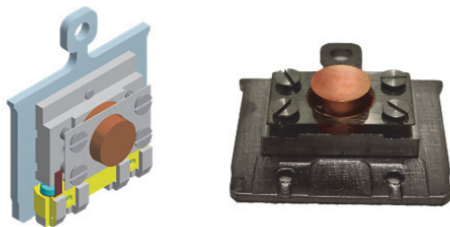


Fig. 2: Cu(111) sample for experiments at PEARL. Left side showing a CAD drawing by the PSI (back to front: Ta/Mo sample plate, Mo spacer, hat shaped copper single crystal, Mo sheet to fix the crystal, ceramic part (yellow) with direct heating contacts). The right image shows an assembled sample. The single crystals dimensions and orientation were measured by an optical laser microscope and the spacer was cut precisely by the mechanical workshop to obtain the desired height and orientation.

Graphene preparation at PEARL

Chemical vapour deposition (CVD) was used to prepare graphene by dosing the ethylene precursor gas through a nozzle directly on the hot, catalytically active Cu(111) surface [4]. For PEARL we constructed and implemented a new nozzle setup, as shown in Fig. 3.



Fig. 3: Setup for the graphene preparation at PEARL. A long nozzle (600 mm) with a z-drive (300 mm) – bellow visible in the image centre – is mounted to the preparation chamber. Valves at the rear of the nozzle allow for control of the gas flow. The upper right inset shows the approached nozzle. The inset in the lower middle is showing the guide that stabilizes the nozzle. Ion pump and z-drive were provided by R. Stania and T. Greber, University of Zürich.

Preparation simulations – running a preparation cycle without dosing gas – showed that small graphene flakes could just grow from ethylene contaminations at temperatures of $T=950\text{ °C}$ and a base

pressure of the preparation chamber in the $p = 10^9$ mbar range. Due to the optimization of the growth parameters the contamination of the preparation chamber could be drastically reduced. The dosing of the ethylene was limited to a short time of 2 min only after the growth temperature of 950 °C was reached. In addition, the overall gas pressures could be reduced by several orders of magnitude compared to the system in Basel (from 10^{-6} mbar range down to 10^{-9} mbar).

Furthermore, an angular orientation of the nozzle – allowing a homogeneous and continuous flow of the precursor gas at the Cu surface – showed to be crucial to obtain a well-controlled sub-monolayer growth. Finally we obtained small graphene islands on Cu(111) and could image the sample by STM (Fig. 4) and photo electron spectroscopy.

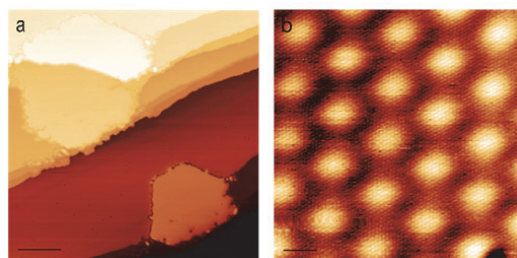


Fig. 4: STM images of graphene nano-islands on Cu(111). a) Islands grown at kink sites which induced bunching of copper steps (growth parameter – $p=5.9 \times 10^{-9}$ mbar, $T=950\text{ °C}$, $t=75$ s). b) Typical Moiré pattern of graphene flakes and atomic resolution; Imaging conditions: a) $U=1$ V (tip), $I=70$ pA, the scale bar is 20 nm; b) $U=160$ mV (tip), $I=200$ pA, the scale bar is 2 nm.

The quality of shape and the size of the graphene flakes still have to be improved. Unfortunately, first trials for the evaporation of alkali halides failed due to problems with the evaporator. The next measurement time at PEARL is planned for March 2015.

References for Project P1208:

- [1] U. Starke, S. Forti, K. V. Emtsev and C. Coletti, "Engineering the electronic structure of epitaxial graphene by transfer doping and atomic intercalation" *MRS Bull.* **37**, 1177–1186 (2012)
- [2] T. Bointon, I. Khrapach and R. Yakimova, "Approaching magnetic ordering in graphene materials by FeCl₃ intercalation", *Nano Lett.* **14**, 1751–1755 (2014)
- [3] S. Hüfner, "Photoelectron Spectroscopy: Principles and Applications", (Springer, 2003).
- [4] L. Gao, J. R. Guest and N. P. Guisinger, "Epitaxial graphene on Cu(111)", *Nano Lett.* **10**, 3512–6 (2010)

Design of polymer nanoreactors with triggered activity

Project P1209: Design of polymer nanoreactors with triggered activity

Project Leader: C.G. Palivan, J. Huwyler

Collaborators: T. Einfalt

Introduction

There is on focus today the need to introduce new systems that serve as functional spaces for desired reactions, with possible applications in domains such as medicine, catalysis or environmental sciences. In this respect, the design of nanoreactors, which are compartments with sizes in the nanometer range in which encapsulated/inserted active molecules act *in situ*, represents an elegant nanoscience-based strategy [1].

Here, we introduce nanoreactors with pH-triggered activity based on polymer vesicles with encapsulated enzymes and a membrane equipped with modified channel proteins, acting as “gates” (Fig. 1). The concept of nanoreactors based on polymer compartments with a permeable membrane (resulting from their intrinsic membrane property, or insertion of porines) is extended here by insertion of a chemically modified porin, which serves as a pH-responsive gate [2,3]. Only when the gate is open (by releasing its pH-sensitive cap), the substrate can penetrate the vesicle’s membrane and arrive inside the cavity where the enzymatic reaction takes place: the products are then released in the nanoreactor’s environment.

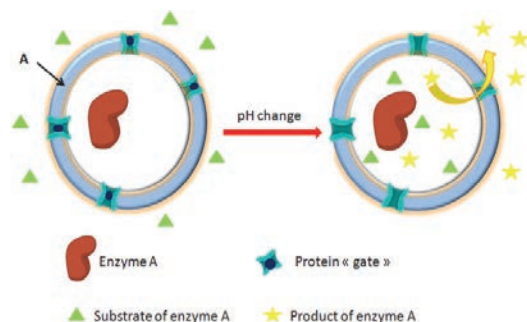


Fig. 1: pH-responsive nanoreactors which act only when the chemical linker blocking the porin (OmpF) is released.

Polymer vesicles (polymersomes) were prepared by self-assembly of a triblock copolymer poly(2-methyl-oxazoline)-*block*-poly(dimethylsiloxane)-*block*-poly(2-methyl-oxazoline) in dilute aqueous solution [4]. Polymersomes were prepared, both empty and in the presence of the enzyme horseradish peroxidase (HRP), and chemically modified channel porin, OmpF-CA. OmpF-CA serves to permeabilise the membrane when a change of pH in the environment of polymer vesicles takes place, while HRP serves as an active compound to generate *in situ* a desired pH-sensitive reaction.

OmpF Modification. The outer membrane protein F (OmpF) was expressed in BL21 (DE3) Omp8 Escherichia coli cells. A 3 % Octyl-glucopiranoside solution was used for the final extraction step. The extracted fraction was analyzed by 12 % SDS-PAGE (CBB stained), and the protein concentration determined by BCA. OmpF was stored at 4 °C in 3 % OG at a concentration of 1.2 mg/ml for several weeks. The functional characteristics of the OmpF pore are determined by six residues located inside of the constriction zone of WT OmpF. We decided to chemically modify the K16ε-NH₂ residue located inside of the pore in order to control the flux of molecules through the pore of OmpF. In order to form a pH cleavable hydrazone bond with fluorescent linkers, levulinic acid was first coupled to the available ε-NH₂ of the K16 via sulfo-NHS/EDC coupling, which served to introduce reactive carbonyl groups. A DMSO solution of Cyanine5 hydrazide (Cy5-hydrazide) was then added to carbonyl-modified OmpF (OmpF-CA), and native OmpF (OmpF-NA) at pH 7.5, and reacted overnight at ambient temperature. Non-reacted dye was removed by washing OmpF-NA and OmpF-CA with 3 % OG. In the next purification step, the detergent concentration was lowered to 0.05 % by overnight dialysis against a 0.05 % OG solution. Concentration of both the modified and unmodified protein was then determined with a BCA kit. OmpF-CA-Cy5, OmpF-NA and OmpF-CA were used for insertion during the self-assembly process of nanoreactors generation.

Design of the nanoreactors. pH-responsive nanoreactors were generated by film rehydration method in the presence of native and modified channel protein (OmpF, OmpF-CA-Cy5 and OmpF-CA), and HRP at 23 °C and pH = 7.4. Control vesicles were also prepared in the absence of OmpF or HRP. All solutions were then extruded in order to obtain the desired size homogeneity of the self-assembled 3D supramolecular structures. Free enzyme was removed by dialysis against PBS pH 7.9 for 5 days using a dialysis tube, with a cut-off size of 300 kDa, and then against PBS pH 7.2.

Characterization of the nanoreactors. A combination of transmission electron microscopy (TEM) and Static and Dynamic Light scattering (SLS, DLS) measurements was applied to determine: (i) the architecture of the 3D assemblies, (ii) the influence of enzyme and porin encapsulation and insertion, and (iii) the stability of the nanoreactors. To ensure that the vesicular structure was stable even at acidic pH, the 3D assemblies were characterized after 7 days in an acidic pH. Both empty vesicles and nanoreactors preserved their architecture and did not aggregate at low pH. The average hydrodynamic radius of nanoreactors was 70 nm (Fig 2).

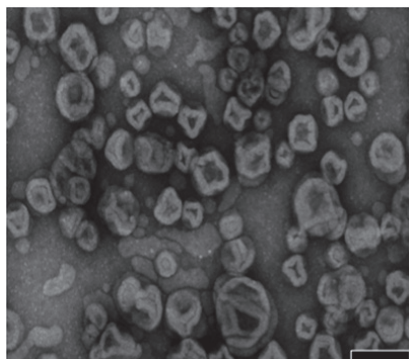


Fig. 2: TEM image of nanoreactors. Scale bar 200 nm.

pH-triggered activity of the nanoreactors. In order to determine whether the porin was appropriately modified with a pH-sensitive cap, we first investigated the specific binding of the dye to the carbonyl groups of the OmpF-CA. We used fluorescence correlation spectroscopy (FCS) because it measures the mobility of fluorescent molecules and allows establishing their size via Stokes-Einstein equation. We selected Cy5 as a model dye because of its pH insensitivity in the range of pH 3-10. A difference in molecular brightness was observed between OmpF-NA and OmpF-CA, where the fluorescent linker binds after mixing with the Cy5-hydrazine, and subsequent purification. A significant decrease in brightness is observed for OmpF-CA-Cy5 at acidic pH, which indicates the cleavage of the hydrazone bond, and subsequent release of the Cy5 molecule, which was blocking the OmpF pore (Fig 3). Our nanoreactor is pH-sensitive due to the insertion of a chemically modified porin, and not because of an intrinsic property of the polymer 3D assembly [5].

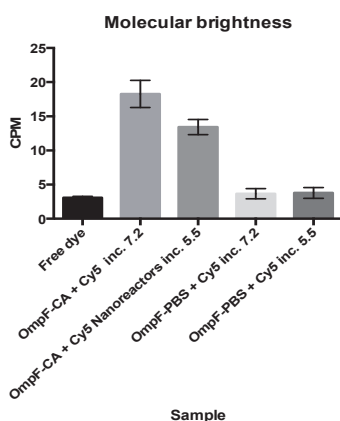


Fig. 3: Brightness of different unmodified and chemically modified OmpF molecules.

Enzyme kinetics inside nanoreactors. To assess how the nanoreactor activity was affected by the

chemical modification of the porin, we used the TMB (3,3',5,5'-tetramethylbenzidine) colorimetric system. TMB is a chromogen, which is used in enzyme immunoassays of HRP, and in molecular understanding of controlled compounds release through an engineered channel protein FhuA. The oxidation of TMB by HRP in the presence of H_2O_2 yields a blue colored product. Nanoreactors were incubated with TMB at pH 5.5 and TMB conversion rate was measured at pH 7.4 (Fig 4). After incubation of the nanoreactors with chemically modified OmpF (OmpF-CA), the enzymatic activity is restored, which indicates that the nanoreactors have a pH-sensitive functionality.

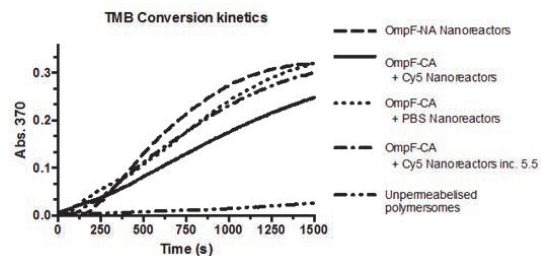


Fig. 4: TMB conversion kinetics in nanoreactors with OmpF-CA in various conditions. Once the linker is released at acidic pH, the substrate turnover is restored.

Conclusion. We designed a nanoreactor with a pH responsive enzymatic activity, based on a chemically modified channel porin OmpF, which was inserted in the membrane of polymer vesicles, and acted as a "pH responsive gate". Our system has high potential for biosensing and therapeutical applications.

References for Project P1209:

- [1] A. Najer, D. Wu, D. Vasquez, **C.G. Palivan**, W. Meier, *Polymer nanocompartments in broad-spectrum medical applications*, *Nanomedicine* **8**, 425, (2013)
- [2] **C.G. Palivan**, T. Einfalt, *Membrane proteins as functional gates in polymer membranes*, SNI Annual Meeting, Lenzerheide (2014)
- [3] T. Einfalt, R. Goers, A. Dinu, **C.G. Palivan**, *Design of polymer nanoreactors with triggered activity*, NICE Conference, Nizza (2014)
- [4] L.H. Dieu, L.H., D. Wu, **C.G. Palivan**, V. Balasubramanian, **J. Huwyler**, *Polymersomes conjugated to 83-14 monoclonal antibodies: In-vitro targeting of brain capillary endothelial cells*, *Eur. J. Pharm. Biopharm.* **88**, 316 (2014)
- [5] T. Einfalt, D. Vasquez, **C.G. Palivan**, *3D supramolecular assemblies of PEG-b-PMCL-b-PDMAEMA copolymers as pH responsive carriers for enzyme enhancement therapy* Nanomed, London (2014)

Nanowires as cantilevers: exploiting nonlinearities

Project P1210 Bottom-up nanowires as ultra-sensitive force transducers

Project Leader: M. Poggio and R.J. Warburton

Collaborators: D. Cadeddu (SNI-PhD Student) and A. Fontcuberta i Morral

Introduction

Due to their favorable geometry and potentially defect-free growth, nanowire (NW) cantilevers are promising as ultrasensitive force transducers for scanning probe microscopy. Additionally, their relatively high mechanical resonance frequencies decouple their motion to a large degree from external noise sources and should permit improved sensitivity in mass-sensing and scanning probe applications. Furthermore, the wide choice of nanowire growth material and the possibility to grow NW heterostructures could allow access to different measurement modalities, such as sensing of local electric or magnetic fields. In recent experiments, coupling of optical transitions of a self-assembled quantum dots (QDs) embedded in a NW to the motion of the NW through strain was demonstrated, opening the way to investigation of hybrid devices with nanowires as their main building blocks [1]. NW heterostructures are attractive as hybrid systems, as they can combine multiple functionalities in one integrated structure.

The goals of this project include: 1) the setup of a polarization-enhanced interferometer for the measurement of NW thermal motion in vacuum both at room temperature and temperatures below 1 K; 2) the characterization and optimization of NW properties for sensitive force sensing; and 3) the setup of a low-temperature scanning probe microscope customized for use with NW cantilevers.

Mechanical Mixing and Amplification

Conventionally, in scanning probe experiments, oscillatory motion of the cantilever is driven with amplitudes small enough to remain in the linear dynamical regime. Due to a number of reasons, including the oscillator geometry, nonlinear damping, the presence of external potentials, and nonlinear boundary conditions, this linear dynamic range is often quite limited in nanoscale oscillators. The nonlinear dynamics occurring when this range is exceeded, complicate the analysis of sensing experiments and are therefore generally avoided or compensated for. However, nonlinearities in general can also give rise to a host of useful effects, such as signal amplification, noise squeezing, and frequency mixing. The nonlinear dynamics of nanowire cantilevers can enable these effects at the nanoscale in mechanical form and have the potential to enhance the performance of cantilever-based sensors.

As part of goals 1) and 2), we study the motion of several GaAs NWs attached to their GaAs growth substrate [2]. Having built several polarization-enhanced fiber interferometers for the measurement of NW motion, i.e. goal 1), we observe that upon driving the periodic bending motion of a NW with sufficiently large amplitudes, it can no longer be de-

scribed by a linear equation of motion. Instead, the NW follows the, qualitatively different, nonlinear dynamics of a Duffing oscillator. A Duffing nonlinearity can give rise to complex motion of an oscillator, such as hysteresis, cascades of period-doubling, and chaotic motion. In the quantum regime, Duffing nonlinearities have recently been studied in the context of mechanical squeezing. Furthermore, we find that when applying two driving frequencies, the NW motion in the nonlinear regime contains components at frequencies other than the two driving frequencies, as a result of mechanical mixing.

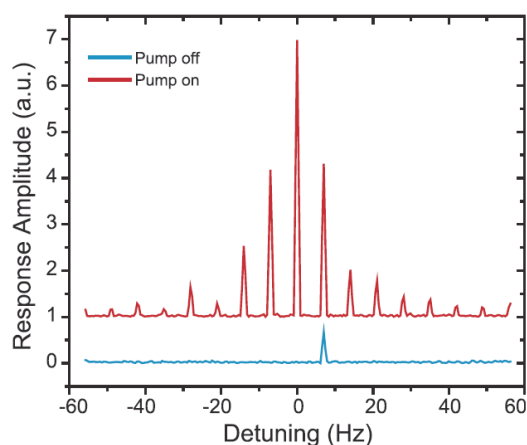


Fig. 1: Mechanical amplification [2]. Spectral response with pump excitation (1.29 MHz, 250 mV) off (on) in blue (red) for a signal detuned from the pump frequency by 7 Hz and with amplitude 35 mV. The curves have been offset for clarity.

In our investigation, we observe and characterize nonlinear motion of a variety of as-grown GaAs NWs. We observe mechanical nonlinearity already for modest driving amplitudes in all cases. Furthermore, we demonstrate that this nonlinearity allows for mechanical mixing of two excitations and amplification of a signal excitation through this mixing as shown in Fig. 1 [2]. This amplification could be utilized in several scanning probe techniques. For example, in the case where these NWs act as mechanical force transducers, the observed gain of 26 dB could make force sensitivities of $\sim 100 \text{ zN}/\sqrt{\text{Hz}}$ in a narrow bandwidth feasible. These results indicate that, although nonlinear motion can be non-negligible for NWs, the nonlinearity can also be turned into an advantage using simple measurement schemes. The nonlinearity could, in addition, lead to coupling of different flexural modes. Such nonlinear mode coupling could have several applications, including tuning the resonance frequency and quality factor of one mode through driving of the other mode, and implementing quantum non-demolition measurements of mechanical excitation.

Coupling of Mechanical Modes

Mode coupling in nanomechanical resonators is the subject of growing interest. Sufficiently strong coupling forms the basis for phenomena such as phonon-cavity physics, mechanically induced transparency, and synchronization. Such coupling may enable quantum non-demolition measurements of the excitation of one mode by measuring the frequency or phase of a coupled mode. Furthermore, mechanical mode coupling is interesting for various applications, including frequency and amplitude modulation, improvement of mechanical quality factors, several parametric amplification schemes, implementation of mechanical logic, and enhanced sensitivity in ultra-small mass, charge, and force detection. The coupling between multiple nanomechanical resonators has been studied in several top-down fabricated systems, including single and double beam structures and membranes. So far, mechanical mode coupling in bottom-up produced structures has not been studied extensively. Carbon nanotubes grown by chemical vapor deposition have been observed to exhibit strong coupling between flexural modes of different orders. In grown nanowires, transverse modes have been observed, but coupling has not yet been demonstrated or exploited.

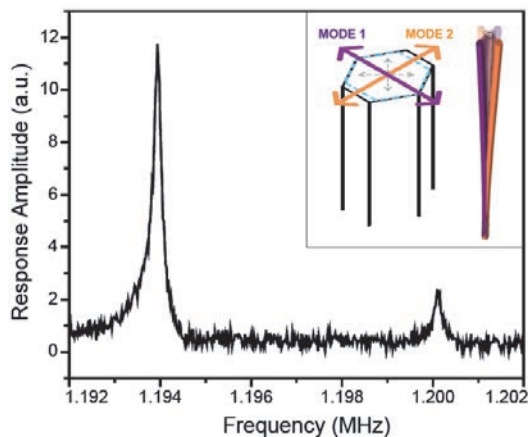


Fig. 2: Non-degenerate transverse flexural modes in a NW. Spectral response of the lowest order modes in an as-grown GaAs NW. Inset: schematic diagram showing the broken symmetry leading to the non-degenerate modes as well as the mode direction and shape.

As part of goals 1) and 2), we investigate the presence and coupling of non-degenerate, transverse flexural modes of as-grown GaAs NWs. An asymmetry in the cross-section of the NW leads to the formation of two transverse normal modes, with different eigenfrequencies. By driving one mode in its nonlinear regime of motion the other mode is observed to shift in frequency. In a ring-down-type experiment, this leads to a distinct beating pattern in the time domain, where the beating period decreases with time. We show that the mode coupling and nonlinearity can be exploited for the implementation of frequency modulation, amplitude to frequency

conversion and logical operations. In particular, we demonstrate the implementation of mechanical OR and NOR operations with the NW modes. The GaAs NW studied here is of particular interest, since such NWs form a template for further growth steps in fabricating AlGaAs/GaAs NW heterostructures, which can for example host self-assembled optical QDs [1].

Nanowires as Sensitive Scanning Sensors

The setup of a low-temperature scanning probe microscope (SPM) customized for use with NW cantilevers, i.e. goal 3), has recently been completed. First measurements are underway including the characterization of as-grown GaAs NW cantilevers at low temperature. The expectation is that their mechanical properties, as with those of conventional top-down cantilevers, should be considerably better at cryogenic temperatures. The use of the NW cantilevers as high-sensitivity atomic force microscopy (AFM) probes is also planned with this setup. Of particular interest, will be the use of the two orthogonal flexural modes for imaging surface force gradients along different directions simultaneously.

The new SPM is also equipped with a fiber-coupled confocal microscope for the excitation and collection of photoluminescence (PL) from QDs within the NWs. This capability will allow us to study not-only the coupling of the NW mechanical motion to the QD energy levels in more detail [1], but it should also enable the realization of a setup for “scanning QD” microscopy. With the simultaneous ability to measure PL from a QD-in-NW and to scan the NW over a surface, we should be able to map electric and magnetic fields of a sample surface using the QD as a sensor. This technique shares similarities with recently realized schemes using nitrogen-vacancy centers in diamond for the accurate mapping of magnetic fields [3]. Here, however, our scanning QDs should be particularly sensitive to electric fields and may provide a new and high-bandwidth method for mapping small electric fields [4].

Our collaboration with NW growers such as the Fontcuberta Group at EPFL and the Bakkers Group in Eindhoven has so far been highly productive and efficient. The respective students in each group are in frequent contact and work well together towards common goals. In the meantime, we are making contact with other growth groups to diversify the types of NWs available to us.

References for Project P1210:

- [1] M. Montinaro et al., *Nano Lett.* **14**, 4454 (2014)
- [2] F. R. Braakman et al., *Appl. Phys. Lett.* **105**, 173111 (2014)
- [3] C. L. Degen, *Appl. Phys. Lett.* **92**, 243111 (2008)
- [4] J. Martin et al., *Nature. Phys.* **4**, 144 (2008)

Electron optics in encapsulated graphene

Project P1211 Electrical properties of ultraclean suspended graphene

Project Leader: C. Schönenberger and D. Zumbühl

Collaborators: C. Handschin (SNI-PhD Student), P. Rickhaus, M. Weiss, and P. Makk

Motivation

The charge carriers in graphene are massless Dirac fermions with a linear dispersion relation pointing to an analogy between the charge carriers in graphene and photons. Quite recently, the mobility of suspended [1] and supported graphene [2] has reached numbers allowing for ballistic electron motion up to several micrometers. Since the wavelength of the electrons can be tuned by a gate voltage, many effects known from optics can be reproduced with electrons in graphene. Examples are interference effects realized in e.g. a Fabry-Perot interferometer [1] and quantization due potential confinement in constrictions. Moreover, phenomena known from optical ray physics may also be reproduced in graphene, since the refractive index is directly proportional to the carrier density which can be tuned in graphene seamlessly from electron to hole doping (n to p -doping). This allows the realization of mirrors, prism, optical guiding by total internal reflection and lensing. The different sign of carriers, electrons and holes, is directly mapped onto the sign of the refractive index. In graphene, one can therefore obtain a negative refractive index for electron waves. This allows to realize a *Veselago lens*. [3,4] In the Veselago lens, the divergent beam emanating from a point source in a positive index material is refocused into a point in a negative index material. The two materials face each other in flats, so that no curved surface is required for lensing in this case. An experimental demonstration of the Veselago lens, which is still open to be done, requires a relatively large doping gradient and point contacts that can be used as electron emitters and detectors.

Experimental challenges and progress

In order to actually be able to address the interesting Dirac physics, not only graphene of highest purity (e.g., single crystals exfoliated from graphite), but also a reduction of external influences is required. The latter includes chemical doping due to fabrication residues or charge puddles in the substrate coming from trapped charges in SiO_2 .

In the beginning of the project, we started to work with suspended graphene, since it had been shown to result in very high qualities [5-7]. It turned out, however, that it is difficult to achieve the same high mobility with multi-terminal devices. In suspended devices, the graphene is cleaned from resist residues originating from the fabrication by *current-annealing* – a technique where the graphene is heated in situ in the measurement setup to very high temperatures by passing a large current (~ 1 mA) through it. This is very difficult to do for multi-terminal devices such as the Veselago lens, since it is not a priori clear which terminals to use for the current annealing step. We have therefore decided

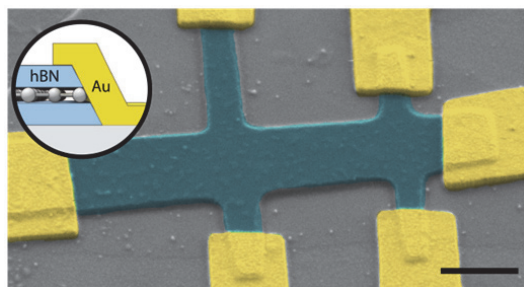


Fig. 1: SEM picture of a hetero-structure (Hall-bar) made of hBN-graphene-hBN (cyan) with side-contacts (yellow). The scale bar equals $1 \mu\text{m}$. The inset shows the schematic of the side contact (picture taken from Ref. [6]).

to shift the focus to graphene encapsulated in hexagonal boron nitride (hBN) using a so called *dry-transfer* technique and electrical *side-contacts* (Fig. 1) [2]. The dry-transfer technique makes use of the van der Waals force to pick-up and release layered systems onto each other. Consequently, during the fabrication the graphene never comes into contact with any solvent or resist and therefore remains clean. This technique yields qualities nearly as good as suspended graphene, but is much more versatile concerning the device geometry.

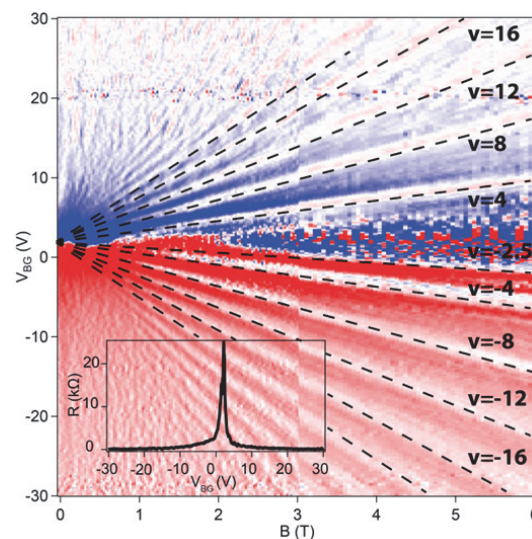


Fig. 2: Color map of the differential Hall voltage (here the numerical derivative d/dB for clarification) as a function of the back-gate voltage (V_{BG}) and the magnetic field (B) for a graphene bilayer device fabricated as depicted in Fig. 1. The quantized Hall-plateaus are indicated with dashed lines. Inset: Gate dependence of the resistance with a clear Dirac peak at zero magnetic field.

During the last months, the main focus was on establishing this encapsulation technique, which is completely new to our group. This includes the op-

timization of i) the cleanliness of dry-transferred graphene, and ii) side-contacts with low enough resistances $R \sim 1 \text{ k}\Omega/\mu\text{m}$. i) To obtain clean graphene, new processes such as Piranha cleaning of the SiO_2 chips were established. An example of a clean bilayer graphene (mobility up to $\mu = 110'000 \text{ cm}^2/(\text{Vs})$) and the corresponding Hall measurement is given in Fig. 2. ii) The contact resistance of the side-contacts is currently around $R \sim 3 \text{ k}\Omega/\mu\text{m}$, which is still slightly above the desired value. Nevertheless, it is in a range which allows the fabrication of functional devices.

Besides the sketched way of establishing side-contacts (first etching the hBN-graphene-hBN stack, afterwards metallization), efforts were also undertaken to investigate a *reversed-fabrication* approach. The latter includes the establishment of the side contacts in the first step and the etching of the hBN-graphene-hBN stack into its desired shape in the second step. This has the advantage that the graphene side-contacts are never in contact with any solvent or polymer before metallization which might lead to better contacts. So far, mostly 2-terminal devices and Hall-bars were fabricated as they allow an easy characterization of the contact-resistances and the graphene quality.

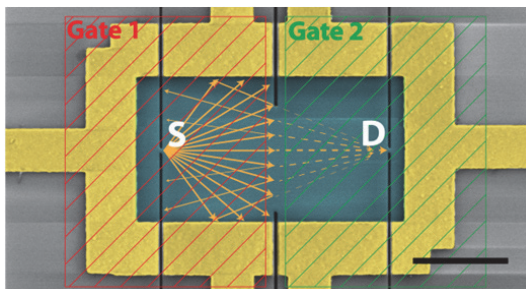


Fig. 3: SEM picture of two apertures denoted S and D cut into a test-structure (yellow=Cr/Au contacts, cyan="stack" (simply SiO_2 for the test sample)). The charge-carrier trajectories from source (S) to drain (D) are indicated with orange arrows (for the case of $V_{\text{gate}1} = -V_{\text{gate}2}$). Gates are indicated as an overlay in red and green. The scale bar equals $2 \mu\text{m}$

Apart from etching, which is the most common process for shaping the hBN-G-hBN stack in its desired configuration, a focused ion beam (FIB) was used to define the stack-boundaries. This might be of special interest for the Veselago lens in order to establish point-contacts using an aperture as shown in Fig. 3. The aperture on the left forms the source (S) from where the charge carriers are emitted ballistically into the device (orange arrows). At the pn-interface in the middle the charge carriers are partially reflected and partially transmitted with different probabilities depending on the incident angle. If transmitted, they would be focused back to the drain (D) (negative refraction). Note that this is a test structure and the pn graphene interface has not yet been realized. The technique to FIB the apertures directly into the heterostructure allows making point-contacts as small as $\sim 80 \text{ nm}$ in diameter in a

reliable manner. This would be much more difficult using a conventional etching mask.

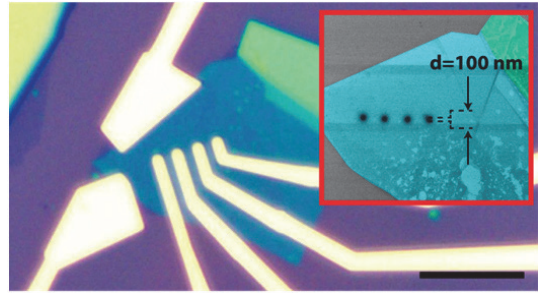


Fig. 4: Optical picture of point-contacts through hBN (bluish) on graphene with palladium contacts (yellow). The scale bar equals $10 \mu\text{m}$. Inset: SEM picture of the 100 nm wide holes in hBN before transferring onto graphene and supplementing them with Pd contacts.

Fig. 4 shows an alternative way of establishing point-contacts on graphene through a thin hBN layer in which holes were drilled into the top hBN layer using an FIB prior to transferring the hBN onto the graphene. This technique could be extended as well to hBN-graphene-hBN stacks, but for simplicity this first sample was produced on SiO_2 . We succeeded to realize first ohmic contacts with resistances near $R \sim 10 \text{ k}\Omega$ ($\sim 350 \Omega/\mu\text{m}^2$) at room temperature.

Outlook

Having solved most of the technical issues to establish a hBN-graphene-hBN heterostructure, the road is open to merge the single pieces to a real Veselago lens device. Besides the Veselago lens, the single and double-slit experiment known from optics is another possible experiment that could be realized this way. Furthermore, the top-contacts (using the FIB) allow designs which up to now have been out of reach in these hetero-structures, such as e.g. a Corbino disk where one has a contact in the center with ring electrodes around it.

Acknowledgements

We would like to thank Sofya Blanter (TU-Delft) and Balint Fülöp (BUT Budapest), two exchange students who did a training during several months at the SNI in Basel. They supported Clewin Handschin and contributed to establishing the stacking-technique. We also gratefully acknowledge the help of Marcel Düggelin and the whole ZMB team for their continuous support with the FIB

References for Project P1211:

- [1] P. Rickhaus et al., Nat Commun **4** 2342 (2013)
- [2] L. Wang et al., Science **342**, 614 (2013)
- [3] Veselago, Phys. Usp. **10** 50 (1968)
- [4] V. V Cheianov et al, Science **315**, 1252 (2007)
- [5] N. Tombros et al., J. Appl. Phys. **109** 093702 (2011)
- [6] P. Rickhaus et al., Nat Commun **4** 2342 (2013)
- [7] R. Maurand et. al., Carbon **79** 486 (2014)

A low-loss, broadband optical antenna for a single color center in diamond

Project P1212 Nano-photonics with diamond (comb.12)
 Project Leader: R.J. Warburton and P. Maletinsky
 Collaborators: D. Riedel (SNI-PhD Student), E. Neu, S. Starosielec

The nitrogen-vacancy (NV) center in diamond has a coherent spin and an optical transition which facilitates both spin initialization and read-out. These features are very attractive in a range of quantum applications, notably quantum sensing and quantum information processing. One major problem is that the extraction efficiency out of the high refractive index diamond is small: the critical angle at the diamond-vacuum interface is small such that even with an objective with very high numerical aperture, most of the light is not collected. Solving this problem by embedding the NV in a spherical nanocrystal is unattractive as the spin coherence is degraded. The challenge is to solve the problem while preserving the high spin coherence. In practice, this means creating nano-photonics devices from high quality single crystal synthetic diamond.

We report here success with an antenna [1]. An antenna changes the emission pattern of an emitter, ideally concentrating the light in one particular direction. A so-called dielectric antenna involves embedding a thin active layer between a material with lower refractive index and a material with higher refractive index, Fig. 1(a). This design is metal-free, thus eliminating losses via the creation of plasmons; it operates over a wide range of wavelengths; and in principle allows extraction efficiencies above 99%. We implement this concept by using a single crystal diamond membrane, just a few hundred nanometers thick, as active layer, bonded to gallium phosphide (GaP). GaP is a semiconductor with high refractive index, 3.3 (larger than that of diamond, 2.4) and is transparent at the NV emission wavelengths, Fig. 1(c). The vacuum-diamond-GaP heterostructure constitutes the antenna. In order to extract the light efficiently from the GaP, the GaP top surface is fabricated into a spherical shape such that the light can exit refraction, Fig. 1(a). The main challenge in creating the antenna is fabricating the diamond membrane. Single-crystal diamond has been sourced, commercially cut and polished into 50 μm thin samples. These samples are then etched using inductively coupled reactive ion etching, using a chlorine/argon etch to remove surface layers, and an oxygen etch to remove material relatively rapidly. In this way, membranes just a few μm thick are fabricated. It has been very challenging to produce membranes with smooth surfaces. The main problem has been the deposition of silica nanoparticles onto the diamond top surface, the silica arising from the effects of the etch gases on the silicon carrier substrate. Reproducibility has also been an issue. Nevertheless, process recipes have been developed which are yielding excellent results. GaP half-spheres have been sourced externally.

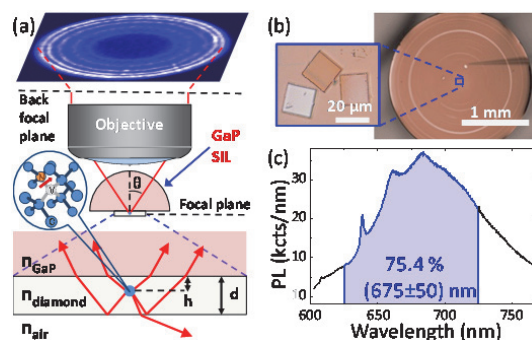


Fig. 1: (a) Schematic of the high-index dielectric antenna structure: a thin diamond membrane containing NV centres is bonded to a GaP lens. Most of the NV emission is located within the critical angle (47°) at the GaP: diamond interface. (b) Positioning of the diamond membranes onto the GaP lens using a micromanipulator. (c) Room-temperature emission spectrum of a single-NV center collected through the dielectric antenna.

Few-micron-thick membranes are bonded to the GaP via the van der Waals force, Fig. 1(b), and a final etch step allows the diamond to be thinned to a thickness of a few hundred nanometers. We note that the performance of the dielectric antenna is not critically dependent on either the exact membrane thickness or the position of the emitter within the membrane. The optical properties of NV centers are probed in the combined structure, Fig. 2. In particular, so-called back-focal-plane imaging allows the radiation pattern (emission intensity versus angle) of the device to be determined, Fig. 2.

The back-focal-plane image of an ensemble of color centers exhibits a clear ring-like structure, Fig. 2, clear evidence that the antenna is working. Furthermore, the intensity pattern can be described extremely well quantitatively by calculating the properties of an optical dipole in the antenna structure, Fig. 2. In the thinnest diamond membranes, single NVs can be isolated. We demonstrate a flux of single photons close to 10^6 per second. In fact, we can show that 90% of the light is emitted in the forward direction. Significantly, we also show that the spin coherence of the starting material is maintained in the antenna structure.

Further improvements to the dielectric antenna can be envisaged, perhaps leading to a further tenfold increase in the single photon flux. However, the small fraction of the emission into the zero phonon line is not altered in the broadband antenna. This fraction, just 4% for the NV center, can be boosted in a small mode volume, high-Q microcavity. Progress has been made in designing and characterizing highly miniaturized Fabry-Perot cavities [2].

Notably, the diamond membranes developed here are ideal for the cavity project: the membranes are bonded not to a GaP half-sphere but to a high-reflectivity mirror.

References for Project P1212:

- [1] D. Riedel, D. Rohner, M. Ganzhorn, T. Kaldewey, P. Appel, E. Neu, R. J. Warburton, and P. Maletinsky, “Low-Loss Broadband Antenna for Efficient Photon Collection from a Coherent Spin in Diamond”, *Phys. Rev. Appl.* 2, 064011 (2014)
- [2] L. Greuter, S. Starosielec, D. Najer, A. Ludwig, L. Duempelmann, D. Rohner, and R. J. Warburton, “A small mode volume tunable microcavity: Development and characterization”, *Appl. Phys. Lett.* 105, 121105 (2014).

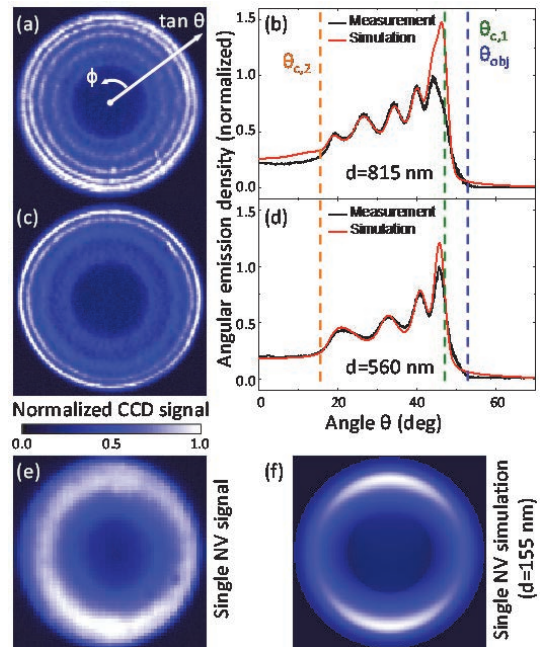


Fig. 2: Angular radiation patterns of NV ensembles in the dielectric antenna obtained by back focal plane (BFP) imaging for (a) $d = 815 \text{ nm}$ and (c) $d = 560 \text{ nm}$. (b),(d): Average intensity versus azimuthal angle. (e) Broadband emission pattern of a single NV center. (f) Calculated BFP image for an NV center in a diamond membrane with $d = 155 \text{ nm}$ and $h = 140 \text{ nm}$.

Hydrogen production based on molecular nanofactories

Project P1213 Artificial Metalloenzymes for Molecular Nanofactories

Project Leader: T. R. Ward

Collaborators: S. Keller (SNI-PhD Student), O. Wenger (Uni Basel), S. Panke (DBSSE), W. Shaw (PNNL, USA)

Introduction

Hydrogen is an attractive, clean and renewable energy vector. In this context, formic acid has been identified as a promising, safe and easy-to-handle hydrogen storage medium^[1]. The reversible catalytic decomposition of formic acid yields dihydrogen and carbon dioxide and is mediated by organometallic catalysts. In particular, d^6 pianostool complexes have demonstrated their versatility as formate dehydrogenase catalysts. However, these studies are typically performed with high formic acid concentrations. In a biological context, formic acid can be produced metabolically from glucose by a pyruvate lyase mechanism^[2]. With the long-term goal of producing biohydrogen *in vivo* by a chemoenzymatic cascade, we set out to compare and evaluate the performance of d^6 pianostool complexes at low formate concentrations. In collaboration with Prof. S. Panke (DBSSE) we plan to perform catalysis inside *E. coli* taking advantage of the biotin-streptavidin technology^[3,4].

Together with Prof. S. Panke, we have demonstrated that artificial metalloenzymes (ArM) can be compartmentalized into the periplasm of *E. coli*. Formic acid can be metabolically produced in the cytoplasm and exported to the periplasm where the ArM could decompose it to dihydrogen and carbon dioxide.

To mimic the formate decomposition produced by *E. coli* strains, the following reaction conditions were selected: buffered solutions (pH = 4.0), 37°C and a formate concentration of either 230 or 45 mM. Screening of complexes **1–12** for their formate dehydrogenase activity through the determination of gas evolution measured by an automated gas burette system led to the identification of $[\text{Cp}^*\text{Ir}(\text{phenpz}(\text{CO}_2\text{H}))\text{H}_2\text{O}]^+$ **8** and $[\text{Cp}^*\text{Ir}(\text{imim})\text{H}_2\text{O}]^{2+}$ **11** as the most active catalysts^[5]. Biotinylated versions $[\text{Biot-Cp}^*\text{Ir}(\text{phenpz}(\text{CO}_2\text{H}))\text{H}_2\text{O}]^+$ **13** and $[\text{Biot-Cp}^*\text{Ir}(\text{imim})\text{H}_2\text{O}]^{2+}$ **14** were synthesized to determine their formate dehydrogenase activity inside streptavidin as host protein (Fig. 2).

The pianostool complex $[\text{Biot-Cp}^*\text{Ir}(\text{phenpz}(\text{CO}_2\text{H}))\text{H}_2\text{O}]^+$ **13** was tested and displayed a turnover number of nine without protein and fifteen in the presence of streptavidin. The significant decrease in rate when compared to $[\text{Cp}^*\text{Ir}(\text{phenpz}(\text{CO}_2\text{H}))\text{H}_2\text{O}]^+$ **8** might be due to the intermolecular coordination of the thioether of biotin to the iridium center. Upon addition of streptavidin, the rate increases again since the thioether is tightly embedded inside the binding pocket of the protein.

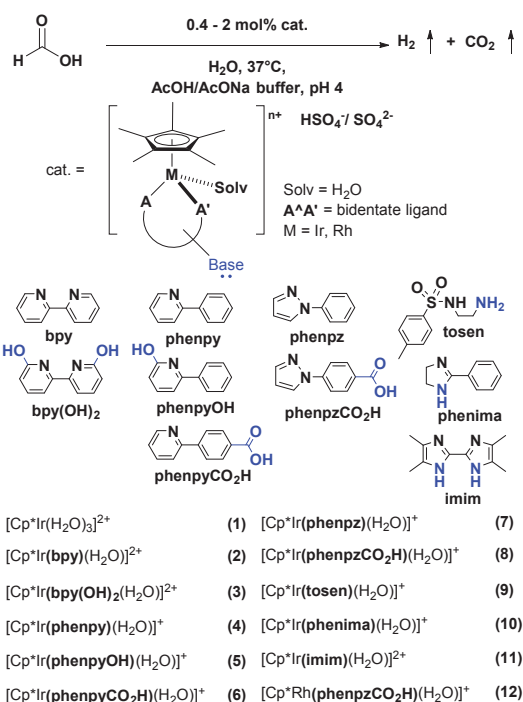


Fig. 1: Catalytic decomposition of formate to dihydrogen and carbon dioxide is catalyzed by d^6 -pianostool complexes. Ligands and corresponding complexes screened in this study.

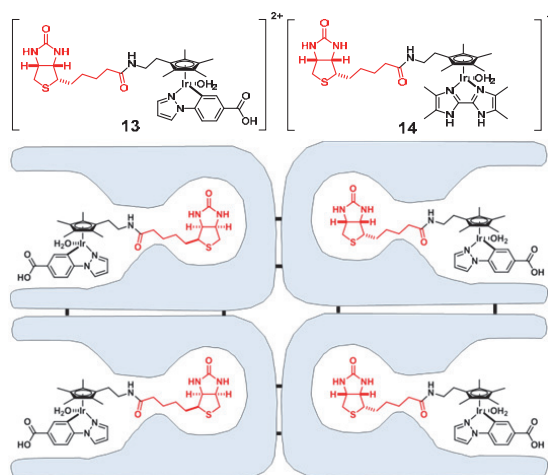


Fig. 2: Biotinylated formate hydrogenase complexes **13** and **14** and a cartoon representation of the streptavidin tetramer hosting four biotinylated catalysts **13**

Towards an efficient photo-driven hydrogenase based on the biotin-streptavidin technology

In collaboration with Prof. O. Wenger and Dr. W. Shaw (PNNL), we are scrutinizing an alternative approach to producing hydrogen.

The strategy is to bind a photosensitizer to streptavidin in the proximity of a biotinylated hydrogen reduction catalyst. Upon light excitation, the protein-bound photosensitizer is expected to donate electrons to the biotinylated proton reduction catalyst. For this purpose, we tethered the rhenium photosensitizer **15** to His87 of streptavidin ($[\text{Re}(\text{phen})(\text{CO})_3]\text{-His87 SAV}$ hereafter)^[6]. Successful anchoring was demonstrated by ESI-MS, UV-Vis and SDS-page analysis. Next, the biotinylated triarylamine **16** acting as electron donor was added to $[\text{Re}(\text{phen})(\text{CO})_3]\text{-His87 SAV}$. Unfortunately, no quenching of the excited state lifetime could be detected. This suggests that the distance between the donor and acceptor pair is too large to favor quenching (Fig. 3).

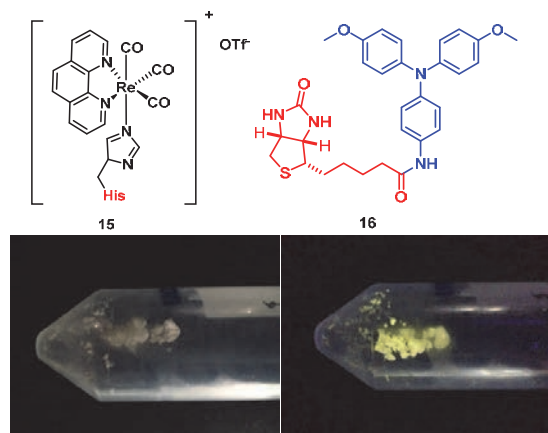


Fig. 3: Streptavidin as host for phototriggered charge separation. Rhenium photosensitizer **15** bound to histidine 87 of streptavidin. Biotinylated triarylamine **16** as electron donor. $[\text{Re}(\text{phen})(\text{CO})_3]\text{-His87 SAV}$ (bottom left); $[\text{Re}(\text{phen})(\text{CO})_3]\text{-His87 SAV}$ upon irradiation at 366 nm (bottom right).

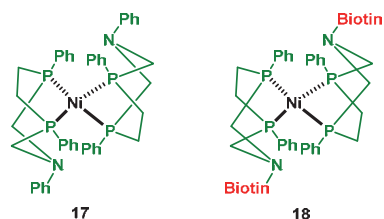


Fig. 4: Most efficient hydrogenase catalyst NiP4 **17** and its biotinylated analog biotNiP4 **18**.

Ultimately, the biotinylated triarylamine **16**, will be substituted by a proton reduction catalyst. With this goal in mind and in collaboration with Dr. W. Shaw (PNNL, USA, who has designed the most efficient hydrogenase NiP4 **17**), we are synthesizing a biotinylated biotNiP4 **18** analog (Fig. 4)^[7].

Outlook

Having identified highly active homogeneous formate dehydrogenases, and moderately active biotinylated formate hydrogenases the next step is to test other promising biotinylated catalysts for artificial hydrogenase catalysts based on Earth-abundant catalysts.

For this purpose, we have teamed up with Prof. Oliver Wenger (UniBas) and Dr. W. Shaw (PNNL, USA) to investigate the potential of NiP4-type catalysts within a protein environment. Although we will initially test electrochemical means for hydrogen production, we plan to rapidly switch to photodriven hydrogen production.

References for Project P1213:

- [1] G. Laurency, "Hydrogen storage and delivery: The carbon dioxide – formic acid couple", *Chimia* **65**, 663 (2011)
- [2] T. B. Causey, K.T. Shanmugam, L. P. Yomano and L.O. Ingram, "Engineering *Escherichia coli* for efficient conversion of glucose to pyruvate", *Proc. Natl. Acad. Sci., U. S. A.* **101**, 2235 (2004)
- [3] T. R. Ward, "Artificial metalloenzymes based on the biotin-avidin technology; enantioselective catalysis and beyond", *Acc. Chem. Res.* **44**, 47 (2011)
- [4] V. Koehler, Y. M. Wilson, M. Dürrenberger, D. Ghislieri, E. Churakova, T. Quinto, L. Knörr, D. Häussinger, F. Hollmann, N. J. Turner and T. R. Ward, "New synthetic cascades by combining biocatalysts with artificial metalloenzymes", *Nature Chem.* **5**, 93 (2013)
- [5] S. Keller, M. Ringenberg, D. Häussinger and T. R. Ward, "Evaluation of the formate dehydrogenase activity of three-legged pianostool complexes in dilute aqueous solution", *Eur. J. Inorg. Chem.* **34**, 5860 (2014)
- [6] B. R. Crane, A. J. Di Bilio, J. R. Winkler, H. B. Gray, "Electron tunneling in single crystals of *pseudomonas aeruginosa* azurins", *J. Am. Chem. Soc.* **123**, 11623 (2001)
- [7] M. L. Reback, G. W. Buchko, B. L. Kier, B. Ginovska-Pangovska, Y. Xiong, S. Lense, J. Hou, J. A. S. Roberts, C. M. Sorensen, S. Raugei, T. C. Squier, W. J. Shaw, "Enzyme design from the bottom up: An active nickel electrocatalyst with a structured peptide outer coordination sphere" **20**, 1510 (2014)

Ultracold atoms and ions on a chip

Project P1214 An ion-atom hybrid trap on a chip

Project Leader: S. Willitsch and P. Treutlein

Collaborators: I. Rouse (SNI-PhD Student), A. Mokhberi and R. Schmied

Introduction

The trapping of charged and uncharged particles through electromagnetic fields has proven essential for the high-precision study of a variety of quantum systems, from the spectroscopy of a single ion to investigating unusual states of matter such as Bose-Einstein condensates.

The miniaturization of existing atom and ion trapping technologies from macroscopic structures into chip-based forms has further enabled new applications in quantum metrology, quantum information processing and the trapping and cooling of charged molecules. Macroscopic hybrid traps for the simultaneous trapping of both neutral and charged species have previously been demonstrated [1], but as of yet the analogous chip system has not. Such a chip would allow for a more precise control over trapped species and act as a stepping-stone towards more complex and flexible trapping architectures.

Although microscopic traps for both ions and atoms are referred to as chip traps, they are constructed in quite different ways, and the hybrid chip trap must successfully combine both. The ion chip uses voltages applied to sheet-like electrodes to generate an electric field, which, due to Maxwell's equations, must contain a time-varying component to generate a three-dimensional trap. For these types of traps, this is achieved by applying a radio-frequency voltage to two of the electrodes, trapping the ions in a rapidly oscillating field. The atom chip uses a different mechanism, controlling the neutral atoms through the interaction of their quantum-level structure with a magnetic field. This magnetic field is produced through passing small currents through wires contained on the atom chip.

Design and simulation of a combined ion-atom chip

The design of the chip is constrained by the need to ensure that both the atomic and ionic species can be trapped in the same location, and in such a way that the trapping of one species does not interfere with the confinement of the other. A two-level structure was designed to facilitate this consisting of a series of gold-plated electrodes mounted on a printed circuit board with the wires required for atom trapping (Fig. 1).

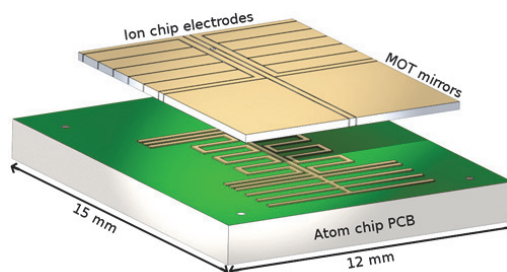


Fig. 1: Schematic of the hybrid chip trap with upper and lower layers separated to show the structures on the lower layer.

This chip then rests atop a copper heat sink, containing a broad U-shaped wire used to generate a magneto-optical trap (MOT) to collect the rubidium atoms from a vapor. This MOT requires laser light to be reflected off the surface of the trap, a process which leads to the formation of electric patch potentials that would disrupt the trapping of ions. To overcome this, the MOT is operated some distance away from the main experimental area, and the collected atoms are transported on a “magnetic conveyor belt” to the central area of the chip to interact with the ions.

To confirm that the chip design is suitable for use, it is then necessary to ensure that it will be able to efficiently transport and trap particles. Molecular dynamics simulations were implemented in the ProtoMOL software package in order to numerically solve Newton's equations of motion for particles in the time-dependent potentials generated by the chip. For the ions, the forces present are those due to the interaction of the charged particles with each other and with the electric field produced by the electrodes, the radiation force caused by the laser used to cool the ions, and a stochastic force to represent collisions with background gas. The laser cooling of the ions typically results in the formation an ordered structure known as a “Coulomb crystal” (Fig. 2), and comparison of the experimentally-obtained images of these crystals to those generated through these simulations will be used to determine the number and temperature of ions that are trapped.



Fig. 2: Simulated picture of a Coulomb crystal of 50 Ca^+ ions formed in the chip trap at a temperature of 30 mK.

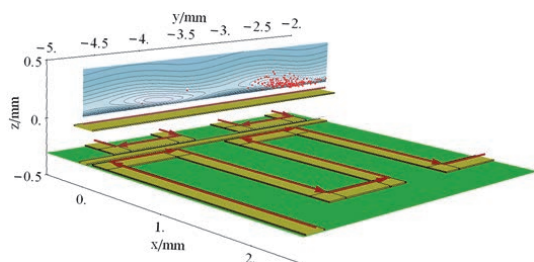


Fig. 3: Snapshot of the position of atoms (red points) during a simulation of the magnetic conveyor sequence, with a contour plot of the magnetic potential and arrows showing the direction of current in the wires.

Two types of simulation involving neutral atoms have been run in order to investigate different stages of the atom chip sequence. The first is to characterize the mirror-MOT used to initially gather atoms from background gas. The second investigates the transfer of atoms from an initial wide trap to a compressed one, and then into the “meander conveyor” to be transported to the final interaction region. These latter set of simulations are especially important to confirm that the atom cloud is not significantly heated during the transportation process, which would result in the loss of atoms and make the final production of a BEC more challenging.

Manufacturing process

Manufacturing the chip represents an additional challenge. The upper layer requires laser cutting narrow but deep cuts into stainless steel, a process which is not easily achievable, while the lower layer requires etching a PCB with features of sizes smaller than one hundred microns. Nonetheless, manufacturers for both components have been identified, and prototype atom chips have been supplied for use in initial testing (Fig. 4). This testing will be performed to confirm that the wire thickness and the heat capacity of the substrate are suitable for carrying the currents needed for sufficiently long times to allow experiments to be performed.

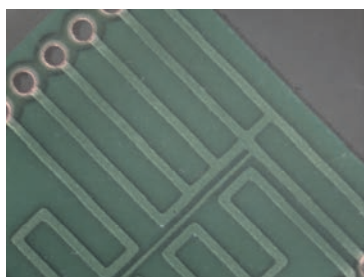


Fig. 4: View of the prototype atom chip PCB showing the wires used for initial trapping and compression of an atomic cloud.

With both components manufactured separately they must then be combined to form the hybrid chip. This will be achieved by including alignment features onto both chips and using these to ensure that the two chips are both positioned correctly relative to each other. This alignment step is crucial to

ensure that the magnetic conveyor belt can be operated successfully and that both species can be trapped in the same location with maximum efficiency.

Prototype ion chip

The technology for the present ion chip has recently been established and tested in a prototype in which both atomic and molecular ions were trapped and cooled [2,3]. Mono- and bi-component ion Coulomb crystals were obtained (Fig. 5) and their structural and energetic properties were characterized with the help of molecular-dynamics simulations. The flexibility in shaping the trapping potentials on the chip enabled the generation of three- and two dimensional crystal shapes and also allowed the separation of different ion species in the crystal. These results prove the functionality and versatility of the present ion chip design and represent an important prerequisite for the hybrid ion-atom chip.

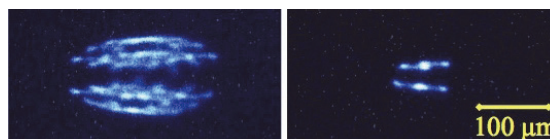


Fig. 5: False-color fluorescence images of sympathetically cooled nitrogen molecular ions embedded into a Coulomb crystal of laser-cooled calcium ions on an ion-trap chip [2]. The non-fluorescing molecular ions are visible as a dark region in the center of the crystal.

Outlook

Once the chip has been assembled into a vacuum chamber and the laser system set up, experiments can be performed. After the ability of the chip to trap both species has been confirmed, an interesting initial experiment would be to form a BEC of atoms and observe the behavior of this system in response to the presence of multiple trapped ions. This hybrid system is expected to show a number of interesting features, but so far has only been demonstrated for a single trapped ion doped into the BEC. Other possible uses for the hybrid chip would be to investigate collision dynamics at low temperatures to help better understand the processes involved in elementary chemical reactions, and to open up new avenues for the field of quantum information processing to explore.

References for Project P1214:

- [1] S. Willitsch, “Coulomb-crystallised molecular ions in traps: methods, applications, prospects”, *Int. Rev. Phys. Chem.* **31**, 175 (2012)
- [2] A. Mokhberi and S. Willitsch, “Sympathetic cooling of molecular ions in a surface-electrode ion trap”, *Phys. Rev. A* **90**, 023402 (2014)
- [3] A. Mokhberi and S. Willitsch, “Structural and energetic properties of molecular Coulomb crystals in a surface-electrode ion trap”, *New J. Phys.*, submitted

Nanoelectronics at ultra-low temperatures on a cryogen-free dilution refrigerator

Project P1215 Nanostructure Quantum Transport at Microkelvin Temperatures

Project Leader: D. Zumbühl and D. Loss

Collaborators: M. Palma (SNI-PhD Student), D. Maradan, L. Casparis, A. Feschchenko, I. Khaymovich, M. Meschke, J. Pekola

Motivation

Reaching ultra-low temperatures on electronic nanodevices would allow to explore new physics such as novel nuclear/electron spin phases [1,2] and fragile fractional quantum Hall states, with applications in topological quantum computing. Implementing such experiments on a cryogen-free platform causes additional challenges due to the mechanical vibration, but this kind of systems are independent from liquid helium supply, a non-renewable resource.

Here, we present an advanced network of 16 parallel nuclear refrigerators [3] operating on a BlueFors cryo-free dilution refrigerator (DR) [4]. An advantage of our setup is that any measurement lead passes through its own nuclear refrigerator (NR, see Fig. 1) for efficient cooling, and is electrically isolated as required for transport measurements.

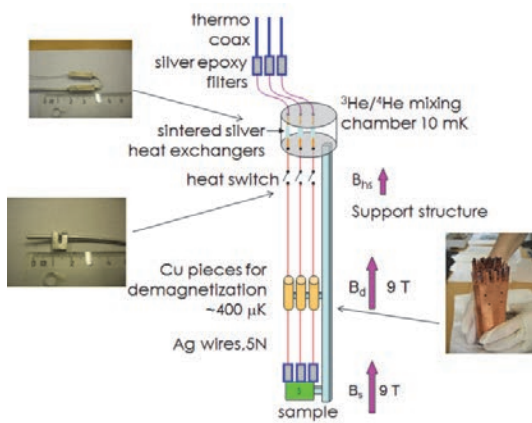


Fig. 1: Schematic of parallel nuclear refrigerator network

Introduction

We use a new method – developed in our group – for cooling nanoelectronic devices based on a nuclear adiabatic demagnetization process consisting of three steps. First, we pre-cool the nuclear refrigerant (Cu plates of 2 mol each), in a large initial magnetic field $B_i = 9$ T to a temperature of 10 mK. Second, we use superconducting Al heat switches to cut the thermal coupling between the DR and the NR. When the external magnetic field at the Al switch is $\ll 10$ mT, the Al is in the superconducting state, conducting heat only through the lattice and is essentially thermally disconnected from the DR. Finally, we adiabatically (slowly) reduce the magnetic field by a large factor $x = B_i/B_f \sim 45$. In the ideal adiabatic case, the temperature is reduced by the

same factor x . Here, we present an improved version of the previous system [3,5] which was operating in a traditional dilution refrigerator (wet system). In the new generation we improved the thermalization between the mixing chamber and the nuclear refrigerator doubling the surface area of a Ag sinters, which are made of compressed Ag nanoparticles, and consequently reducing the Kapitza resistance. In addition, we reduce the thermal resistance by doubling the wire diameter, because at this low temperature the cooling mechanism is dominated by the Wiedemann-Franz law. I will present the main requirements for a successful cooling of nano-devices, as follows.

Noise thermometry

First, to measure the electronic temperature in the NR, we implement a noise thermometer. We measure the thermal fluctuation of a high purity silver wire well connected to the Cu stage. For this, we employ a gradiometer made of a couple of pick-up coils counter-wound around the silver wire. To perform an inductive read-out of noise voltage across the gradiometer a DC SQUID is used to amplify the small voltage. In addition, we designed a superconducting double shield to protect the gradiometer against the stray magnetic fields present in our experiment. For calibrating the noise thermometer, a reference point at high temperature, where all the system's parts are perfectly thermalized, is enough [4]. As shown in Fig. 2, the noise plateau is scaling linearly in temperature according to the Nyquist relation. We observe a saturation of the noise thermometer during the demagnetization process, which may be due to a residual heat leak, e.g. due to imperfect thermalization of the superconducting shields or limited by the voltage noise of the setup.

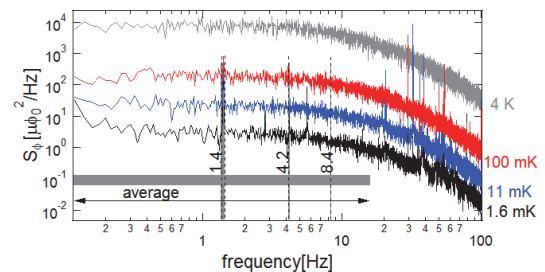


Fig. 2 Spectral power density S_ϕ vs. frequency at different temperatures. The noise plateau scales proportionally with the temperature. The dashed lines show the noise peak due to the mechanical vibration of the system

System performance

An important issue is the characterization and reduction of the background heat leak. A low heat leak in the system allows to reach lower electron temperature in the electronic device and to extend the measurement time in the ultralow temperature regime. To measure the heat leak, we precool the copper plate in finite magnetic field to increase the heat capacity of the nuclear refrigerator. Using the aluminum heat switches we decouple the copper plate from the mixing chamber. In this way the heat leak warms up the copper plate. Next, we measure the electron temperature T_e of different copper plates, with a lanthanum cerium magnesium nitrate (LCMN) thermometer and the noise thermometer, as a function of time. Using a simple thermodynamic relation between the time needed to warm up the plates and the inverse of temperature [7], we extract the heat leak and the temperature after the demagnetization process. Fig. 3 shows the measurement of the heat leak performed after a demagnetization process in an external magnetic field of 0.2 T. We observe a field dependent heat leak of the order of a few nW.

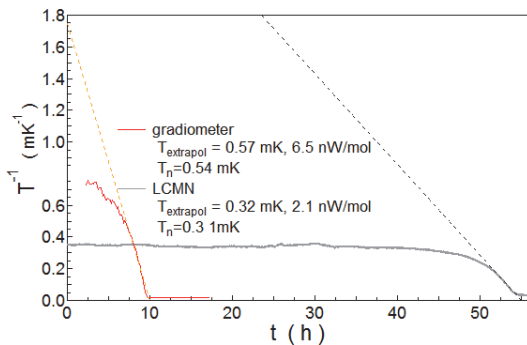


Fig. 3: The heat leak test after demagnetization referring to two different cool downs. Measured T_e^{-1} (gray line) for LCMN thermometer and (red line) for noise thermometer, theory T_e^{-1} (dashed lines) vs. t .

On-chip thermometry

Finally, the main focus of our project is to design and measure on-chip thermometers with the scope to know which electron temperature we can reach in the electronic devices. For this reason we are collaborating with the group of Jukka Pekola (Helsinki) in the development of a metallic island [5] and Tunnel

junction thermometer [6]. Both types of devices in the wet system show the same ultimate temperature around 6 mK, which is state of the art for such thermometers. In the BlueFors system they show higher temperatures around 16 mK at 7 mK base temperature due to a time-dependent heat leak. The time-dependent heat leak is presumably originating from the Ag epoxy chip carrier. For the future, we propose to optimize the thermometer design, for example with a doped substrate, to increase the thermal contact between the sample and the chip carrier.

In conclusion, our goal is to reduce the heat leak further, designing a sapphire chip carrier and socket which should minimize the effect of heat release. In addition, we are thinking to reduce the overall electrical resistance and improving the thermal contact of our measurement leads increasing the diameter of the bonding wire and eliminating the lower filtering stage. For future experiments, we are planning to investigate the back action of a charge sensing device to the quantum dot [8] and the temperature dependence of the electron dephasing time in the low temperature regime [9].

References for Project P1215:

- [1] P. Simon and D. Loss, *Phys. Rev. Lett.* **98**, 156401 (2007). P. Simon, B. Braunecker, and D. Loss, *Phys. Rev. B* **77**, 045108 (2008)
- [2] C. P. Scheller, T.-M. Liu, G. Barak, A. Yacoby, L. N. Pfeiffer, K. W. West, and D. M. Zumbühl, *Phys. Rev. Lett.* **112**, 066801 (2014)
- [3] A. C. Clark, K. K. Schwarzwälder, T. Bandi, D. Maradan, D. M. Zumbühl, *Rev. Sci. Instr.* **83**, 103904 (2010)
- [4] **D. Maradan, M. Palma, T.-M. Liu, L. Casparis, D. M. Zumbühl in preparation**
- [5] L. Casparis, M. Meschke, D. Maradan, A. C. Clark, C. P. Scheller, K. K. Schwarzwälder, J. P. Pekola and D. M. Zumbühl, *Rev. Sci. Instr.* **83**, 083903 (2012)
- [6] **A. V. Feshchenko, L. Casparis, D. Maradan, M. Palma et al. in preparation**
- [7] F. Pobell. *Matter and Methods at Low Temperatures*. Springer, Berlin (2007)
- [8] O. Zilberberg, A. Carmi, A. Romito, arxiv:1403.5879v3
- [9] A. G. Huibers, J. A. Folk, S. R. Patel, C. M. Marcus, C. I. Duruöz and J. S. Harris, *Phys. Rev. Lett.* **83**, 5090 (1999)

Energy dissipation on moiré patterns on graphene/HOPG

Project P1301 Energy dissipation over structural and electronic phase transitions

Project Leader: E. Meyer and M. Poggio

Collaborators: D. Yildiz (SNI-PhD Student), M. Kisiel, U. Gysin, and Th. Glatzel

Highly oriented pyrolytic graphite (HOPG) is a layered crystal which is composed of stacked graphene layers and has a chemically inert surface. Because there is weak van der Waals interaction between the layers, the topmost graphene layer might be shifted or rotated with respect to the rest of the crystal. Due to the rotation of the topmost layer, superperiodic structures, called moiré pattern, occur (fig. 1). Electronic and morphologic properties of these structures change depending on the rotation of the topmost layer. Although moiré patterns on graphene/HOPG system were studied by scanning tunneling microscopy (STM) [1], observation of these patterns by atomic force microscopy (AFM) is yet to be reported.

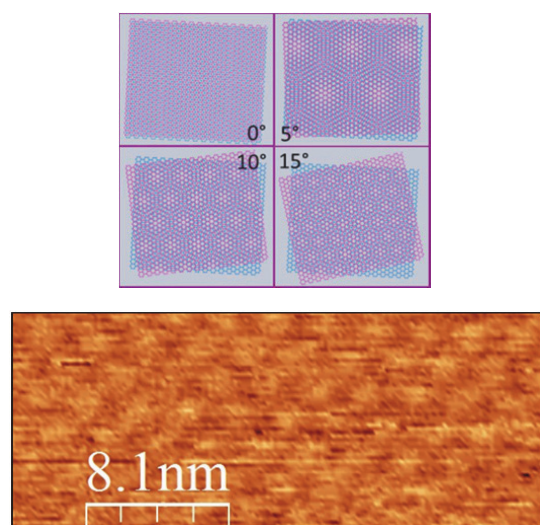


Fig. 1: Models for moiré patterns on rotated bilayer graphene with different rotation angles (top). STM data of moiré pattern on HOPG (scan parameters; $I_t = 0.4$ nA, $V_b = 100$ mV) – (bottom).

A significant scientific interest, triggered by recent discovery of graphene, is focused on frictional response of two-dimensional (2D) materials. Owing to breaking of translational symmetry, quasi-2D materials exhibit a variety of electronic and structural peculiarities, such as charge density waves (CDW) and accompanied periodic lattice distortion (PLD). Although very recently the giant dissipation was observed on NbSe₂ surface and associated with non-linear response of the CDW [2], the problem of friction in those systems still remains unexplored.

In the first step, energy dissipation measurements were performed on clean HOPG surface by means of pendulum AFM with ATEC CONT cantilevers

(force constant: 0.2 N/m), and they show the lack of electrostatic dissipation on HOPG (figs. 2 a and b). Although no significant dissipation was observed on clean HOPG, it is possible to find such dissipation on moiré/HOPG systems, in analogy to NbSe₂ samples.

At that point, observation of moiré patterns by STM is essential before investigating them by pendulum AFM. In order to combine STM and AFM, an ATEC-NCPt cantilever was tested as an STM probe and an Au surface was measured for that purpose. Herringbone reconstructions on the flat Au (111) surface were observed (fig. 2 c).

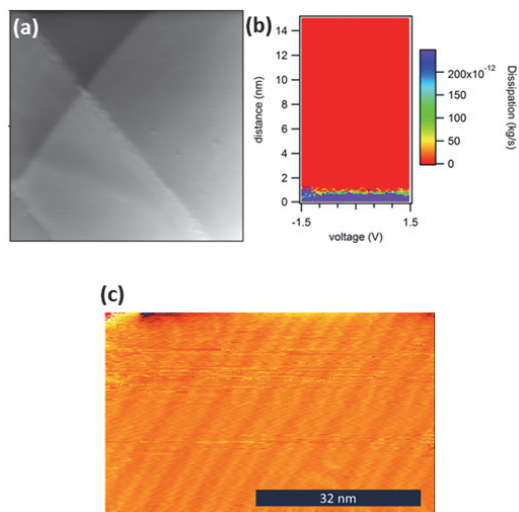


Fig. 2: (a) AFM data of HOPG. Size: $1 \mu\text{m} \times 1 \mu\text{m}$. Amplitude: 10 nm, Excitation: 40 mV. (b) Map of force-distance curves depending on a bias voltage. The map shows that there is no influence of electrostatic dissipation and also that the dissipation is independent of the applied bias. (c) STM data of herringbone reconstruction on Au (111) surface scanned by cantilever (scan parameters; $I_t = 0.5$ nA, $V_b = 1,2$ V).

References for Project P1301:

- [1] D. Yildiz, S. Sen, O. Gulseren, O. Gurlu, Apparent corrugation variations in moiré patterns of dislocated graphene on HOPG and the origin of the van Hove singularities of the moiré system, (submitted)
- [2] M. Langer, M. Kisiel, R. Pawlak, F. Pellegrini, G. E. Santoro, R. Buzio, A. Gerbi, G. Balakrishnan, A. Baratoff, E. Tosatti, E. Meyer, Giant frictional dissipation peaks and charge-density-wave slips at the NbSe₂ surface, Nature Materials **13**, (2014), 173-177

Probing the initial steps of bacterial biofilm formation

Project P1302 Dynamic and molecular principles of surface-based cell motility and mechanosensation

Project Leader: T. Pfohl and U. Jenal

Collaborators: N. Sauter (SNI-PhD Student)

Introduction

In this project, we aim to understand the initial steps of bacterial biofilm formation. We work with the model organism *Caulobacter crescentus* which is widely used for the study of the regulation of cell cycle, asymmetric cell division, cellular differentiation and biofilm formation. *Caulobacter crescentus* has two different stages in its life cycle: it starts as a swarmer cell and develops into a stalked cell after a defined time period or when it comes into contact with a surface. *Caulobacter* swarmer cells adhere to surfaces through their pili followed by irreversibly binding through the formation of a holdfast [1]. Preliminary studies have led to a model where mechanosensing occurs by pili-mediated obstruction of the flagellar rotary motor when the bacterium is close to a surface. Motor obstruction is then sensed through some unknown mechanism and transferred to the cell interior to increase cyclic di-GMP levels and to activate the holdfast synthesis machinery.

Optical trapping of bacteria

The experiments are performed using a custom built light microscope which allows for bright field and fluorescence illumination. Optical traps are generated by coupling two IR lasers into the light path. The lasers are focused through an objective and the particle or cell is dragged closely in the focus of the laser due to the transfer of momentum from the photons onto the particle. The set-up is completed with a camera, a movable stage and a microfluidic device. This allows for the quick and easy handling and exchange of the surrounding media [2].

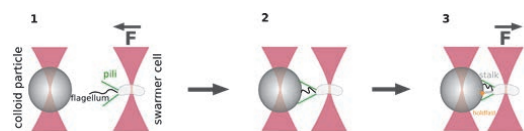


Fig. 1: A set of two optical traps is used to trap a colloid particle with one trap and a swarmer cell with the other trap. The traps are then brought in closer proximity to each other (1). The swarmer cell is allowed to attach to the particle under controlled conditions (2). The set-up allows for force measurements of the obstruction of the rotary motor and the exact distances between cell and colloid particle (3).

We are using a set of IR lasers (808 and 813 nm) to keep phototoxicity as low as possible. A way to reduce phototoxicity even further is to add oxygen scavengers into the media [3].

For our studies, a swarmer cell is caught with one optical trap and approached to the surface of a

colloidal particle, which is held by the second trap (Fig. 1). The set-up allows bringing the cells in contact to different surfaces – colloidal particles with different surface coatings – in a controlled manner. Our set-up enables the measurement of forces when the bacteria are approaching the surface, of the obstruction of the flagellar motor and in parallel of the exact distances between cell and surface. The experiments will help to gain further insights into the processes involved in mechano-sensing and adhesion of bacteria.

The first experiments are to test the effectiveness of oxygen scavengers. For this, we trap a swarmer cell, release it after a defined time period and compare its swimming speed before and after being trapped. If the speed is not significantly reduced by the trapping event, the cell is not affected by phototoxicity. For the study of the attachment process, we trap a cell, move it to the desired position, press it against the wall of the microfluidic device and measure the time it takes to attach to the wall (Fig. 2). The attaching-time and the forces generated will help to understand the impact of flagellar rotation and pili on the attachment process.

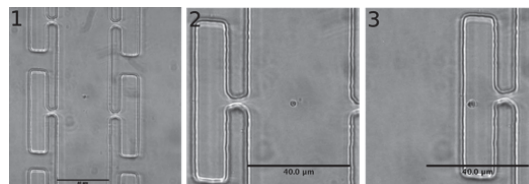


Fig. 2: Overview of the microfluidic device. The chambers generate a non-flow environment in which the experiments are performed (1). A particle is trapped and held in position by the optical trap (2). The surrounding device is then moved by the stage and the particle is placed in a chamber and brought into close proximity with the PDMS wall (3).

References for Project P1302:

- [1] D. Bodenmiller, E. Toh and Y. V. Brun, "Development of surface adhesion in *Caulobacter crescentus*", *J. Bacteriol.* **186**, 1438 (2004)
- [2] Eric Stellamanns, Sravanti Uppaluri, Axel Hochstetter, Niko Heddergott, Markus Engstler, Thomas Pfohl, "Optical trapping reveals propulsion forces, power generation and motility efficiency of the unicellular parasites *Trypanosoma brucei brucei*", *Sci. Rep.* **4**, 6515 (2014)
- [3] M. Koch and A. Rohrbach, "Object-adapted optical trapping and shape-tracking of energy switching helical bacteria", *Nature Photon.* **6**, 680 (2012)

Molecular muscles: A modular approach

Project P1303 Assembly and investigation of electrochemically triggered molecular muscles

Project Leader: M. Mayor and M. Calame

Collaborators: Y. Aeschi (SNI-PhD Student), S. Drayss-Orth, and M. Mayor

Mechanically Interlinked Molecular Switches

Supramolecular chemistry offers unique opportunities to construct mechanically interlinked molecular devices responding with shape alteration/adaptation towards physical or chemical stimuli. Sauvage *et al.* introduced the concept of a [c2]-daisy chain with switchable dimensions by exchange of a coordinating metal ion^[1]. Due to the self-complementary nature of their monomers, daisy chains are particularly appealing to construct such interlinked devices. Current examples rely mostly on crown ethers and cyclodextrins as receptors^[2]. However, it has previously been shown by our group that [c2]-daisy chains are formed by an amphiphile comprised of a water-soluble cyclophane and a hydrophobic OPE rod in polar protic solvents^[3]. By functionalization of the monomers with an electroactive moiety, the resulting dimers can respond to changes in electrochemical potential.

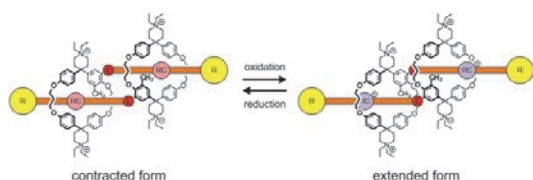


Fig. 1: Contraction/extension of a [c2]-daisy chain. The linker group is displayed in red, hydrophobic rod shown in orange. Terminal R groups in yellow represent modular functionalities like e.g. bulky stoppers or thiol anchoring groups. A redox chromophore (RC) on the rod enables to trigger between both forms electrochemically.

Modular Synthesis of Daisy Chains

Our recent investigations were directed towards a modular, synthetic approach, which allows for a convergent synthesis of amphiphilic rod structures. A large-scale synthetic route to cyclophane **2** was developed, from which highly functionalized cyclophanes **3a** and **3b** can be synthesized. **3a** incorporates a free acetylene, which can undergo Huisgen azide-alkyne cycloadditions ("click reactions") or Sonogashira cross-couplings, while the iodo-substituent of **3b** serves as reactive leaving group for various types of Pd-catalyzed cross-couplings. **3a/b** already incorporate quaternary ammonium centers, which are required to achieve solubility in polar protic solvents. In order to examine the reactivity of **3a/b** and study the influence of the bonding angle between cyclophane and OPE rod on the aggregation behavior, three exemplary amphiphiles were envisaged. By choosing different rigid linking groups, the bonding angle of the OPE rod with respect to the normal plane of the cyclophane can be controlled, which potentially allows to tune the aggregation behavior. Suzuki cross-coupling of **3a** with **OPE-1** gave amphiphile **4** in a yield of 65%.

5 was synthesized by a Huisgen cycloaddition of **OPE-2** on **3b** in a yield of 86%, while a Sonogashira cross-coupling of **OPE-3** on **3b** afforded **6** in 91%.

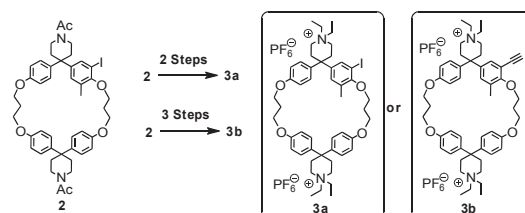


Fig. 2: Synthesis of building blocks **3a** and **3b**

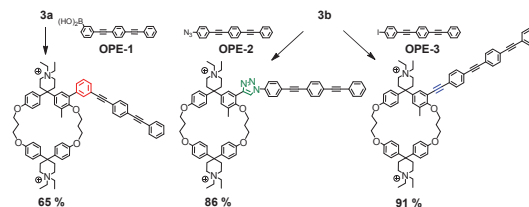


Fig. 3: Synthesis of amphiphiles **4-6** by a) Suzuki-coupling b) "click"-reaction c) Sonogashira-coupling

Conclusion

Amphiphiles **4-6** could be obtained in high overall yields and their aggregation behavior is currently under investigation by ¹H-NMR. Owing to the wide scope of applicable coupling chemistry and their late-stage derivatization, **3a/b** can serve as a versatile building block for the construction of highly functionalized daisy chains. This paves the way for the introduction of electroactive rods and the synthesis of electrochemically switchable molecular muscles.

References for Project P1303:

- [1] M. C. Jiménez, C. Dietrich-Buchecker and J-P. Sauvage, "Towards Synthetic Molecular Muscles: Contraction and Stretching of a Linear Rotaxane Dimer", *Angew. Chem. Int. Ed.*, **39**, 3284 (2000)
- [2] J. Rotzler, M. Mayor, "Molecular daisy chains", *Chem. Soc. Rev.*, **42**, 44 (2013)
- [3] J. Rotzler, S. Drayss, D. Häussinger, O. Hampe and M. Mayor, "Molecular Daisy Chains: Synthesis and Aggregation Studies of an Amphiphilic Molecular rod", *Chem. Eur. J.*, **19**, 2089 (2013)
- [4] Y. Aeschi, S. Drayss and M. Mayor, Molecular Daisy Chains: A Modular approach, *Publication in preparation*

Clearing the view: Highly transparent window supports for serial protein crystallography

Project P1305 X-FEL based dynamic studies on 2D and 3D nanocrystals of membrane proteins on solid supports
 Project Leader: C. Padeste and H. Stahlberg
 Collaborators: N. Opara (SNI-PhD Student), T. Braun, S. Arnold, X.D. Li, B. Pedrini

Structure determination of proteins is of great importance for understanding human diseases and for the design of efficient medicines. The largest contribution to protein structure determination has so far been made by synchrotron radiation-based crystallography. However, this method is limited to well-diffracting three dimensional (3D) crystals, which are in many cases hard to obtain and prone to damage during the exposure to X-rays. The measurements have to be carried out at low temperatures achieved using liquid nitrogen cooling systems.

Recently, it has been demonstrated that using the extremely short, coherent, and intense X-ray pulses produced in free-electron laser sources (XFELs), diffraction patterns from 3D protein crystals of few hundred nanometers in size can be collected at room temperature before the crystals are destroyed by the enormous energy of the pulse (“diffract-before-destroy”) [1]. In this “Serial Femtosecond Crystallography” approach, a crystal suspension is continuously delivered to the probing XFEL beam, and diffraction patterns of individual crystals hit by the X-ray pulses are collected. This strategy, however, results in an enormous waste of material. In the alternative “Fixed-Target” method, the crystal suspension is loaded on a solid support with ultra-thin windows, which is then scanned through the X-ray beam [2]. This technique has also been employed to acquire meaningful XFEL diffraction images from 2D membrane protein crystals (Fig. 1, [3]).



Fig. 1: Diffraction pattern from 2D crystals of bacteriorhodopsin obtained with a femtosecond XFEL pulse. The crystal suspension was prepared on a silicon nitride membrane support [3].

In the first part of this project, we are focusing on the evaluation and fabrication of optimized window supports for the fixed-target sample delivery. In parallel, methods for efficient and low-loss deposition of the protein crystal suspension on the supports are evaluated and implemented.

Thin membranes are obtained from silicon nitride coated silicon wafers by classical microfabrication processing consisting of photolithography, reactive ion etching, and anisotropic wet etching of silicon (Fig. 2). Arrays of windows of ten to a few hundreds of micrometers in size were produced with high yield with membrane thicknesses down to 25 nm. For photons with energies of 8.5 keV typically used for structure determination, such windows show less than 0.03 % absorption. However, as clouds of secondary electrons produced after X-ray absorption may influence the protein crystal, further reduction of the absorption is desired. This may be achieved either by using even thinner nitride films or by replacing the silicon nitride by materials containing lighter elements than silicon. Possible materials of interest include various polymers, diamond-like carbon, boron nitride, or graphene, which represents a material of ultimately low thickness and high mechanical strength. Tests using 25 nm thin films of PMMA are encouraging. However, it was found that crystalline domains in the films result in a diffuse background in the diffraction images, which may hide low-intensity diffraction peaks.

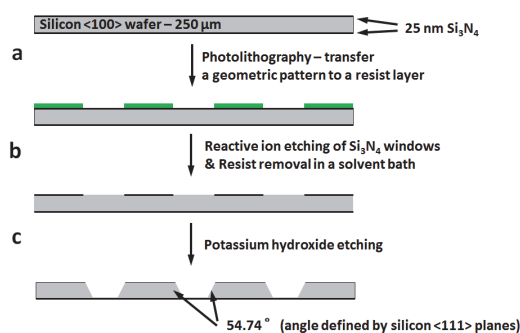


Fig. 2: Fabrication process of silicon nitride window chips. a) photolithographic structuring of a nitride coated Si<100> wafer; b) reactive ion etching of the structures into the nitride; c) anisotropic etching of the silicon. The process is self-terminating at the silicon/silicon nitride-interface.

References for Project P1305:

- [1] S. Boutet et al., “High-Resolution Protein Structure Determination by Serial Femtosecond Crystallography. *Science* **337**, 362 (2012)
- [2] M.S. Hunter et al., 2014 “Fixed-Target Protein Serial Microcrystallography with an X-ray Free Electron Laser.” *Sci.Rep.*4:6026 (2014)
- [3] M. Frank et al., “Femtosecond X-ray Diffraction from Two-Dimensional Protein Crystals”, *IUCrJ* **95**, 1 (2014).

Hydrogen bond formation during folding of an integral membrane protein

Project P1304 Folding mechanisms of beta-barrel outer membrane proteins and their catalysis by natural holdases and foldases

Project Leader: S. Hiller and D. Müller

Collaborators: P. Rios Flores (SNI-PhD Student), T. Raschle, J. Thoma, and B.M. Burmann

β -barrel membrane proteins are essential functional components of the outer membrane of Gram-negative bacteria, mitochondria and chloroplasts. Membrane proteins have highly interesting folding properties, since they fold in an external environment that comprises hydrophobic and hydrophilic phases. The biogenesis of these outer membrane proteins (Omps) poses a complex biophysical challenge to the pro- and eukaryotic cell, because the Omps are synthesized at locations distant from their target membrane. The overall essential biological function of Omp biogenesis is accomplished by molecular chaperones that pass the unfolded substrates from the ribosome to the destination membrane [1]. In the gram-negative bacterium *E. coli*, the periplasmic chaperones SurA and Skp transport the substrate to the Bam complex, which folds and inserts the substrates into the outer membrane [2]. The in-vitro and the in-vivo folding mechanisms of β -barrel Omps from mitochondria or Gram-negative bacteria are so far not understood at atomic resolution. The same polypeptide chains can refold in vitro in the absence of chaperones and other proteins, but resulting in the same three-dimensional β -barrel structures. In this project we employ structural biological and nanotechnological approaches to characterize the folding process of complex outer membrane proteins at atomic resolution.

We have adapted the hydrogen-deuterium (H/D)-exchange labeling technique, which is well established for soluble proteins [3] for the first time to integral membrane proteins. Protein refolding is initiated by rapid dilution of a denatured protein sample with micelle solution. After a variable folding time τ , the buffer is rapidly mixed with a larger volume of D_2O . In the folded state, all amide protons involved in the β -barrel are strongly protected with exchange times of the order of weeks or longer and we can thus quantify the proton occupancy for each residue in the β -barrel using 2D [^{15}N , 1H]-TROSY NMR experiments (Fig. 1). In subsequent experiments, τ is scanned through the entire folding time scale.

By our combination of H/D-exchange with NMR spectroscopy and mass spectrometry, we could characterize hydrogen bond formation during folding of the outer membrane protein X (OmpX) from *E. coli* in detergent micelles. Folding of the OmpX polypeptide propagates via a conformational ensemble state in which backbone amide protons form hydrogen bonds transiently and are thus accessible to rapid exchange with the solvent. OmpX folds from this ensemble by a rate-limiting, irreversible monomolecular reaction, with slow kinetics on the minute scale.

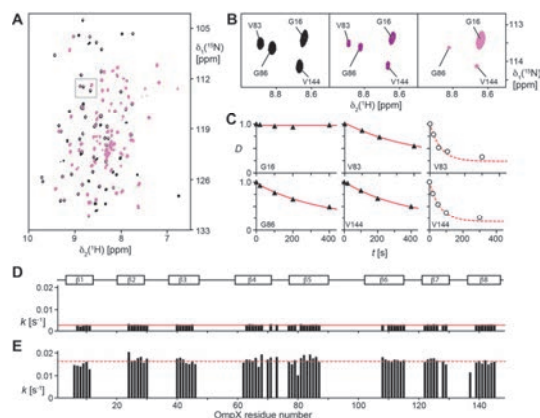


Fig. 1: Residue-specific hydrogen bond formation kinetics of OmpX folding as monitored by high-resolution NMR spectroscopy in combination with H/D-exchange. (A) 2D [^{15}N , 1H]-TROSY spectra of OmpX in LDAO micelles. Black: Spectrum after folding in H_2O -based buffer. Magenta: Spectrum after folding in D_2O -based buffer with a folding time $T = 400$ s. Peak intensities vary due to the differential incorporation of deuterium at the backbone amide position. (B) Enlargement of a spectral region containing four resonances at different folding times. Black: $T = 0$, purple: $T = 100$ s, magenta: $T = 400$ s. (C) Hydrogen bond formation kinetics during folding for the amino acid residues shown in (B). The experimental data (symbols) have been fitted to single exponentials (red lines). Black triangles and solid lines: Folding into DPC detergent; White circles and dashed lines: Folding into LDAO detergent. (D, E) Residue-specific exchange rate constants for folding of OmpX into (D) DPC detergent and (E) LDAO detergent. The horizontal lines indicate the average value for the measured rate constants. The secondary structure of folded OmpX with eight β -strands β_1 - β_8 is indicated.

Stable formation of the hydrogen bond network occurs downhill of the rate-limiting transition state and thus appears cooperative on the overall folding timescale. The insights reveal how increasing the number of hydrogen bonds funnels the unfolded polypeptide towards the native protein and thus highlight in great detail a general folding mechanism of beta-barrel membrane proteins. A publication of our work is currently in preparation [4]. We have also been able to compare the kinetic refolding data from a chaotrope denatured state with a holdase-chaperone unfolded state.

In a next step, we apply AFM-based single-molecule force spectroscopy (SMFS) to investigate the insertion and folding of completely unfolded Omp polypeptides into lipid membranes. We have previously established SMFS to follow the refolding steps of single Omps and how these steps are affected by chaperones (Fig. 2, [5]). Deflections of the AFM cantilever detect the insertion and folding attempts

of the unfolded polypeptide into the membrane. Time-resolved measurements will measure the insertion kinetics and the free energy of insertion of secondary structure elements folding one after the other until the folding process of the Omp has been completed. Overall, the combination of NMR and AFM experiments will help us to understand the factors that control and support the insertion and folding of membrane proteins into membranes.

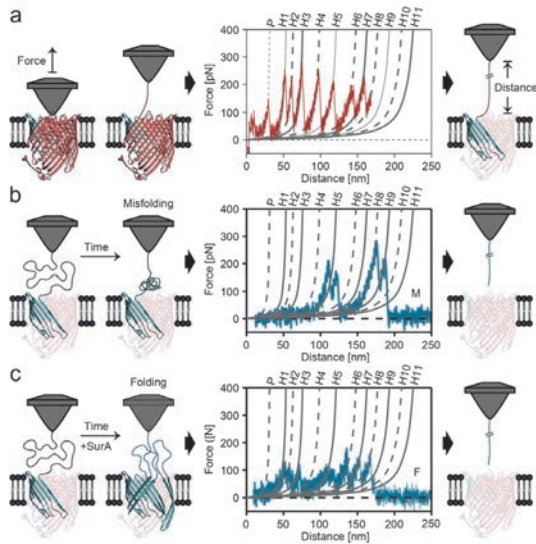


Fig. 2: Application of atomic force spectroscopy to characterize chaperone-modulated refolding of individual FhuA molecules into the *E. coli* lipid membrane. (a) Partial FhuA unfolding by single-molecule AFM. The AFM tip attaches to the N-terminal plug domain of membrane-embedded FhuA. Subsequent retraction of the tip applies a mechanical pulling force, which induces FhuA unfolding. The force-distance curve records this process with each force peak detecting an unfolding step of FhuA. The part of FhuA

unfolded (β -hairpins H1–H8) is colored red and the part remaining embedded in the membrane (β -hairpins H9–H11) is colored blue. (b) and (c) Subsequent to the partial unfolding, the AFM tip is re-approached towards the lipid membrane at a distance of ≈ 10 nm. The unfolded polypeptide can then relax for a refolding time in the range 0.1–10 s in the absence (b) or presence (c) of chaperones. During this time the polypeptide can possibly reinsert and fold into the lipid bilayer. Subsequently, the tip is retracted to characterize the emerging protein structure by force-distance measurements. In (b), force peaks not coinciding with native FhuA positions, indicate misfolding (M) of the protein. In (c), refolding in the presence of the holdase chaperone SurA results in force peaks showing native FhuA positions, indicating proper folding intermediates (F) of the membrane protein.

References for Project P1304:

- [1] T.J. Knowles, A. Scott-Tucker, M. Overduin and I.R. Henderson, "Membrane protein architects: the role of the BAM complex in outer membrane protein assembly", *Nat. Rev. Microbiol.* **7**, 206 (2009).
- [2] J.G. Sklar, T. Wu, D. Kahne and T.J. Silhavy, "Defining the roles of the periplasmic chaperones SurA, Skp, and DegP in *Escherichia coli*", *Genes Dev.* **21**, 2473 (2007).
- [3] H. Roder, G.A. Elöve and S.W. Englander, "Structural characterization of folding intermediates in cytochrome *c* by H-exchange labelling and proton NMR", *Nature* **335**, 700 (1988).
- [4] T. Raschle, P.R. Flores, C. Opitz, D.J. Müller and S. Hiller, "Hydrogen bond formation in β -barrel membrane protein folding", manuscript in preparation (2014).
- [5] J. Thoma, B.M. Burmann, S. Hiller, D.J. Müller, "Direct observation of chaperone-modulated single membrane protein folding", manuscript submitted (2014).

Nano-pills for mosquitoes to interrupt malaria transmission

Project P1306 Slow-release nano-pills for mosquitoes for interrupting malaria transmission

Project Leader: P. Hunziker and R. Brun

Collaborators: D. Gonçalves (SNI-PhD Student), X. Wang, K. Liu, P. Müller, and M. Rottmann.

Introduction

Malaria remains one of the top tropical and infectious diseases in the world, both in terms of morbidity and mortality, with an estimated more than two hundred million clinical cases every year (WHO report 2012). In recent years, the mosquito stages of the parasite life cycle have received a renewed attention with some progress being made in the so-called Transmission Blocking strategies (TBs). Some attractive targets are the stages in the mosquito midgut where a population choke point occurs, going to as few as 1-5 plasmodia per mosquito [1].

A new unconventional approach is being studied in our group combining the in-house experience of using self-assembly polymers to form drug-carrier nanovesicles, microfluidics and other tools to design a setup that could potentially be used in a cost-effective manner to lure mosquitoes into ingestion of novel anti-malarial nano-pills, that would clear, or at least reduce, the parasite density to levels that would render it non-infective and interrupt the disease transmission and propagation [2-3]. At the same time, having a mosquito survival strategy can avoid selective pressure towards the drug-free mosquitoes and by designing the system to be stage-specific and with a slow-release mechanism, one will hopefully be able to locally reduce the parasite reservoir in the field, and by exposing the least plasmodium possible to drugs, reducing the likeness of resistance to arise. The way we envision the implementation in the field would be to distribute kits for in-situ preparation of our nanovectors with sugar solutions and attractants to small community leaders in endemic regions and to strategically place these kits in water sources near the community [4].

Material and Methods

Material

240 Hera cell incubator adapted for humidity and light control. Cages for adult mosquitoes and plastic containers filled with water for pupae stages. Confocal and fluorescence microscopes, and a stereoscope adapted with fluorescence kit and ocular camera. Nanoparticles based on triblock copolymer self-assembly systems of PMOXA-PDMS-PMOXA of different lengths, terminal functional groups and covalent bond to fluorophores such as rhodamine c, phthalocyanine and fluorescein. Extrusion and size exclusion procedures for purification. Microfluidic channels prepared in-house with PDMS as substrate material. Sugar solution for mosquito

feeding: 6 % glucose, 10 % v/v corn syrup, 10 % v/v sucrose. *Anopheles stephensi* and *gambiae* as insect vectors. *Plasmodium berghei* parasites expressing m-cherry and luciferin. Atovaquone, a commercial antimalarial for humans (ETC/bc1 inhibitor) with known gametocidal activity was chosen as model drug.

Rearing conditions

Environmental chamber settings for standard experiments: T: 28 °C; Hr: 70 % (+/- 5 %); photoperiod: 14 hours of day and 10 hours of darkness with a 1.5 hours transition for dusk

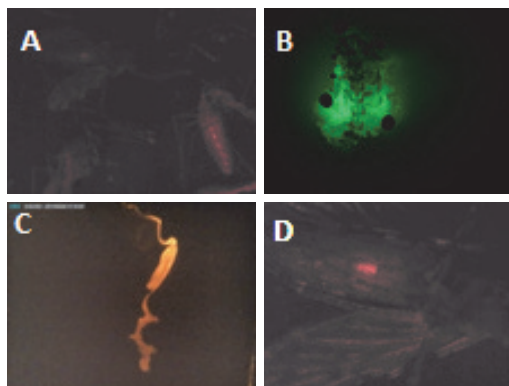
Basic setup

Encapsulation and assembly made either by microfluidic mixing of PBS and organic phase (ethanol) with polymers and drug dissolved or bulk method by slowly evaporating organic phase. Cages of 50 females of *A. stephensi/gambiae* just hatched from pupae stage. Mixing nanovectors with sugar solution. Duplicate cages at same conditions without nanovectors for control. Scan on stereoscope at certain fixed time points whole mosquitos and dissected guts, random samples selected for fluorescence microscope. Compare data for fluorescence localization and survival rate during the life span of population 2/3 weeks. Follow infection by fluorescence with m-cherry expressing parasites.

Proof-of-concept

Data collected

- Three fluorescence dyes tested in mosquito samples for imaging: rhodamine b, fluorescein and phthalocyanine.
- Encapsulation of a model drug (Tamoxifen) using microfluidics. Loading efficiency studies. Modulation of different parameters.
- Four different PMOXA/PDMS/PMOXA with rhodamine-b- or phthalocyanine-based vectors tested in feeding essays: OH₁₁; OH₁₂; COOH₇; Pip₇.
- Three different starting concentrations tested for OH₁₂: 200 µl/10 ml, 400 µl/10 ml, 800 µl/10 ml.
- Differences in longevity and behaviour by changing humidity conditions (50 % and 90 %).
- Detection of infected mosquitoes with *P. Berghei* expressing m-cherry.
- Comparison of *A. stephensi* and *A. gambiae* fed with Pip₇.



A: Stereoscope image of mixed population of female *A. Stephensi* with infected and non infected m-cherry expressing berghei; **B:** camera frame of live gut section fed with nanovector marked with rhodamine b; **C:** Fluorescent microscope image of midgut dissected after feeding with fluorescein. **D:** Single mosquito with infection in the midgut.

Analysis

From the data collected in the feeding experiments using controls with and without different nanosystems, one can safely conclude that:

- Our feeding setup with sugar water containing nanovectors seems not to influence the normal feeding behaviour of the mosquitoes.
- All nanocarriers accumulate preferentially in the mosquito midgut.
- It is possible to follow the infection and the nanovectors' presence by fluorescence imaging using a stereoscope and without dissection.
- At the initial concentrations tested (feeding every two days) no impact in life expectancy (statistical comparison between population sets of 50 individuals) seems to occur.
- Localization of nanovectors in dissected guts is possible by fluorescence/confocal microscopy.

Complete life-cycle model

To accurately assess the impact of our nanosystem and in particular the efficacy of certain drug in clearing parasites in the mosquito stages and avoid transmission to another host, one must establish a model that can follow the parasite life cycle from end to end. The solution found was to design an

experiment that follows infection from mice to mosquito and then to mice again. *P. falciparum* was replaced by *P. berghei* (an exclusive rodent infecting strain), genetically modified to express a fluorescence protein (m-cherry) and luciferin (luminescence emission when fed with the appropriate substrate), and the mosquito vector *Anopheles gambiae* by *Anopheles stephensi*. With this model, one is capable to test the impact of different systems in all stages of parasite development. The model is being established in collaboration with the Swiss TPH and is in the process of getting an animal license for our project to work independently.

Summary and outlook

The project is now reaching phase II of the initial proposal. The concept has been tested and an experimental model established. The nanovectors are being optimized and a release system is currently being studied. The next steps of the project are to establish a stochastic model relating the decrease of mosquito infection levels with the transmission of parasites to the rodent host; long term stability of drug-loaded nanovectors in sugar solutions and harsh conditions, developing an automated imaging setup to acquire fluorescence signals from large populations of mosquitoes at once and *in situ*, follow evolution and optimize localization of nanovectors in single specimens with a higher resolution fluorescence microscope; establish a cellular in-vitro model for testing the release and targeting systems and testing different setups for field applications, including attractants and volatiles to attract mosquitoes.

References for Project P1306:

- [1] Ranford-Cartwright, *Spreading the seeds of million-murdering death: metamorphoses of malaria in the mosquito*, TRENDS in Parasitology, 573-580 (2005)
- [2] Broz P. *Nanotechnologies for targeted delivery of drugs*, Wiley-VCH, 3731-3732 (2007)
- [3] Ben-Haim, **Cell-Specific Integration of Artificial Organelles Based on Functionalized Polymer Vesicles**, N. Nano Letters, 1368-1373 (2008)
- [4] Knols BGJ, *Odour-mediated host-seeking behaviour of the Afro-tropical malaria vector Anopheles gambiae Giles*, Parasitology Today, 159-161 (1996)

First steps towards optoelectronic nanojunctions

Project P1307 Optoelectronic nanojunctions

Project Leader: M. Calame and M. Mayor

Collaborators: J. Overbeck (SNI-PhD Student), A. Vladyka, K. Thodkar, and M. El Abbassi

Introduction

Over the past decade, the field of single molecule electronics has revealed a variety of novel effects [1]. In this context, the mechanically controllable break junction technique (MCBJ) proved itself a choice experimental approach to unravel the electronic transport properties of individual molecules [2]. The interaction of light with electrical transport in molecular junctions, however, has been only barely investigated and attracts growing interest as a method to gain further insights and to control these systems [3].

In this project, we want to investigate the optoelectronic properties of molecular junctions consisting of organic molecules within two contacting electrodes. To this end, a new break junction setup will be developed and adapted to fit into multiple optical microscope setups. Additionally, we will investigate modifications to the sample design to incorporate graphene as an electrode material and exploit plasmonic effects that can be tuned through the mechanically controlled electrode separation. Jan Overbeck has been enrolled in the SNI doctoral program since mid-october 2014.

Sample fabrication

As a prerequisite for more advanced experiments, an optimization of the break junction chips has been the focus of the first few weeks with the support of A. Vladyka. In particular, the sample fabrication by electron-beam lithography has been adapted to improve control over the exact junction geometry and to speed up fabrication.

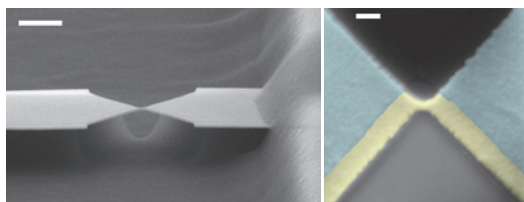


Fig. 1: **Left:** Free-standing gold bridge protected by polyimide except for underetched junction area. Scale bar 1 μm . **Right:** Top-view of the junction area. The width of the junction is 80 nm and the pure gold junction area (yellow shading) can clearly be distinguished from the area with the titanium adhesion layer underneath (blue shading). Scale bar 200 nm.

Additionally, as a first step towards its use as an electrode material, we have shown the successful transfer and adhesion of graphene on break junction samples. We benefited here from the help of K. Thodkar and M. El Abbassi who are currently wor-

king extensively on the chemical vapour deposition (CVD) of graphene and its transfer optimization to various substrates.

Setup design for optoelectronic measurements

To perform optoelectronic measurements, the design of the existing setup for mechanically controlled break junction experiments is currently being adapted to accommodate the following objectives:

- Integration of the mechanical setup within an inverted optical microscope and an existing confocal Raman setup.
- Possibility to mechanically open and compress the junction beyond neutral position.
- Integration of temperature control and readout

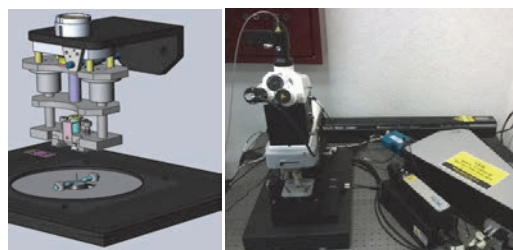


Fig. 2: **Left:** CAD-Drawing study of a possible break-junction configuration for an optical microscope. **Right:** Raman setup giving the geometric framework for design considerations.

Outlook

Over the coming months, we will finalize the design process and start building the optoelectronic setup. Additionally, we plan to expand on the sample geometry to incorporate structures for the in- and out-coupling of light.

Acknowledgements

We thank Peter Makk and Heinz Breitenstein for fruitful discussions.

References for Project P1307:

- [1] See e.g. Focus issue on Molecular electronics, *Nature Nanotech.* 8, 377-467 (2013)
- [2] Z. Li, et al., *J. Am. Chem. Soc.*, **136**, 8867 (2014); J. Brunner et al., *J. Physics: Cond. Matt.*, **26**, 474202 (2014); S. Wu, et al., *Nature Nanotech.* **3**, 569 (2008)
- [3] M. Galperin and A. Nitzan, *Phys. Chem. Chem. Phys.* **14**, 9421 (2012)

Nanostructures of nuclear pore complex

Project P1310 Plasmonic Sensing in Biomimetic Nanopores
 Project Leader: Y. Ekinici and R. Lim
 Collaborators: D. Sharma (SNI-PhD Student)

Nuclear pore complex (NPC) is an important proteinaceous assembly in eukaryotic cells, which controls exchange of biomolecules through the nuclear membrane. Translocation channels in NPCs are filled with Phenylalanine glycine nucleoporins (FG Nups) that allow passive transport of molecules with mass ≤ 40 kDa and restrict the passive translocation of larger molecules. These macromolecules (> 40 kDa) get access via selective binding after attachment with nuclear transport receptors such as importin β . In this selective translocation of macromolecules, FG Nups play a critical role and therefore it is important to study the effect of micro- and nano-pathways of FG Nups on transportation of nuclear protein cargo-nuclear transport receptor complexes. In the future, this understanding will be employed for the fabrication of two-dimensional NPC structure. Two dimensional NPC structures will be useful for the study of selective and controlled reaction between biomolecules, and drug discovery.

Our current focus is to fabricate nano-pathways of FG Nups and examine the selective transport of colloidal particle bearing nuclear transport receptors (see Fig. 1). Top-down lithography process will be used for patterning along with suitable passivation techniques. Fabrication and patterning work will be done on glass substrate.

To accomplish the nano-structures of FG Nups, it is necessary to passivate the unpatterned area against proteins. Therefore, three passivation methods have been studied in the past few months to optimize the passivation techniques for FG Nups. These methods are as follows:

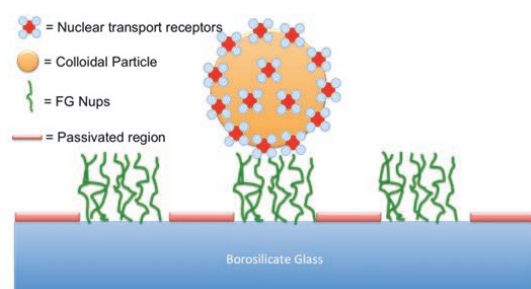


Fig. 1: Schematic of one-dimensional walk of a colloidal particle, bearing nuclear transport receptors, on FG Nups' pathways.

Fluorocarbon polymer: Fluorocarbon polymer was synthesized on glass substrate using reactive ion etching and was further characterized using contact

angle measurements and XPS. Passivation against FG Nups has been investigated for the prepared fluorocarbon polymer layer. Results show that non-selective binding affinity of polymer layer for FG Nups changes with the density of the polymer layer.

PEG Silane: Poly-ethylene glycol Silane is coated on glass substrate after piranha cleaning. To check the passivation efficiency of PEG-Silane, FG Nups 153, 62, 98 and 214 are used for non-selective binding. Results show that PEG Silane passivates substrates effectively against FG Nups (see Fig. 2). To proceed further with the obtained results, the plan is to use PEG-based passivation and top-down nano-patterning using optical and e-beam lithography.

Photocleavable PEG: EG₇NPEOC-APTES (Septa-ethyleneglycol nitrophenylethoxycarbonyl-protected aminopropyltriethoxysilane) contains a photocleavable protecting group that can be deprotected via UV light exposure. In order to examine the non-selective binding efficiency of photocleavable PEG for FG Nups 153, experiments are performed. Results show that the unexposed NPEOC molecules have high affinity for non-selective binding with FG Nups 153 comparative to exposed molecules. Hence, based on differences in the reactivity of exposed or unexposed molecules with FG Nups, it can be further used for protein immobilization.

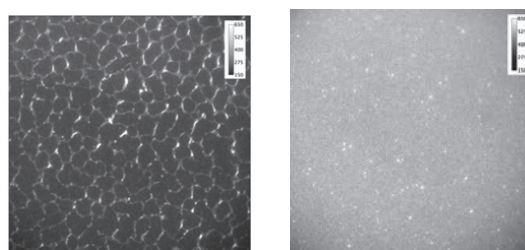


Fig. 2: (Left) Passivation of glass substrate against FG Nups 153 using PEG-Silane and (Right) attachment of FG Nups 153 on glass substrate.

References for Project P1310:

- [1] K. D. Shleicher, S. L. Dettmer, L. E. Kapinos, S. Pagliara, U. F. Keyser, S. Jeney and R. Y. H. Lim, "Selective transport control on molecular Velcro made from intrinsically disordered proteins", *Nature Nanotechnology* **9**, 525 (2014)

Calixarene-based Langmuir-Blodgett film stabilization by inorganic supramolecular clips

Project P1308 Supramolecular charge and spin architectures produced by chemical clipping

Project Leader: P. Shahgaldian and T. Jung

Collaborators: M. Moradi (SNI-PhD Student) and L. Tulli

Introduction

The increasing capabilities to organize monomolecular layers on surfaces has raised expectations that bottom-up nanostructuring procedures will find their role in technologies like sensors, data storage or even logic devices. [1]. Organized surface layers for a wide range of applications have been produced, for example by the self-assembly of alkanethiols on noble metals [2]. An alternative approach for the production of well-ordered films on solid surfaces is the Langmuir-Blodgett (LB) technique. It allows for the deposition of single layers, or multilayers, of water-insoluble amphiphiles on solid substrates and includes the possibility to control the packing density of the deposited film. Problems associated with the homogeneity and stability of LB films have strongly limited their applications. In order to tackle this issue, several strategies have been developed. For example, Regen demonstrated that LB films produced with poly-cationic amphiphiles could be stabilized using polyanionic polymers [3]. Recently, we demonstrated a novel and effective strategy to prepare stable LB films using supramolecular clips [4]. The amphiphiles' positive charges at their polar head are stabilized by small organic "clips" that possess negative charges in a favorable *syn*-position. By this clipping, also *monomolecular* films and not only bilayers can be transferred from the assembly trough to solid substrates.

In the present project, we aim at extending the clip stabilization approach towards a more general and novel approach of surface supramolecular engineering. It is based on the use of macrocyclic amphiphiles bearing several metal coordination ligands at their polar side. The building blocks will be produced by chemically "decorating" calixarene macrocycles, a class of molecules widely used to produce designer amphiphiles.

Results

As a first model amphiphile, we produced a calixarene macrocycle bearing four carboxylic functions at the upper rim and four short aliphatic chains at the lower rim; cf. Fig. 1. The self-assembly of this macrocycle, at the air water interface, was studied using the Langmuir balance method and Brewster angle microscopy (BAM). We could demonstrate that in spite of the short length of its aliphatic chains, **1** could self-assemble and form stable and well-defined monomolecular layers. In the presence of CuCl_2 in the aqueous subphase, the monolayer showed a different behavior suggesting an interaction between the carboxylate functions of the amphiphile and Cu^{2+} ions; cf. Fig. 2.

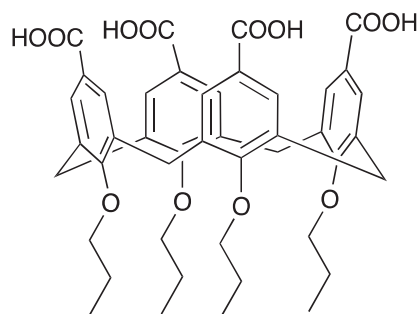


Fig. 1: Chemical structure of calixarene macrocycle **1**.

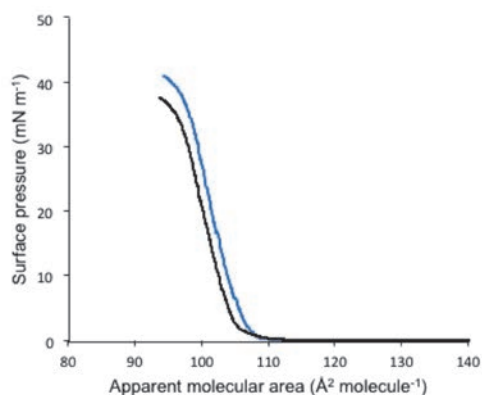


Fig. 2: Π/A isotherm of **1** measured on water (—) and 10^{-5} M CuCl_2 (—) subphases

The compression isotherm of the monolayer of **1** on pure water indicates that the amphiphiles form a stable monolayer at the air-water interface. According to the compression isotherm curves, the takeoff (A_0) and collapse area (A_c) values of **1** on water are similar to those measured on CuCl_2 . Interestingly, the collapse pressure (π_c) value on CuCl_2 is lower than that measured on pure water indicating that the amphiphiles interact with Cu^{2+} ions at the air-water interface.

The morphology of the monolayer of **1** on pure water and on a 10^{-5} M CuCl_2 solution was investigated by Brewster angle microscopy (BAM) (Fig. 3). The monolayer of **1** on pure water shows domains of different contrast suggesting the presence of organized, i.e. anisotropic domains with distinct molecular organization/directions.

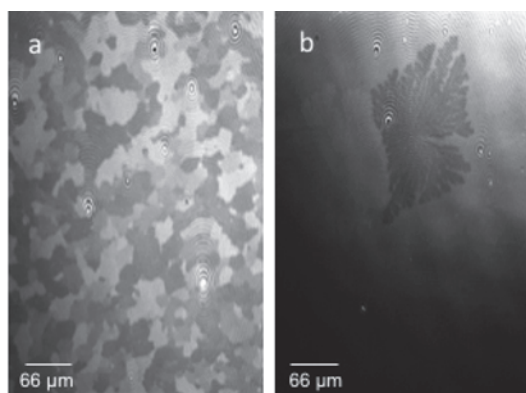


Fig. 3: Brewster angle micrographs of the monolayer **1** on pure water (a) and on CuCl_2 subphase.

In the presence of Cu^{2+} ions at a concentration of 10^{-5} M, large dendritic domains are observed, suggesting that Cu^{2+} ions interact with the monolayer of **1** at the air-water interface causing the formation of crystalline domains of the amphiphiles.

The possibility to transfer Langmuir monolayers of **1**, after stabilization by Cu^{2+} ions, from the air-water interface onto a solid substrate was assessed by using the Langmuir-Blodgett deposition technique. The transfer of the monolayer turned out to be successful with a transfer ratio of 1 ± 0.1 . Surface ellipsometry measurements carried out on the so-produced films confirmed the presence of a monolayer on the substrate surface with a thickness value of 1.0 ± 0.2 nm. This value is consistent with the presence of a monomolecular film of **1** in a densely packed phase with the pseudo C_4 symmetry axis of the calixarene macrocycles oriented orthogonal to the air-solid interface. These layers were further characterized using field-emission scanning electron microscopy (FE-SEM) and atomic force microscopy (AFM); the results are presented in Fig. 4. Both these experimental techniques confirm the presence of a 1 nm-thick layer at the surface of the solid substrates.

Conclusion

For the first time, we demonstrated that macrocyclic amphiphiles can be stabilized by transition metal ions to be successfully transferred onto solid substrates using the Langmuir-Blodgett deposition method. Clearly, there is a transition from an anisotropic, presumably amorphous or 2D fluid, phase to a crystalline phase at higher densities of **1** and the formation of at least a dendritic sub-phase by the addition of CuCl_2 to the water in the LB trough. The work is underway to characterize, at the molecular level, the architecture of the floating and of the transferred films using optical techniques as well as scanning probe microscopy and synchrotron-based characterization techniques after transfer. The here-

established approach of molecular clipping will be expanded to other macrocyclic amphiphiles and other transition metal ions towards the goal of architecting increasingly functional 2D layers.

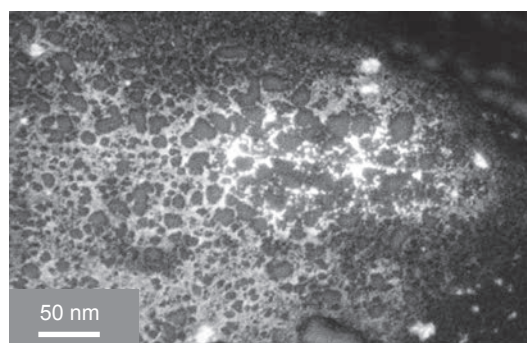
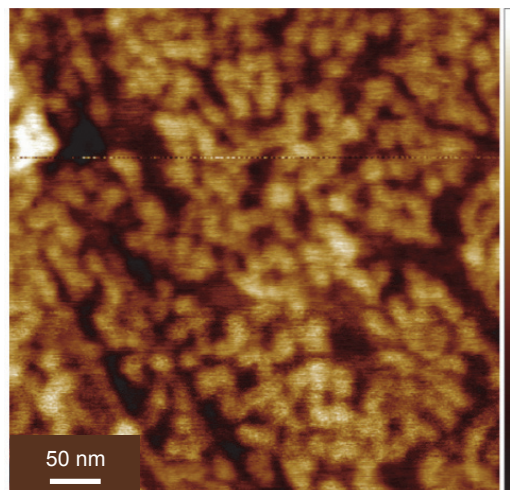


Fig. 4: AFM (top) and FE-SEM (bottom) micrographs of monolayers of **1** transferred onto solid substrates using the Langmuir-Blodgett technique.

References for Project P1308:

- [1] A. G. Slater, P. H. Beton, and N. R. Champness, "Two-dimensional supramolecular chemistry on surfaces", *Chem. Sci.* **2**, 1440 (2011)
- [2] J. C. Love, L. A. Estroff, J. K. Kriebel, R. G. Nuzzo and G. M. Whitesides, "Self-Assembled Monolayers of Thiolates on Metals as a Form of Nanotechnology", *Chem. Rev.* **105**, 1103 (2005)
- [3] X. Yan, V. Janout, J. T. Hsu and S. L. Regen, "The Gluing of a Langmuir-Blodgett Bilayer", *J. Am. Chem. Soc.* **125**, 8094 (2003)
- [4] N. Moridi, C. Wäckerlin, V. Rullaud, R. Schelldorfer, T. A. Jung and P. Shahgaldian, "Langmuir-Blodgett monolayer stabilization using supramolecular clips", *Chem. Commun.* **49**, 367 (2013)

Low-temperature bonding of multichip modules by nano-size silver sintering

Project A7.4 Nano-LTB (PSI, FHNW, ABB Switzerland Ltd. Baden-Dättwil)

Project Leader: H. Van Swygenhoven

Collaborators: S. Zabihzadeh, L. I. Duarte, Ch. Kähr, S. Van Petegem, N. Hofmann, A. Wahlen

Introduction

Although silver has been investigated as bonding material since 1980, it has not been largely applied in the high-temperature packaging industry. This can be referred to the limited knowledge on the mechanical behavior of this material, which is in part due to a lack in appropriate micro-testing devices as well as the difficulty to prepare samples. As a consequence, high-lead contained solder material is still being used as high-temperature die-attach technique which, of course, has obvious environmental consequences (ROHS). In this work, we perform an in-depth analysis of the microstructure and mechanical behavior of porous silver layers in order to better understand this material and to make predictions for optimizing the relation between microstructure and mechanical behavior possible. The obtained experimental data will further serve as input parameters for a lifetime simulation model. The final goal is to improve the reliability of the sintered layers in the temperature range of -55 °C to 250 °C.

Experimental results

The free-standing layers (~25 µm) are produced by a pressure-assisted sintering method in the pressure range of 4 MPa to 12 MPa and temperature range of 210 to 300 °C. The microstructure is characterized in terms of bulk porosity, grain size and defect structures using electron microscopy and X-ray nano tomography. The mechanical behavior of the layers is investigated by in-situ tensile testing at the Materials Science beamline of the Swiss Light Source on dog-bone-shaped geometry samples. Representative SEM images of two samples are presented in Fig. 1 (a & b). Here, S1 is the sample which is sintered at the lowest pressure, temperature and time, and S2 is the one sintered at maximal pressure, temperature and time. Analysis of the grain size distribution is presented in Fig. 1(c) which evidences strong dependency of grain size on sintering conditions. S1 has a narrow distribution with a mean value of 98 nm; S2 has a broad distribution extending from 100 to around 600 nm with a mean value of 294 nm.

The reconstructed x-ray nano-tomography images of S1 and S2 samples are presented in Fig. 2 (a and b). Fig. 2 (c), compares the pore size distribution. In both samples, most of the pores are in the range of 200-300 nm. The bulk porosities derived for S1 and S2 are 34 % and 19 %, resp., corresponding to densities of 6.93 gr cm⁻³ and 8.5 gr cm⁻³, resp. In these results, one has to take into account that pores with a diameter smaller than 100 nm are not detectable.

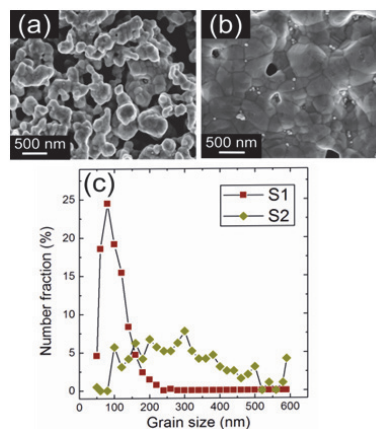


Fig. 1: SEM images for (a) S1 and (b) S2, and (c) grain size distribution of S1 and S2.

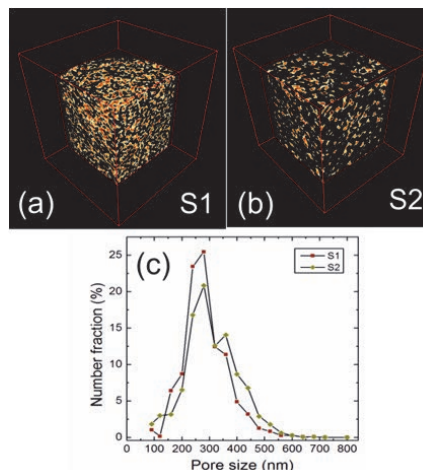


Fig. 2: The nano-tomography reconstruction images for (a) S1 and (b) S2 nano-silver, (c) the pore size distribution of S1 and S2

Fig. 3 displays dark field (DF) TEM images of samples S1 and S2 before (a & b) and after (c & d) tensile deformation. A large density of twins and dislocations are observed in both cases; independent on the sintering conditions, samples are plastically deformed during pressure-assisted sintering process. The limited number of observable grains does not allow to quantitatively comparing the twins and dislocations densities before and after deformation. To overcome this limitation, in-situ tensile tests are performed in order to gather information about the samples during deformation.

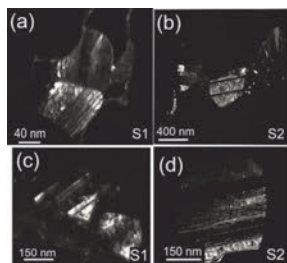


Fig. 3: DF/TEM images from S1 before (a) and after (c) tensile deformation, and from S2 before (b) and after (d) tensile deformation.

Fig. 4 (a and b) displays the stress strain curves of S1 and S2 which are deformed at room temperature during load-unload tensile cycles at strain rate of $0.003\%s^{-1}$. Both samples show large hysteresis and brittle behavior with low strain. A significant difference in flow stress of the samples is observed. S1 reaches a stress around 20 MPa, while ultimate strength for S2 rises up to 100 MPa. The stress-strain curves of the samples deformed at elevated temperature ($T=150\text{ }^{\circ}\text{C}$) are shown in Fig. 4 (c and d). Here, S1 and S2 exhibit more ductile behavior with larger strain. Large differences in macroscopic strain and ultimate strength are observed for these samples.

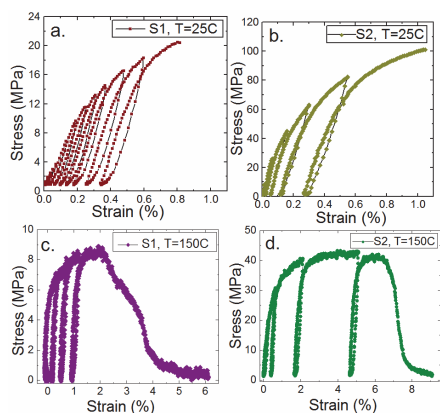


Fig. 4: Stress-strain curves of S1 (a) at room temperature, (c) at $T=150\text{ }^{\circ}\text{C}$, and of S2 (b) at room temperature and (d) at $T=150\text{ }^{\circ}\text{C}$ for a series of load/unload cycles.

Fig. 5 a displays the width of the (200) reflections at maximum load, immediately after unloading and after relaxation as function of the maximum applied stress in each cycle. Figure 5b shows the FWHM of the (111) reflection as function of macro-strain. The arrows shown for the last loading cycle show that the strain just after unloading is smaller due to elastic contraction, and that, after relaxation, a large amount of inelastic strain is recovered: similar trends are observed for all measured diffraction peaks. In both samples, a large percentage of the peak broadening is recovered upon unloading. This effect is more important in S1. The larger strain recovery and FWHM after unloading of S1 suggests that less strain is produced by mechanism such as mechanical twinning and/or dislocations in this sample compared to S2.

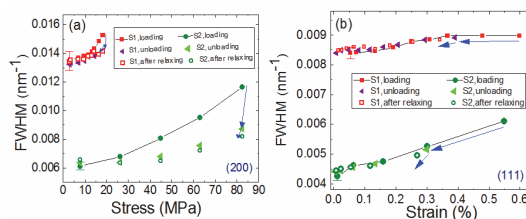


Fig. 5: (a) the FWHM of (200) planes as the function of stress, and (b) the FWHM of (111) planes as the function of macroscopic strain for loading, unloading and relaxing states of S1 and S2.

The broadening of the diffracted peaks as function of the scattering angle (Williamson-Hall plot), are presented in Fig. 6 prior to loading, during loading and after unloading. The shape of the WH in S1 hardly changes during loading and takes the same shape after unloading. On the other hand, in S2, the shape of the WH plot changes during loading and the new shape is kept after unloading. In S2, the FWHM of the (200) and (311) families have increased more compared to the other reflections, which points resp. to the presence of mechanical twinning and dislocation mechanisms. The WH plots support the view that after deformation of S1 there is no additional storage of dislocations and/or twins; however, this is not the case for S2.

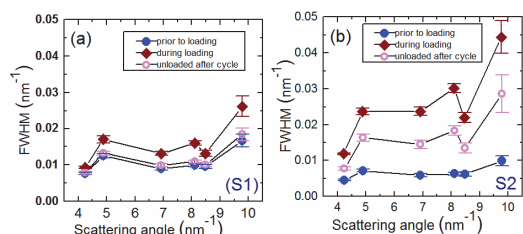


Fig. 6: Williamson-Hall plot of (a) S1 and (b) S2, for prior to loading, during loading and unloaded after cycle states.

Summary:

In summary, by increasing the sintering temperature and pressure, significant grain growth occurs, while the pore size distribution seems to be less affected by the sintering conditions. Depending on the volume fraction and distance between the pores, two competing deformation mechanisms can be defined. In S1, with the larger porosity and more closely packed pores, the deformation is mainly controlled by the pores themselves, although the effect of intra-granular deformation should not be ignored. On the other hand, in S2, the sample with lower porosity, deformation occurs mainly intra-granularly with more important contribution of dislocations. However, the role of porous structure in the recovery mechanism should not be ignored.

Outlook:

As next step in the planned research, a micro-structure-based model will be developed in order to establish the relation between the volume fraction and distance between the pores with the mechanical behavior of the material.

Nano-capsules for active textile cooling

Project A7.5 NanoFACTs (FHNW, University of Basel, HeiQ Materials AG Bad Zurzach)

Project Leader: U. Pielers

Collaborators: J. Grognum, O. Braissant, C. Bradbury, M. Height, W. Bender

Concept

Regulation of the human skin temperature can be of great importance in particular for personnel wearing protective clothing in environments of extreme conditions e.g. fire fighters or rescue personnel. Critically, these protective clothing impair the body's natural cooling mechanisms, building up excessive heat providing additional stress and discomfort and consequently could compromise crucial decisions. Therefore, textiles providing active cooling mechanism worn under insulating protective clothing are highly desirable.

The objective of the project was to advance the application of functional textiles exhibiting active cooling by tailoring the capsule size. Presently, the durability of encapsulated active materials has shown limited application because the capsule size was significantly larger than the fiber diameter. However, by decreasing the capsule size, one also reduces the amount of active material that is captured, therefore reducing the overall effect. A range of capsule sizes was needed to determine the optimal compromise between durability and intensity of the effect. As existing encapsulation methods were not very suitable to produce capsules in the range of 100-10'000 nm, new approaches were required.

Capsule formation

The project was defined around the core active material, giving the semi-permeable nano-capsules their energy-absorbing properties e.g. cooling effect (schematic diagram of the principle in Fig. 1). The choice of compounds to be entrapped is one of the keys for the efficiency of the capsules and therefore the success of the project. Many of the so-called sugar alcohols (or polyols) under their crystalline form present a negative heat of solution. In other words, when entering in contact with water (sweat), the polyol starts dissolving in an endothermic process, hence generating a refreshing sensation. The effect is regenerated by drying the textile without use of high energy consumption like it can be the case for phase-change-material-based technology. The literature being scarce on the topic, we defined and tested a series of potentially active components with a large molecular weight range for their heat of solution. Xylitol under its crystalline form presented the most interesting negative heat of solution at 35 °C (-157.5 J/g). Sorbitol was finally selected as alternative to xylitol as the molecule displayed an interesting heat of solution (-104.0 J/g) combined with a larger molecular size, allowing for a more durable entrapment of the molecule, reasonable cost and a slightly different, slower profile of solubilization which could offer a more progressive, longer lasting cooling effect.

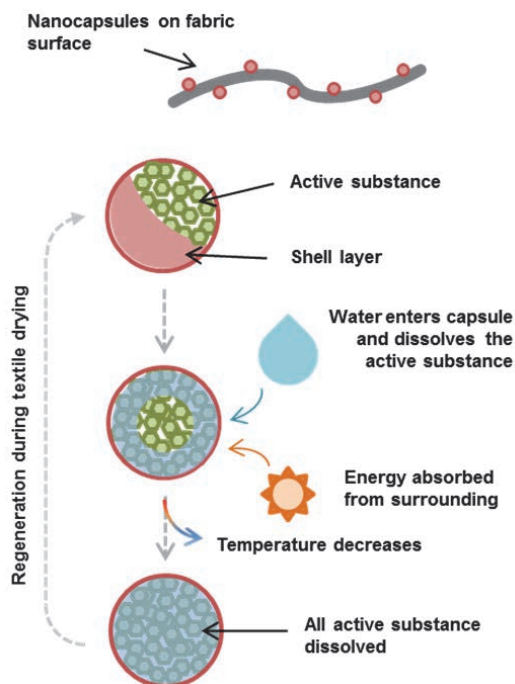


Fig. 1: Dissolution cooling principle: schematic diagram showing the dissolution of the cooling material by water.

It was decided to form the capsules using emulsion-polymerization with, as starting point, a strategy similar to the one published by Salaün *et al.* [1], who formed micro-capsules of xylitol in a size range of 13 to 25 µm. Emulsions are a particular system of the 2-phases matter referred to as colloids. They are composed of at least two immiscible liquids: the continuous phase and the dispersed phase. As the molecules to be entrapped are hydrophilic and the chemistry to form the shell is hydrophobic, the type of emulsions that has been developed is a so-called water-in-oil emulsion. In order to be able to achieve the targeted, very small size of capsules (~100 nm), a particular emphasis has been put on the selection of the continuous phase and surfactants. The emulsions were prepared using a high-speed disperser for which the best conditions (time, speed and temperature) had to be defined. The highly viscous mineral oil has been finally selected as continuous phase, as it helped stabilize the emulsion. Furthermore, the low cost of this solvent would help keep the cost down for a potential large scale production. Most of the work focused on the nature of the surfactants to be used, the composition of the mixture (two or three components), and hydrophilic-lipophilic balance value in order to achieve the smallest possible droplets within a stable system that would allow for the formation of the shell via cross-linking. The monomer chosen to produce the capsule shell was 4,4'-methylenebis(phenyl isocyanate) for its

reactivity at lowest temperature – needed to avoid an inversion of the emulsion – and its inert nature once fully reacted [2], which is an absolute necessity, as the capsules are intended to be in direct contact with the customer's skin.

Capsules' cooling performance

We could produce capsules as small as 260 nm (average diameter, Fig. 2) and as large as 1500 nm (average diameter) with either active material. The capsules were then assessed for their cooling performance by microcalorimetric measurements (performed by O. Braissant, Uni Basel). The achieved performance was excellent with a measured enthalpy of solution in the range of -100 J/g of material for capsules containing up to 40 % xylitol. Similarly, the nano-capsules containing sorbitol displayed a measured enthalpy of solution of about -60 J/g of material for an equivalent load of active compound.

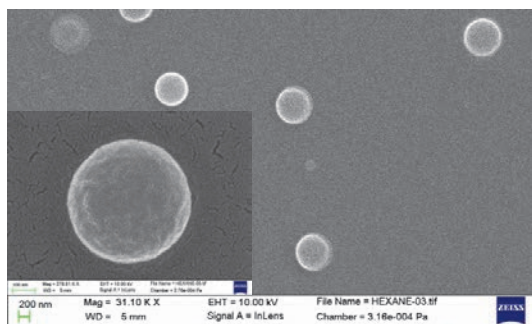


Fig. 2: SEM micrograph of typical capsules. The inset is a high magnification of one capsule.

Application on textile fibers

The next step was the application of capsules on actual textile fibers. Our partner HeiQ Materials AG provided the textile material under the form of a synthetic fabric treated with their proprietary Adaptive® finishing technology. HeiQ Materials AG also performed the cross-linking of the capsules on the fibers (Fig. 3) with various amount of nano-capsule concentration in the liquor. It provided a range of samples with various loading of capsules on the textile surface. This was meant to help determine the appropriate amount of material needed for the targeted performance and to test the differences in terms of feel of the functionalized textile. The performance observed in the microcalorimetric measure-

ments for the highest nano-capsule loading (6.7 % weight in the padding liquor) consumed, after addition of water, up to 0.42 mW/cm². Once extrapolated to the size of a technical shirt, one could expect a power consumption of approximately 3.3 W for the textile functionalized with xylitol nano-capsules, well in accordance with the initial target. This would represent the absorption of the excess power developed under an intense effort for approximately 1h, which could be sufficient for most emergency missions of rescue personnel.

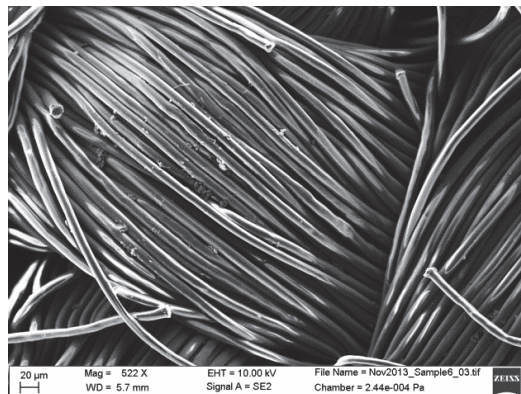


Fig. 3: SEM micrograph of capsule-functionalized textile fibers.

We could successfully synthesize active nano-capsules with a demonstrated cooling effect for potential applications on technical textiles aimed at rescue personnel. The technology could also be applied to technical clothing dedicated to recreational activities, for example. Effective functionalization of textile fibers with the nano-capsules was achieved, and their effect measured on fabric samples reached the target of 1 to 5 W absorbed as defined in the specifications.

References for Project A7.5:

- [1] F. Salaün, G. Bedek, E. Devaux, D. Dupont, D. Deranton, "Investigation of water absorption and diffusion in microparticles containing xylitol to provide a cooling effect by thermal analysis", *International Journal of Thermophysics* **30**, 1242 (2009)
- [2] C. U. Dornhel, "Health hazards associated with polyurethane foams", *Journal of Occupational and Environmental Medicine*, **8** (1966), 59-62

Nanostructured surfaces for the control of polymorphism of active pharmaceutical ingredients

Project A7.6 NanoMorph (FHNW, PSI, RPD TOOL AG Muttenz)

Project Leader: P. Shahgaldian

Collaborators: L. Tulli, N. Moridi, W. Wang, D. Vaknin, K. Helttulinen, B. Schneider, W. Meier, and T. Jung

Solid-state polymorphism is defined as the ability of a substance to exist as two or more crystalline phases^[1]. Polymorphism of active pharmaceutical ingredients (APIs) is of crucial importance for the pharmaceutical industry. Distinct polymorphs of the same API may possess different physicochemical properties, with a direct influence on the therapeutic activity of the final drug. The US Food and Drug Administration (FDA) identifies each polymorph of an API as a patentable entity. Control over the polymorphism of APIs is commonly achieved by tuning the physical (e.g. concentration, solubility, temperature, pressure) and chemical (e.g. solvent and co-solvent) crystallization conditions. Heterogeneous crystallization might represent a valuable alternative for the control over the polymorphism of APIs. Langmuir monolayers have been shown to act as templates for the crystallization of inorganic molecules at the air-water interface; Mann demonstrated that Langmuir monolayers of stearic acid act as *supramolecular seeds* for the crystallization of the vaterite polymorphic form of calcium carbonate^[2]. Recently, we demonstrated that Langmuir monolayers of an amphiphilic calix[4]arene act as templates for the crystallization of acetaminophen, an API used for the relief of minor aches and pains^[3]. Although the macrocycles, self-assembled as a Langmuir monolayer at the air-water interface, initiate the crystallization of acetaminophen, no control over the polymorphism of acetaminophen was achieved. In this work, the interactions of an amphiphilic calix[4]arene (**1**), self-assembled as a Langmuir monolayer at the air-water interface, with gabapentin (GBP), an API used to relief neuropathic pain, and the ability of the macrocycle to kick off the interfacial crystallization of the pharmaceutical were investigated (Fig. 1).

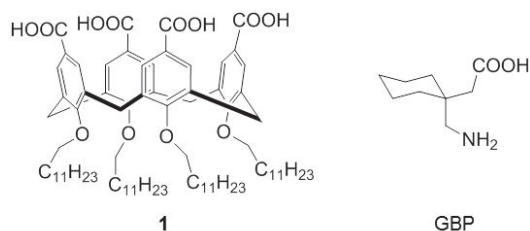


Fig. 1: Chemical structures of **1** and GBP.

1 was synthesized, in the cone conformation, as previously described^[3]. The self-assembly properties of **1** on pure water and on aqueous GBP subphases were investigated by surface-pressure area compression isotherms and surface ellipsometry, cf. Fig. 2. The isotherm of **1** on pure water indicates that the amphiphiles form a stable monomolecular film at the air-water interface. Interestingly, the iso-

therm of **1** shows a phase transition at 37.5 mN m⁻¹, suggesting that a molecular rearrangement of the macrocycle occurs.

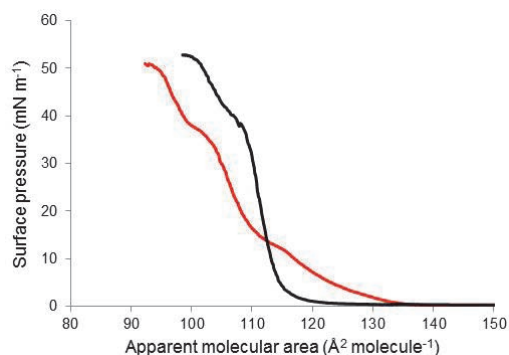


Fig. 2: Surface pressure-area isotherms of the monolayer of **1** on pure water (—) and on a 10⁻⁵ M aqueous GBP subphase (—).

Ellipsometry measurements indicate that, after the takeoff of the isotherm of **1**, the monolayer has an average thickness value of 2.6 nm above the phase transition measured at 37.5 mN m⁻¹. This value is in agreement with the molecular structure of the macrocycle densely packed as a Langmuir monolayer at the air-water interface. In the presence of a 5 g L⁻¹ aqueous GBP subphase, the profile of the isotherm of **1** considerably changes, thus demonstrating that the amphiphiles interact with GBP at the air-water interface. In addition, the thickness of the monolayer of **1** on a 5 g L⁻¹ aqueous GBP subphase increases up to 3.0 nm above the phase transition measured at 36 mN m⁻¹. The increase in the thickness of the monolayer of **1** on the GBP subphase may be explained by the favorable interfacial interactions of the amphiphiles with the API.

The 2D structure of the monolayer of **1** on pure water and on an aqueous GBP subphase was investigated by synchrotron-based grazing incidence X-ray diffraction (GIXD). The monolayer of **1**, compressed at a surface pressure value of 25 mN m⁻¹, is mostly amorphous. Upon further compression that is $\pi = 45$ mN m⁻¹ the monolayer of **1** possesses highly crystalline domains that coexist with the amorphous phase. These results indicate that the structure of the monolayer of **1** on water is dependent on the compression state of the film. In the presence of a 5 g L⁻¹ aqueous GBP subphase, no relevant changes in the molecular arrangement of the amphiphiles are observed, thus suggesting that the interfacial interaction of the monolayer of **1** with GBP does not affect the order of the aliphatic chains.

The ability of the monolayer of **1** to initiate the crystallization of the API was investigated by spreading on the surface of a supersaturated aqueous GBP solution (150 g L^{-1}) the monolayer of **1** compressed at surface pressure values of 0, 1, 25 and 45 mN m^{-1} . GBP crystals grew beneath the monolayers of **1** strictly at the air-water interface after 14 days while no crystallization occurred in the control experiments up to one month. These results demonstrate that the monolayers of **1** act as seed for the crystallization of GBP. Interestingly, single crystal X-ray diffraction analysis of the GBP crystals grown beneath the monolayers of **1** revealed that, while the crystals formed beneath the monolayers compressed at 0, 1, and 25 mN m^{-1} were the polymorph γ , those produced beneath the monolayers compressed at 45 mN m^{-1} were the polymorph α . Both polymorphs grew in a bilayer fashion with the plane of the bilayers parallel to the interface. In addition, the polar groups of GBP those act as molecular recognition units for the interaction with **1** point towards the interface, cf. Fig. 3.

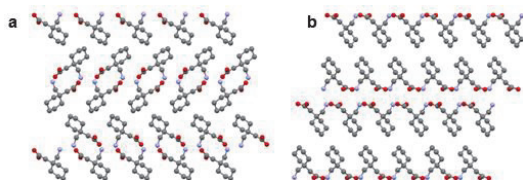


Fig. 3: Side-view packing arrangement of the polymorphs α (a) and β (b).

Interestingly, the hydrate polymorph of GBP crystallized in the controls, both at the interface and in the bulk solution. This represents the first example of the control over the polymorphism of an organic molecule by modulating the compression state of the appropriate Langmuir monolayer. We believe that the different molecular arrangements of the amphiphiles within the monolayer of **1** below and above the phase transition measured at $\pi = 38 \text{ mN m}^{-1}$ are responsible for the crystallization of two distinct polymorphs of GBP^[4].

Separation of chiral compounds is of great interest as the majority of bioorganic molecules are chiral. Amino acids play an important role in drug discovery and development as chiral blocks during synthesis of APIs. In the attempt to investigate the ability of chiral Langmuir monolayers to induce the enantioselective crystallization of amino acids, two amphiphilic enantiomeric calixresorcin[4]arene with four proline moieties were synthesized (L and D-RA-Pro). The two amphiphiles were demonstrated to form stable monomolecular films at the air-water interface. Langmuir monolayers of L and D-RA-Pro, compressed to a surface pressure value of 30 mN m^{-1} , were spread on the surface of a supersaturated aqueous L-alanine solution (175 g L^{-1}). L-alanine crystals grew strictly at the air-water interface beneath the D-RA-Pro monolayer after 18 hours and, beneath the L-RA-Pro monolayer and in the control experiments, after 24 hours. These results indicate that the D-RA-Pro monolayer increases the growth kinetics of L-alanine with respect to the L-RA-Pro monolayer. Despite that, L and D-RA-

Pro monolayers did not induce the enantioselective crystallization of DL-alanine that is racemic crystals were produced beneath both the monolayers.

The molecular arrangement of amphiphilic molecules within Langmuir monolayers plays an important role in the outcome of crystallization processes at the air-water interface. The presence of metal ions in the subphase may affect the nature of the molecular packing of surfactants at the air-water interface. For this reason, the interactions of the Langmuir monolayer of **1** with aqueous CuCl_2 , CoCl_2 , NiCl_2 and MnCl_2 subphases at the air-water interface were investigated. The self-assembly properties of **1** on the metals subphases, at concentrations of 10^{-5} and 10^{-3} M , were studied by means of compression isotherms and Brewster angle microscopy. The results indicate that the interfacial self-assembly properties of the monolayer of **1** are strongly affected by Cu^{2+} . Synchrotron radiation-based GIXD and X-ray near-total-reflection fluorescence (XNTRF) were performed to investigate the interactions of Cu^{2+} and Co^{2+} ions with the monolayer of **1** at the air-water interface. In the presence of a 10^{-3} M aqueous CuCl_2 subphase, GIXD measurements show high diffraction intensities, suggesting that the monolayer of **1** interacts with Cu^{2+} ions in the form of clusters. XNTRF analyses demonstrate that, in the presence of the monolayer of **1**, the emission lines for Cu^{2+} are stronger than those for Co^{2+} ions, thus indicating that the film strongly binds Cu^{2+} at the air-water interface^[5]. The possibility to enhance the crystallinity of Langmuir monolayers by using metal ions in the subphase may be exploited for the production of metal-organic-framework nanosheets. The nanosheets could be further transferred onto solid substrates by the Langmuir-Blodgett (LB) technique. Indeed, we recently demonstrated that Cu^{2+} ions act as inorganic *supramolecular clip* for the stabilization of calixarene-based LB films (Project 1308, p. 42).

References for Project A7.6:

- [1] H. G. Brittain, "Polymorphism in Pharmaceutical Solids", Informa Healthcare (2009)
- [2] S. Mann, B. R. Heywood, S. Rajam and D. Birchall, "Controlled crystallization of CaCO_3 under stearic acid monolayers", *Nature* **334**, 692 (1988)
- [3] N. Moridi, O. Danylyuk, K. Suwinska and P. Shahgaldian, "Monolayers of an amphiphilic para-carboxy-calix[4]arene act as templates for the crystallization of acetaminophen", *J. Colloid Interface Sci.* **377**, 450 (2012)
- [4] L. G. Tulli, N. Moridi, W. Wang, K. Helttunen, M. Neuberger, D. Vaknin, W. Meier and P. Shahgaldian, "Polymorphism control of an active pharmaceutical ingredient beneath calixarene-based Langmuir monolayers", *Chem. Commun.* **50**, 3938 (2014)
- [5] L. G. Tulli, W. Wang, W. R. Lindemann, I. Kuzmenko, W. Meier, D. Vaknin and P. Shahgaldian, "Interfacial Binding of Divalent Cations to Calixarene-Based Langmuir Monolayers", in preparation

Real-time viscosity and mass density sensors

Project A7.7 NoViDeMo (C-CINA, FHNW, University Hospital Basel, Endress+Hauser Flowtec AG Reinach)

Project Leader: T. Braun

Collaborators: J. Köser, O. Glaied, J. Hench, M. Touzin, M. Anklin, C. Huber

Introduction

Viscosity and mass density are key fluid properties. Thus, their accurate determination is fundamental to monitor industrial processes as well as medically relevant transitions, e.g. blood coagulation [1,2].

The project NoViDeMo (**n**ovel **v**iscosity and **d**ensity **m**onitoring) addresses two major limitations of common methods to characterize fluids: Sample consumption (milliliters) and throughput (minutes). Resonant nanomechanical cantilevers promise to overcome these limitations. Whereas sample consumption was already significantly reduced [3], the time resolution, limiting the throughput, was recently addressed.

Sensor implementation

The microcantilevers are embedded in a 1 μL silicone (PDMS) fluid channel. To drive and detect cantilever vibration, an optical setup consisting of two lasers of different wavelengths was built and optimized [4] (Fig. 1). The dynamic behavior of the cantilevers immersed in liquid and confined by microfluidic channels, i.e. with additional squeeze-film damping, was measured for several higher modes of vibration [5]. These findings were incorporated in the fluid cell design.

Hydrodynamic models were then employed to convert the resonance frequencies and damping of the cantilever into viscosity and mass density of the surrounding fluid [3].

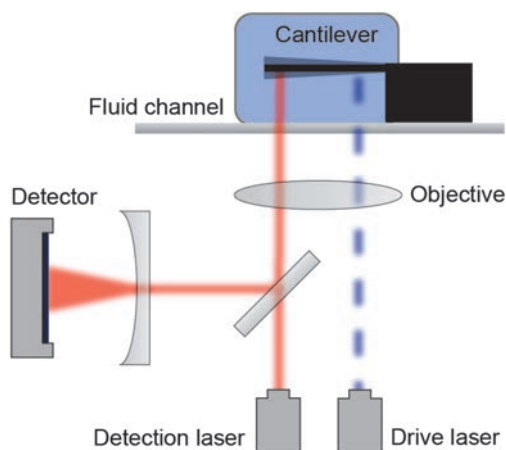


Fig. 1: Experimental setup: Photothermal excitation (blue modulated laser) to drive and an optical beam deflection system (red laser) to detect microcantilever vibration. The fluid surrounding the cantilever can be exchanged.

High-throughput viscosity/density screening

To date, methods to measure the viscosity and density of fluids with microcantilevers rely on the acquisition of resonance spectra; this usually requires several seconds [1]. To overcome this time-limiting step, we are investigating methods to detect changes in resonance frequency and damping with a resolution on the order of milliseconds [6]. This allows screening microliter sample droplets at a rate approaching 1 sample per second. Beside the advantage of a higher throughput, such method might prove less prone to unspecific adsorption; a major source of error in nanomechanical fluid property sensing. Fig. 2 shows a measurement of different aqueous samples (white areas) separated by fluorinated oil. Fig. 2 shows a measurement of different aqueous samples (white areas) separated by fluorinated oil.

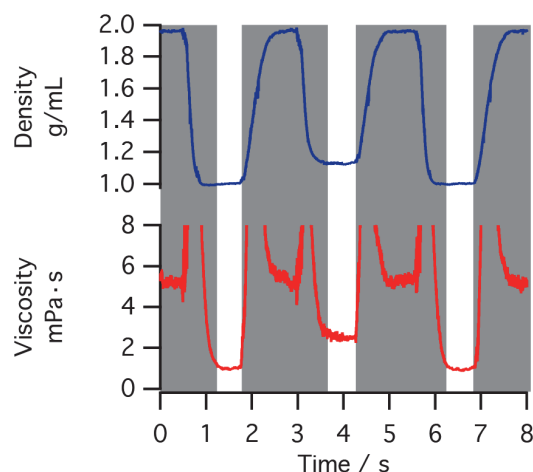


Fig. 2: High-throughput screening of aqueous sample droplets (white areas) separated by oil (gray areas). Note the transition instabilities between the oil- and sample droplets (few 100 ms).

Polymers for glucose sensing

The ability of the instrument to resolve rheological properties of polymers, by measuring multiple modes of vibration, was shown earlier [3].

Next, polymers were functionalized with specific groups that cross-link upon addition of glucose. The resulting shift in viscosity can be detected and related to the surrounding glucose levels. Such principle might overcome limitations encountered with electrochemical sensors, specifically meeting the prerequisite of a longer sensor lifetime required for continuous glucose monitoring [7] (Fig. 3).

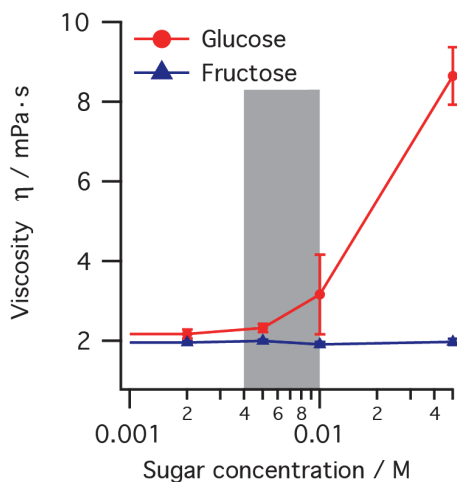


Fig. 3: Glucose sensing polymer. Addition of glucose resulted in an increase in viscosity of the polymer solution; the gray area indicates physiological blood glucose levels. The addition of fructose did not alter the viscosity.

Protein folding and aggregation

The viscosity of biological solutions is strongly coupled to the condition of the solutes. Changes in folding state [1] or aggregation [2] of proteins can be detected by continuously monitoring the viscosity. Lysozyme, a small, soluble protein, was chemically unfolded using urea and changes in viscosity were measured. The viscosity shift is due to the transformation from a compact globular into a flexible random conformation. Fig. 4 shows that the relative viscosity decreases with increasing urea concentration, i.e., unfolding. This somewhat surprising behavior might be related to the rheological, i.e., frequency dependent, properties of the solution; the data was obtained at a frequency of ~200 kHz.

Conclusions

In the first phase, the project NoViDeMo addressed the optimization of nanomechanical resonators for sensing applications in liquid, namely the development of a photothermal excitation setup [4] and characterization of squeeze-film damping [5]. These results are also applicable to atomic force microscopy. Next, a fluid property sensor was developed, evaluated and optimized [3,6]. Finally, proof-of-concept measurements to characterize proteins [1] and glucose-sensing polymers [7] were conducted.

Involved scientists

Benjamin A. Bircher (PhD student), Roger Krenger, Luc Dümpelmann (master students supervised by Benjamin Bircher).

Acknowledgments

We acknowledge Henning Stahlberg, Shirley Müller, Andrej Bieri, Stefan Arnold, Jonas Pollard, Nico

Bruns, Thomas Pfohl, Hans Peter Lang, François Huber, Christoph Gerber, Thilo Glatzel, and Ernst Meyer for their help and collaboration.

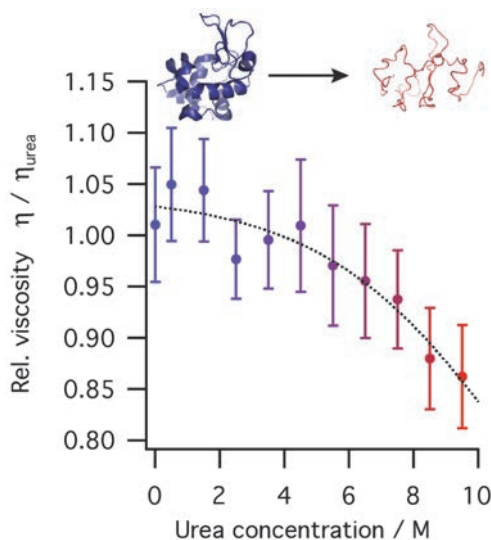


Fig. 4: Unfolding of egg-white lysozyme with urea. The dashed line is a guide to the eye.

References for Project A7.7:

- [1] B.A. Bircher, *Fluid characterization by resonant nanomechanical sensing*, PhD thesis, University of Basel (2014)
- [2] O. Cakmak, et al., *A cartridge based sensor array platform for multiple coagulation measurements from plasma*, Lab Chip. 15 (2014) 113–120
- [3] B.A. Bircher, L. Duempelmann, K. Renggli, H.P. Lang, C. Gerber, N. Bruns, et al., *Real-time viscosity and mass density sensors requiring microliter sample volume based on nanomechanical resonators*, Anal. Chem. 85 (2013) 8676–8683
- [4] B.A. Bircher, L. Duempelmann, H.P. Lang, C. Gerber, T. Braun, *Photothermal excitation of microcantilevers in liquid: effect of the excitation laser position on temperature and vibrational amplitude*, Micro Nano Lett. 8 (2013) 770–774
- [5] B.A. Bircher, R. Krenger, T. Braun, *Influence of squeeze-film damping on higher-mode microcantilever vibrations in liquid*, EPJ Tech. Instrum. 1 (2014) 10
- [6] B.A. Bircher, R. Krenger, T. Braun, *Automated high-throughput viscometer using resonant nanomechanical sensors*, in preparation
- [7] R. Krenger, *Nanomechanical resonators for fluid characterization: Applications and limitations*, Master's thesis, University of Basel (2014)

Bio-DURABLE self-cleaning paint: development of dirt repellency coatings for large surfaces

Project A8.1 Bio-DURACLEAN (FHNW, Walter Mäder AG)

Project Leader: O. Glaied

Collaborators: U. Pieles, W. Meier, J. Reiter

Creating a stable and robust synthetic surface that repels dirt and various liquids has broad technological implications for areas ranging from nanotechnologies and surfaces to polymers. However, the development of these surfaces has proved to be extremely challenging.

Bio-DURACLEAN is a project aiming to develop a durable dirt-repellent large surface. The project innovation is based on the combination of three ideas: A new approach to mimic the lotus effect (Fig. 1) with a surface roughness given by the nano-/microparticles, water-repellent polymer that gives a dirt repellency effect and, for the first time, the use of cellulose nanoparticles.

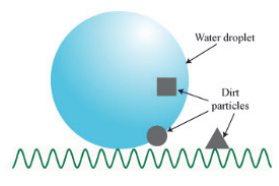


Fig. 1: Self-cleaning effect on the surface of a leaf.

To address these challenges, we here present the study to create a self-cleaning painted surface. The surface has a special, characteristic roughness: Systematically arranged painted surface, nano- and microparticles, and water-repellent polymer covering the whole surface. For the nano particles, two kinds of nanoparticles were studied. The first are silica nanoparticles and the second are cellulose nanoparticles. Combined with the micro- and nanoparticles, the water-repellent surface makes the painted surface super-hydrophobic, i.e. non-wettable, giving it the self-cleaning properties.

To reach a high durability, the Mäder technology is used to well disperse the formulation and to covalently link the nanoparticles, the microparticles, the hydrophobic macromonomer and the painting layer to the polymer matrix.

I. Development of the lotus-like organization

The plant's ability to repel water and dirt results from a combination of a superhydrophobic surface of micron-scale hills, valleys and nanometer-scale waxy bumps that create rough surfaces don't giving water or dirt the chance to adhere. To address several unique applications, we attempted here to duplicate the lotus surface using a variety of materials, including paint, a combination of nano- and microsilia, and nanocellulose crystals.

Based on these project objectives, Bio-Duraclean is divided on two studies which are conducted in parallel; the first concerns the development of a dirt-repellent surface with the combination of the nano- and the microparticles of silica, and the second a bio-approach by using the cellulose nanoparticles with the silica microparticles on the surface.

I.1. First approach: Paint formulations based on lotus-like organization obtained with silica nano- and microparticles.

The first part of the paint surface development based on lotus-like organization obtained with the combination of nano- and microparticles of silica concerns the synthesis of silica particles with different sizes and the study of their organization on the paint surface.

To prepare monodisperse and uniform-size nanoparticles, silica particles were synthesized following the Stöber method using sol-gel process. For the nanometric particles, various-sized particles in the range 20-460 nm were synthesized. For the micrometric silica size, a one-pot method has been studied to prepare monodisperse silica particles in which TEOS was continuously supplied to an ethanolic solution of water and ammonia in the presence of electrolytes. Various-sized particles in the range 1.8-3.6 μm were synthesized.

The silica particles have a negative zeta potential due to Si-OH on the particle surface, which causes a hydrophilic effect. In order to organize the silica nanoparticles around the micro ones, the idea was to graft a cationic charge onto the silica microparticles' surfaces and to adsorb the silica nanoparticles on the surface of the micro ones based on an electrostatic link. The studied reaction is presented in Fig. 2.

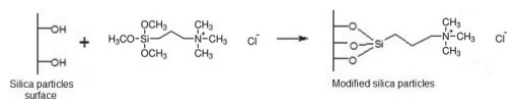


Fig. 2: Silica microparticle cationization.

The comparison between the unmodified silica zeta potential (-41.8 mV) and the modified one shows the cationization of the silica surface (+62.6 mV).

The modified cationic microparticles were incorporated in a coating formulation. A flat surface of the paint formulation was obtained with a spin coating method and UV cross linking under inert atmosphere. The coating layer was analyzed with contact angle and SEM microscopy (Fig. 3).

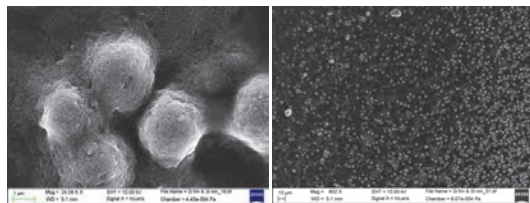


Fig. 3: SEM pictures of the coated surface. Encapsulation of the silica cationic microparticles (25 % w) with the silica nanoparticles (75 % w).

Despite the hydrophilic character of the Luminux (static contact angle, SCA=85°), a clear increase of the surface hydrophobicity was reached (SCA=102°).

I.2. Bio-approach: Coating formulations based on lotus-like organization obtained with cellulose nanofibers and silica microparticles

The second part of the project is dedicated to the study of nanocellulose fibers' effect in the paint formulation in order to obtain the lotus-like organization.

Nanocellulose fibers with widths in the nanometer range are nature-based materials with unique and potentially useful features^[1]. These novel nanocelluloses open up the strongly expanding fields of sustainable materials and nanocomposites.

Details of nanocellulose crystal generation are not enough clear. Its mechanism is usually explained by selective acid hydrolysis of amorphous domains of cellulose fibers. The study of the nanocellulose synthesis based on a conventional process does not result in cellulose nanocrystals. The partial efficacy of the acid hydrolysis was already noted in the literature. In order to improve the NCC synthesis, the reaction was realized in the microwave and all the parameters were optimized (acid concentration, temperature, duration,) which results in nanocellulose crystals with a yield of 30 %. Under controlled conditions of acid hydrolysis treatment and exposure to microwave radiation, rod-shaped cellulose from 70-200 nm in length was obtained, leading to the formation of high-purity single crystals (Fig. 4).

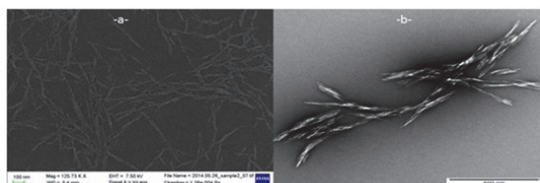


Fig. 4: -a- SEM pictures/-b- TEM pictures of nanocellulose crystals

The lotus-like organization of the particles on a surface was studied through optimization of different parameters in order to determine the size of the micro, the ratio between these two particles sizes and the concentration of the mineral material on the coating formulation. The nanocellulose crystals

were used to encapsulate the cationic silica microparticles as detailed in Fig. 5. The obtained organization is followed by UV cross linking of the paint on the surface.

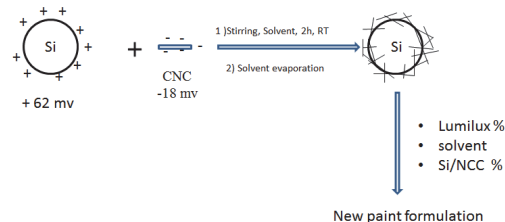


Fig. 5: Development of the self-cleaning surface based on the lotus surface organization

The study of the wetting behavior shows significant increase in the contact angle of the new formulation paint layer compared with unmodified lumilux surface. The SEM pictures (Fig. 6) show the roughness of the surface. The silica microparticles were completely surrounded by nanofibers and the paint is covering the whole system. Lotus-like organization was not as perfect as in nature, however, the static contact angle (SCA) measurement of the new paint (115°) shows an increase compared to unmodified surface paint (85°). The new formulation resulted with 35 % increase of SCA and therefore an improvement of the surface hydrophobicity.

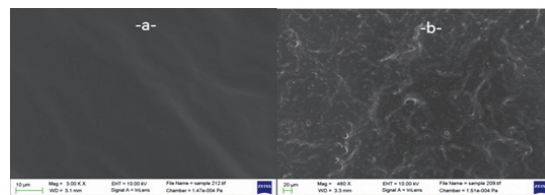


Fig. 6: SEM pictures: -a- unmodified paint surface, -b- paint formulation based on paint, silica microparticles and nanocellulose fibers.

II. Conclusion

Two approaches were studied for the development of lotus-like organization surface. The first is based on silica nanoparticles surrounding silica microparticles and covered with hydrophobic paint layer, the second with replacing the silica nanoparticles with nanocellulose crystals. A better increase in the surface hydrophobicity (35 %) was observed for the formulation based on the nanocellulose crystals. For reasons of confidentiality, no details about the formulations are given.

References for Project A8.1:

- [1] Y. Shimazaki, Y. Miyazaki, Y. Takezawa, M. Nogi, K. Abe, S. Ifuku, H. Yano, "Excellent Thermal Conductivity of Transparent Cellulose Nanofiber/Epoxy Resin Nanocomposites", *Biomacromolecules* **8**, 2976 (2007)

Synthesis and mobility properties of new nanoparticles for colored e-readers

Project A8.3 EL-ENA (FHNW, CSEM SA Muttenz, BASF Schweiz AG Basel)

Project Leader: U. Pieleš

Collaborators: Ch. Jablonski, S. Stebler, G. Grundler, U. Pieleš^a, R. Öhrlein^b and Z. Szamel^c

a) FHNW- ICB, Muttenz

b) BASF Research Center Basel

c) CSEM, Muttenz

ABSTRACT

A new approach based on non-pigmented, stable colored nanoparticles able upon the application of a current to migrate in the electrical field has been developed for the improvement of the color brightness of e-displays.

The scientific challenges comprise first efficient syntheses of tri- and difunctional dendrimers including branching points for further extension, the covalent attachment of these scaffolds to silica nanoparticles via hydrosilylation and final decoration with the dyes (Fig. 1 yellow, magenta, cyan).

INTRODUCTION

New display technologies such as e-paper and e-ink have recently gained significance. However, mostly grey-scale electrophoretic displays are available on the market (Amazon Kindle or SONY PRS for example), and the few color displays available on the market lack in picture brightness.

The project aims at the synthesis and characterization of new nanoparticles attached to a dendrimer of first and second generation and decorated with a dye (yellow, magenta, cyan). It was established that commercially available silica particles are preferable to gain enhanced brightness of the colors. Three-branched and two-branched functionalized dendrimers were prepared and evaluated.



Fig. 1: Three dyes (magenta, yellow, cyan) selected for the development of the new electrophoretic nanoparticles.

Dendrimer structures were designed individually, depending on the functionality present on the dye. In a last stage, in-situ charging enables the move-

ment of the nanomaterial in an electrical field which was screened in a small customized device at CSEM.

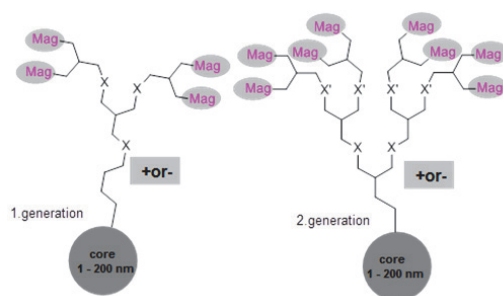


Fig. 2: Final assembly charged comprising the dye, dendrimer and silica nanoparticles.

RESULTS

Dendrimers: due to the steric hindrance (neopentyl effect), three-branched dendrimers **1** and **2** (R=Me) have showed limited reactivity. Two-branched dendrimer **2** (R=H) was attached to the yellow dye, the longer chain spacer dendrimer **3a** was used for the magenta dye and dendrimer **3b** was investigated for the linkage to the cyan.

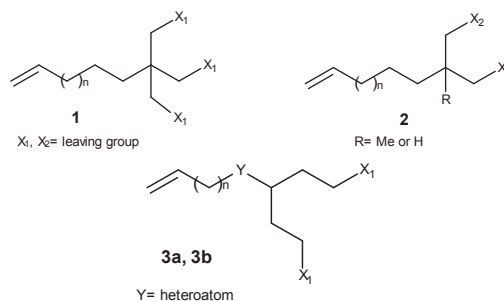


Fig. 3: structures of the three- and two-branched dendrimers developed for the attachment to the dyes.

Yellow dye nanomaterials: dendrimer **2** (R=H) reacted readily with a short spacer which formed a sulfonamide with the yellow dye in moderate yield. Subsequent catalytic hydrosilylation led to non-charged nanoparticles.

Suitable reaction conditions for the activation of the chloride of the yellow dye could not yet be established for the final functionalization of the structure (introduction of a hydrophobic chain and in-situ charging).

Magenta dye nanomaterials: dendrimer **3a** after extension with a short protected spacer was attached to the silica nanoparticles quantitatively. After deprotection of the spacer, the magenta dye was coupled to the particle-dendrimer assembly.

Final functionalization to increase the solubility and in-situ charging was achieved and validated on small scale. In the six-step sequence developed from **3a**, only one purification step by chromatography was necessary. The final construct was analyzed by ^1H and ^{13}C NMR.

The functionalized blue dye was synthesized in five steps which were optimized for good to high yields; the purifications by chromatography were reduced to two steps. However, this material remained completely unreactive as a nucleophile. Modifications of the initial plan of synthesis were required.

Tests for the mobility of the model charged nanoparticles at CSEM. Simplified structures (no dendrimer scaffold included) were tested in the case of the yellow and magenta particles applying a voltage of 10-60 V of different polarization. The expected results were obtained as shown below: we can see the accumulation of particles to the electrodes with a +/-30 V voltage, faster movement was observed when applying a higher voltage.

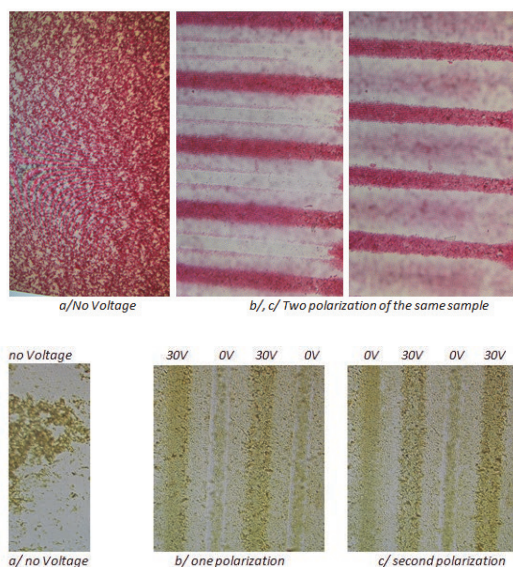


Fig. 4: Mobility tests performed with the model nanoparticles (magenta and yellow) when an adjustable current is applied (+/-30 V).

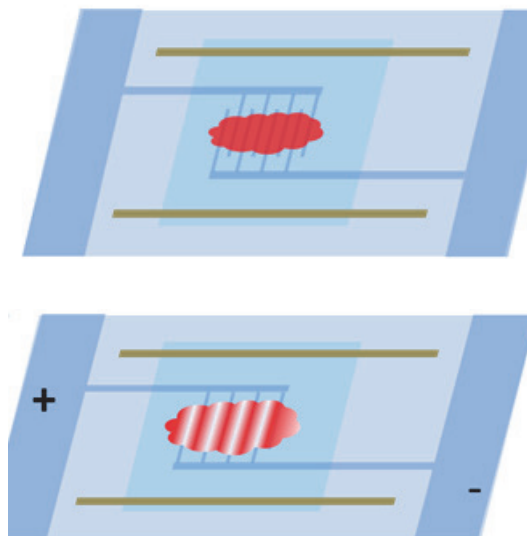


Fig. 5: Device elaborated at CSEM for the test of mobility of charged nanoparticles: ITO electrode thickness 150 μm ; foil thickness used for magenta particles: 38 μm ; foil thickness used for yellow particles: 30 μm .

CONCLUSION AND FURTHER STEPS

Silica nanoparticles covalently linked to a UV-stable yellow dye via a two-branched dendrimer were prepared in nine steps with a good overall yield and limited efforts for purification. However, the introduction of a second linker on the construct enabling particles' mobility by electrophoresis is not yet established.

The attachment of the magenta dye to nanoparticles linked to a two-branched dendrimer could be optimized and led to a fully functionalized and charged assembly suitable for on-going mobility tests performed by CSEM. The mobility of the charged particles was proved.

In addition, the two-branched dendrimer **3b** was prepared for linkage to the cyan dye. The coupling to the blue dye was investigated and remained so far unsuccessful. A modified linker displaying a more electrophilic moiety (Michael acceptor) was synthesized and did not afford a coupling. New strategies are now investigated for the linkage of the blue dye to the dendrimer based on aromatic nucleophilic substitution.

References for Project A8.3:

- [1] R. Öhrlein et al. *Chimia* 63(6), 351 (2009)
- [2] N. Sabourault et al. *Organic Lett.* 4(13), 2117 (2002)
- [3] A. Marra et al. *Eur. J. Org. Chem.* 1144, (2013)

Silver-based catalyst development

Project A8.7 NANOX (FHNW, University of Basel, SKAN AG Allschwil)

Project Leader: U. Pielers

Collaborators: O. Scheuber, C. Redard-Jacot, J.-B. Sauvet

Introduction

This project consists in the development of a catalytic filter for the effective conversion of methanol in formaldehyde. The first part of this study describes the identification of main specifications. Thus, this work takes into account different aspects such as the technologies involved in the production and the economical point of view. Furthermore, the optimization process and scale-up are not part of this work. The final step is the obtaining of the proof of concept and the study of technical feasibility.

The main specifications are the use of a transition metal as catalytic agent and its deposition on an inorganic support showing important specific surface. Concerning the deposition method, the requirements are a good reproducibility and a liquid-phase process. Since silver's catalytic properties make it ideal for use as a catalyst in many reactions such as oxidation reactions, we therefore propose a reproducible procedure for the deposition of silver on highly porous ceramic in solution. Moreover, in anticipation of a future industrial implementation, the synthetic procedure should allow an easy scale-up and the use of accessible raw materials.

Choice of the support

The production of a porous ceramic catalytic filter can be made in two different ways. The two possibilities are either the silver coating of a foam (Fig. 1, left) or the packing of coated beads in a frame (Fig. 1, right).

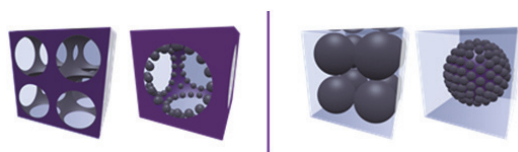


Fig. 1: Ceramic foam filter (left, general and detailed view) and packed ceramic beads (right, general and detailed view) with silver coating (in grey)

In this study, the use of ceramic beads was preferred. The advantages are the possibility to change the shape of the filter frame and an easier coating method in solution.

Choice of the deposition method

Electroless silver deposition is a liquid phase process where silver ions are reduced to form a metal layer on a surface. The most popular method for silver deposition is known as the Tollens reaction and consists in a redox reaction between a silver complex and an aldehyde in alkaline conditions.

The reaction pathway can be described as follows:



where $[\text{Ag}(\text{NH}_3)_2]^+$ is the silver diamine complex obtained by reaction between AgNO_3 and NH_3 .

During the reaction, the aldehyde RCHO is oxidized to its corresponding carboxylic acid. In this work, glucose was used as it is a commonly employed aldehyde in Tollens reaction.

Procedure

Before the coating process, ceramic beads were impregnated with H_2O . The substrate was then immersed in the freshly prepared Tollens reagent solution and placed in a rotating tumbler (Fig. 2) to ensure homogeneous coating.

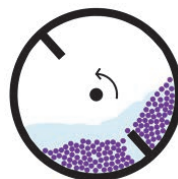


Fig. 2: Scheme of the rotating tumbler used for beads silver coating

Three parameters were considered to determine the most efficient conditions: the pH of the solution, the concentration in Tollens reagent, i.e. $[\text{Ag}(\text{NH}_3)_2]^+$, and the volume of solution per gram of ceramic material giving a 2^3 factorial design so eight test conditions (Table 1).

Test	pH	$[\text{Ag}(\text{NH}_3)_2]^+$	Ratio
A	9	100 mM	1.5 ml g ⁻¹
B	9	100 mM	3.0 ml g ⁻¹
C	9	50 mM	1.5 ml g ⁻¹
D	9	50 mM	3.0 ml g ⁻¹
E	8	100 mM	1.5 ml g ⁻¹
F	8	100 mM	3.0 ml g ⁻¹
G	8	50 mM	1.5 ml g ⁻¹
H	8	50 mM	3.0 ml g ⁻¹

Table 1: 2^3 factorial design conditions

Four responses were finally considered: the surface colors, the SEM topography, the silver surface distribution and the conversion capacity of the coated material. The reaction was continued for a total of about two hours. The resulting material was then washed three times using H_2O and finally dried at 80 °C.

Morphological characterizations were performed by scanning electron microscopy (SEM) for topography determination and EDX elemental mapping (Supra 40 VP and EVO 40, Carl Zeiss AG, Germany). Methanol conversion in liquid phase was measured by UV-Visible spectroscopy (Cary 4000 UV-Vis, Agilent, US).

Results

During the reaction, the initially white beads slowly turn black while silver deposition occurs at the surface. Color changes in the factorial design are easily visible on Fig. 3, showing almost no coating for beads treated in condition 50 mM / ratio 1.5 independently of the pH (Material C and G). For all the other conditions, slight differences are perceptible but all resulting materials appear grey.

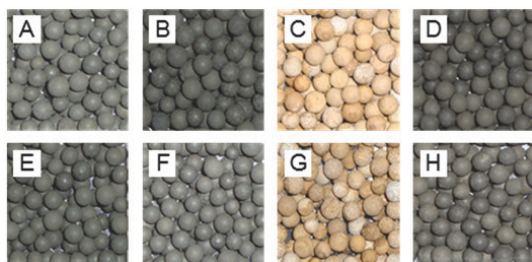


Fig. 3: Visual aspect of factorial design results

As it appears on SEM pictures, the beads' topography before (Fig. 4, left) and after silver coating (Fig. 4, right) remains unchanged. This proves the absence of silver clusters formation and confirms the deposition of a silver film. As a consequence, the high specific surface of the inorganic matrix is preserved.

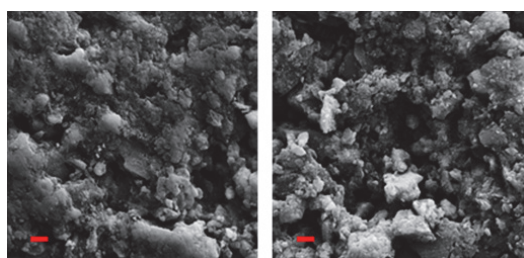


Fig. 4: SEM picture of ceramic beads surface. Non-coated (left) and coated material (right) (scale bar 1 μm)

The analysis of elemental mapping for silver (Fig. 5, left) reveals a good surface distribution. A statistical treatment of the obtained data confirmed this observation with the obtaining of a normal distribution of silver atoms at the surface of the coated material (Fig. 5, right).

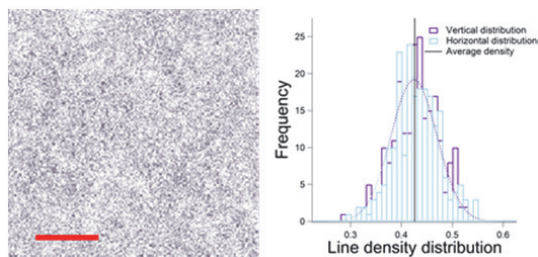


Fig. 5: Silver elemental mapping (scale bar 25 μm)

The study of the methanol conversion reveals the highest activity for the material H (Fig. 6, dark green), while the material B is the less efficient (Fig. 6, light green). As a consequence, the conditions used to obtain the material H will be used for the optimization of the catalytic material.

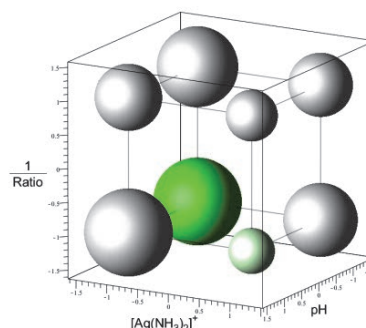


Fig. 6: Factorial design results for methanol conversion in liquid phase

Conclusion

A straightforward procedure is suggested for the obtaining of homogeneous silver deposition on a ceramic support. Herein, the choice of a liquid phase procedure appears as a good alternative and presents the advantage to be realized at room temperature and to avoid the release of harmful aerosols. Considering the easy procedure and the isotropic nature of electroless silver coating, we believe that this method can be used in a wide range of applications. Furthermore, the possibility to adapt the filter thickness to the needs should allow tunable oxidation reactions. Further experiments will enable to determine the efficiency of the catalyst and to select parameters allowing the scale-up.

References for Project A8.7:

- [1] S.-H. Zhang et al., "Synthesis of silver nanotubes by electroless deposition in porous anodic aluminum oxide templates", Chem. Commun., 1106 (2004)
- [2] A. Antonello et al., "Optimized Electroless Silver Coating for Optical and Plasmonic Applications", Plasmonics, 7 (2012)

Polymer emulsion-segmented electroconductive nanofibers for antistatic textile finishing

Project A9.2 em-SELECT (FHNW, PSI, HeiQ Materials AG Bad Zurzach)

Project Leader: U. Pielec

Collaborators: M. Bader, V. Vaché, A. Leisibach (FHNW), J. Gobrecht (PSI), M. Kristiansen (FHNW-INKA), M. Height, W. Bender (HeiQ Materials AG, Bad Zurzach AG)

With nanotechnology to new textiles

Introduction

Electrostatic discharges of work-wear's textile as in medical garments, for oilfield's workers or in the electronic industry, may cause hazards, fire incidents, severe damages to the electronic equipment and discomfort for the wearer. State of the art is the incorporation of metal fibers into the textile or use of graphite to obtain durable antistatic properties. These methods exhibit significant disadvantages by limiting the colours and the wear comfort. The target is the integration of wash resistant antistatic properties in the industrial standard finishing process, the last wet process of the textile production chain, which does not affect the other physical properties of the fabric (appearance, durability and hand-feel). The aim of the em-Select project is to produce conductive micro- and nanofibers using a new approach. The conductive fibers have to be applied by the standard padding process in the textile finishing bath, providing antistatic properties to the pro-

duced fabric. These conductive fibers have to be a minor component of the textile and therefore need to be extremely thin and small. The electrospinning technology, presented in Fig. 1, is the most suitable technique for producing such fibers.

Concept

The concept, presented in Fig. 2, is based on fibers made from two different polymers: a conductive polymer that is not soluble in water and a non-conductive polymer, soluble in water, referred to as an auxiliary polymer. For the electrospinning process, an emulsion of the conductive polymer in an organic solvent and the auxiliary polymer in water has to be done. The reason of this process is to generate a web of continuous polymeric nanofibers consisting of an alternating pattern of interconnected conductive and non-conductive segments. The auxiliary polymer segments will be dissolved in the aqueous finishing formulation, and the remaining conductive fibers of a nano-scale diameter will then form a conductive network on the treated textile.

Materials

Conductive polymers that were tested are polyaniline (PAni), principally doped with camphor-sulfonic acid (CSA), and poly(3,4-ethylenedioxythiophene) combined with Polystyrene sulfonate (PEDOT:PSS). Auxiliary non-conductive polymer such as poly(methyl-methacrylate) (PMMA) and polyethylene oxide (PEO), of different molecular masses, were mixed with the conductive ones to get the nanofibers' web. Solvents such as dimethylacetamide (DMAc) or chloroform were used to solubilise the polymers.

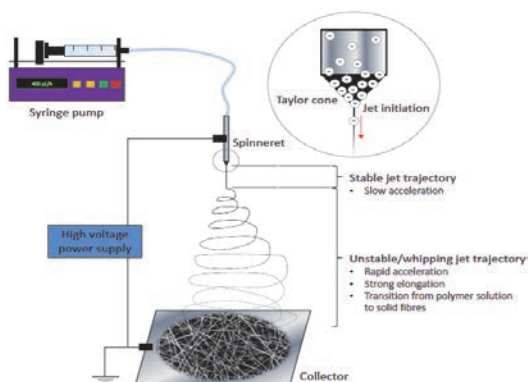


Fig. 1: Schematic representation of electrospinning setup.

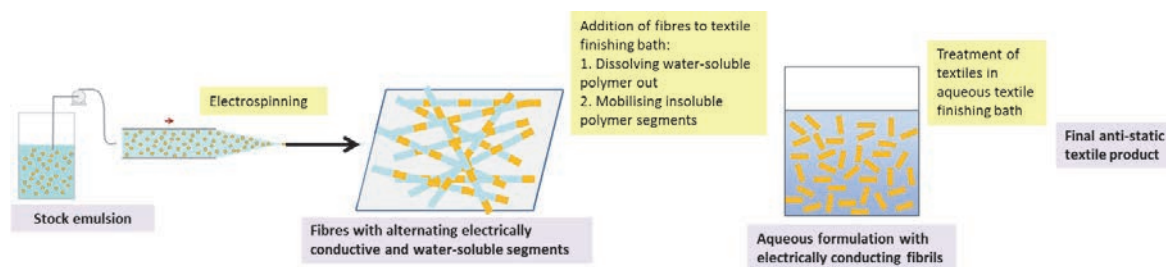


Fig. 2: Stock emulsion electrospinning approach.

Results

With the auxiliary polymer alone, fibers with an average diameter of 110 nm could be produced from the electrospinning process. Combinations of conductive and non-conductive polymers were tested. The spinning process of the combined conductive and auxiliary polymer in two phases is still under development.

The main hurdles of this project are the low solubility of the conductive polymers in organic solvents, preparation of stable dispersion and formation of bead-less fibers from the spinning process. Nevertheless, it was possible to produce fibers with conductive polymer enclosed in the auxiliary polymer: PANi doped with CSA combined with PMMA (see Image 1) and PEDOT:PSS combined with PEO.

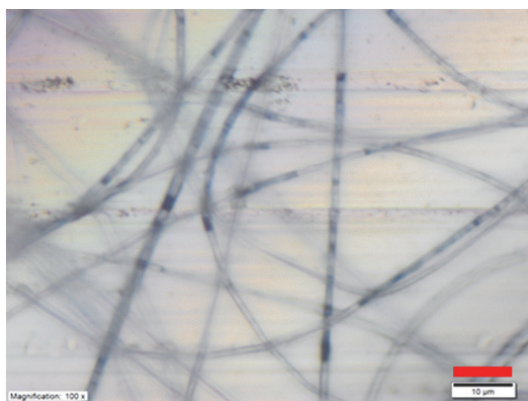


Image 1: LM image (reflection) of electrospun PANi/PMMA fibers on aluminium collector. Scale bar 10 µm.

Better results could be obtained by adding surfactants (SLS or Triton X-100)^[1], with variation of the molecular masses of the auxiliary polymers, optimization of the electrospinning parameters and combination of mixing process when dispersing the conductive polymer. Nets of nanofibers with a diameter range from 110 to 300 nm could be produced (see Image 2) from those improvements. This development process is currently not finalized, and improvements have to be continued.

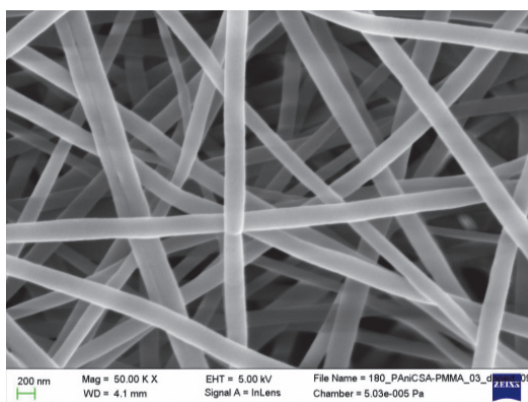


Image 2: Scanning electron microscopy image of nanofibers consisting of PANi doped with CSA in combination with PMMA as auxiliary polymer.

Outlook

It is possible to produce uniform and bead-less nanofibers of different combinations of electrically conducting polymer with an auxiliary polymer around. Some conductivity measurements were conducted. For some solutions, conductivity was measured on the fibers web produced but not on single fibers. The main focus is still concerning how to properly disperse the conductive polymer to make a single fiber conductive.

Other conductive polymer such as poly(3-hexylthiophene-2,5-diyl) (P3HT) doped in an iodine environment has to be further tested to see if it is possible to achieve conductive nanofibers.

To circumvent the elaborate generation of a stable stock emulsion, another approach using microfluidic chips^[2] is possible as shown in Fig. 3. In this method, an emulsion is generated directly before the electrospinning at the spinneret. Different microfluidic chip designs and flow rates are used to create micro-droplets of the conductive polymer solution inside the water-soluble polymer solution.

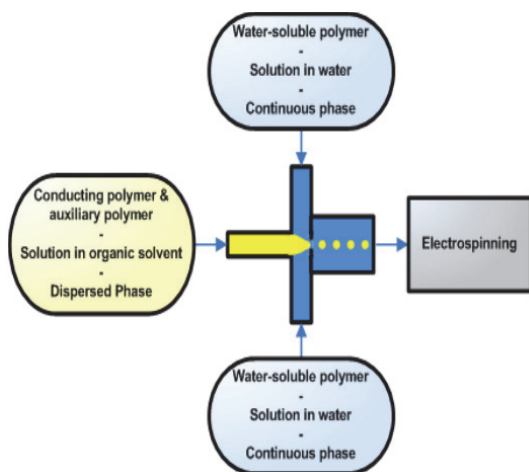


Fig. 3: Schematic representation of the electrospinning setup

The main focus is laid on improving electrospun fiber's electrical conductivity by optimising polymer-blend-solution's homogeneity and electrospinning process parameters. Due to confidentiality agreements, latest and more advanced results cannot be shown here.

References for Project A9.2:

- [1] B. Fan, Significant conductivity enhancement of conductive PEDOT:PSS films by adding anionic surfactants into polymer solution, *Macromolecules* 41 (2008) 5971-5973
- [2] M.T. Guo, D.A. Weitz, Droplet microfluidics for high-throughput biological assays, *Lab Chip*, 2012, 12, 2146-2155

Functionalized nanofiber-enhanced filter media for fine particles and heavy metal removal in flue gases

Project A9.6 NANOFIL (PSI, FHNW, Alstom AG Birr)

Project Leader: C. Ludwig

Collaborators: M. Tarik, M. Paraskevopoulos, F. Pilger, A. Testino, M. Waser, U. Pielers, D. Winkler, G. Timothy, I. Thanou, M. Bialkowski

Introduction

In order to improve the performance of the current fabric filter systems, e.g. more efficient fine particle removal and higher specificity for heavy metals, either in the ionic or in the elemental state, an entirely new approach was planned. The strategy was to develop materials with high specific surface area, thermal and mechanical stability, and functionalized with sulfur (S) groups, which have high specificity for heavy metals.

During the first year, the “NANOFIL” project was devoted to the development of new organic, inorganic, and composite nanofibers. The organic nanofibers are produced by electrospinning, the inorganic material is based on hydrothermally prepared cerium dioxide (CeO_2) nanorods, and the composites were produced by electrospinning a polymer solution containing CeO_2 spherical nanopowders. Based on the ongoing work, the produced nanofibers are currently under optimization. In the second year of the project, the synthesized fibers will be tested by using an in-house constructed setup, to evaluate their sorption properties, regenerability, and thermal stability.

Synthesis of nanofibers

For the selection of the base filter material, the flue gas temperature, continuous and peak, is the most important criterion for filter media selection. Fibers can survive short term exposure to temperatures above their continuous operating temperature limit, but the high heat will degrade them. Additionally, chemical attack, such as contacts with acids and alkalis, can have similar effect. For the manufacturing of the project's filter media, two materials have been selected: polyphenylene sulfide (PPS) and P84 (Polyimide). The latter has outstanding properties such as high temperature stability, good chemical resistance, high mechanical strength and minimal abrasion. Since the nanofibers will be applied in the same environment as the base material, P84 was also chosen as the material for the electrospinning. P84 was electrospun as a solution in DMF to produce nanofibers that can be tailored from diameters of approx. 60 nm up to 1 μm .

The innovative idea in this project is to develop nanofiber materials able to capture S, which then can then be used to remove specific heavy metals such as Hg from flue gases. One way to achieve

that was to modify the P84 material to bear thiol groups which can sorb mercury. Therefore, P84 was allowed to react with cysteamine. The thiol-modified P84 is also soluble in DMF a can be electrospun as P84, albeit with different conditions, since the polymer properties are changed (Fig. 1).

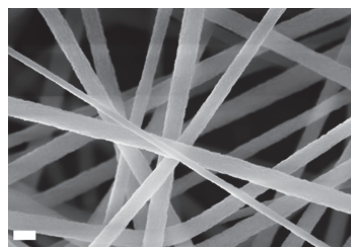


Fig. 1: Electrospun fibers of thiol-modified P84. Scale bar: 400 nm, magnification: 40000x.

Alternatively CeO_2 nanoparticles were synthesized and their capability to capture sulfur was investigated. The activated nanoparticles can be directly deposited on the base filters or electrospun as composite along with P84 (Fig. 2).

CeO_2 nanoparticles synthesis: Several batches of CeO_2 nanoparticles have been produced with the aim to control the particle morphology. Fig. 3 shows an example of the obtained particles with elongated morphology. These materials can be used in granulated form or integrated in a filtering support. The influence of the particle shape on the S and Hg capturing is currently under investigation. CeO_2 nanoparticles with a size of less than 5 nm were produced to be directly immobilized into an inorganic filter material (e.g. glass or quartz). After the synthesis, the particles were washed and dried. The processing promotes particle aggregation (> 1 μm); the aggregates are large enough to be retained by the filtering material. A thermal treatment was applied in order to fix the aggregates on the inorganic support. Some fully inorganic filter with CeO_2 nanoparticles have been produced and are currently under testing.

CeO_2 nanoparticles (< 3 nm) without any drying treatment were synthesized as well. In this case, the material is used for the preparation of the composite fibers by electrospinning. The particles were collected by chemically induced coagulation and re-dispersed in a solvent compatible with the electrospinning process.

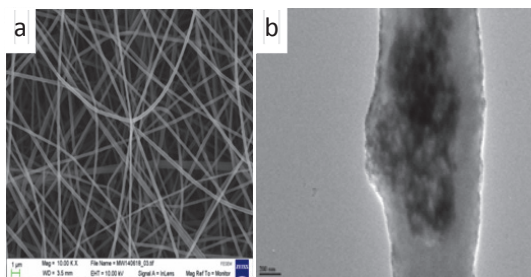


Fig. 2: Example of electrospun composite fibers: (a) SEM; (b) HR-TEM. A CeO_2 nanoparticle aggregate is clearly incorporated in the fiber.

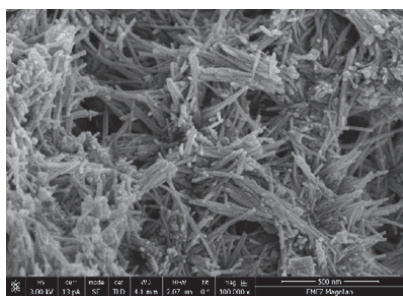


Fig. 3: Example of synthesized CeO_2 acicular particles with tailored size: (a) 500x20 nm.

Sulfur adsorption: Figure 4 reports the preliminary results on S capturing. The sorption was carried out using 1000 ppmV H_2S at 800 °C. The regeneration was done at same temperature with 4 % O_2 . The material shows excellent sorption capability and it is regenerable. The calculated S/Ce molar ratio is 31 %. The material after S sorption is ready to be tested for Hg capturing.

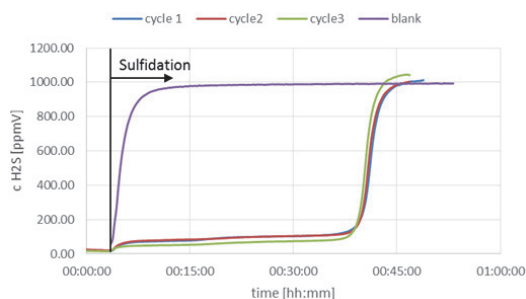


Fig. 4: Sulfur capturing test carried out on the sample of Fig. 1. The overlapped three curves show the sulfur capturing of the same material after a regeneration cycle.

Functionality tests on the developed filters

To test the functionality of nano-coated filters with mercury, a test setup including Hg vaporization, a gas diluter, filter holders, and gas path switch valves have been designed (Fig. 5). A typical Hg concentration in flue gas of coal power plants is

$30 \mu\text{g}/\text{m}^3$ [3]. As the vaporization kinetics of mercury may be too slow to achieve saturated Hg atmosphere at 20 °C in a reasonable time, the vaporization should be performed at elevated temperature. The desired saturation concentration at 20 °C will then be achieved by re-condensation of excess vapor. To include any influence of the filter holders and uncoated filter material on Hg content, two identical filter holders for a coated and uncoated filter are provided. This method allows measuring the difference between both filtering materials. The filter holders are maintained at 220 °C and directly connected to the ICP-OES.

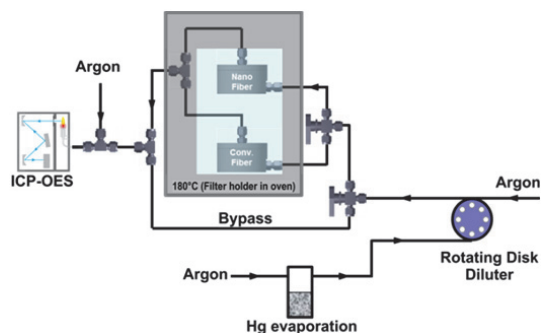


Fig. 5: Schematic test set up for nanofiber filters for removal of Hg from an argon carrier gas.

Conclusions and Outlook

In the first year of the NANOFIL project, novel nanofiber materials able to remove heavy metals (e.g., Hg) were prepared. Chelating groups and CeO_2 nanoparticles were used to specifically bind S. For the production of the final functionalized fiber material, direct deposition or electrospinning can be utilized. Preliminary results on the activity of CeO_2 as sorbent material for S were obtained. The produced materials are under functional characterization and the synthesis processes under optimization. In the second year of this project, the evaluation of the filters will be performed by using an in-house testing setup coupled to ICP-OES. Furthermore, an in-house developed hyphenated SMPS-ICPMS setup (CCMX "NanoAir" Project) can be used to obtain online and simultaneous elemental and size-resolved information of aerosols loaded with metallic particles. Studies on the strategies to regenerate the active materials are also planned. In the future the developed nano-filtering systems should then be tested for other toxic heavy metals in a real flue gas.

References for Project A9.6:

- [1] Zhou J. et al., Environ Sci Technol. 2013; 47:10056-10062
- [2] Adrian H. et al., A hyphenated SMPS-ICPMS coupling setup: Size-resolved element specific analysis of air-borne nanoparticles, submitted to "Journal of Aerosol Science"
- [3] R. H. Ahrens, "EU will Quecksilber Emissionen aus Kohlekraftwerken begrenzen", VDI Nachrichten Nr. 15/16, (11. April 2014)

Simulations and fabrication of novel 4H-SiC nano-trench MOSFET devices

Project A9.7 NanoSiCTrenchFet (CSEM SA Muttenz, PSI, University of Basel, ABB Switzerland Ltd. Baden-Dättwil)
 Project Leader: M. Schnieper
 Collaborators: H. R. Rossmann, F. Zanella, N. Marjanović, M. Schnieper, T. A. Jung, E. Meyer, J. Gobrecht, R. A. Minamisawa, H. Bartolf

Introduction

The two main figures of merit of power semiconductor devices are (i) a high blocking capability, and (ii) a low ON-state resistance when the device is operated under forward bias conditions. Silicon super-junction devices could improve the trade-off between these two figures of merit beyond the so-called unipolar silicon limit. On the one hand, this is a highly costly process (trench-etching and epitaxial-refill processes [1]) and it remains limited by the intrinsic material properties of silicon. On the other hand, wide band gap materials have superior material properties [2] and are suitable for power semiconductor applications. The development of SiC-based unipolar power devices (e.g. planar MOSFETs and Schottky-diodes) was additionally motivated by higher critical electric field (almost an order of magnitude) and the high thermal conductivity compared to silicon. Their fundamental building block is the 4H-SiC crystal-polytype which exhibits the highest bulk mobility and offers the most mature epitaxial growth and processing technology beside the aforementioned advantages.

The performance of current planar SiC MOSFET devices suffers from relatively poor channel-mobilities. They are significantly reduced compared to the bulk value due to scattering processes at the 4H-SiC/insulator interface. Furthermore, the parasitic junction-FET resistance R_{JFET} (as shown in Fig. 1) causes an increasing conduction loss when the device is operated in forward direction.

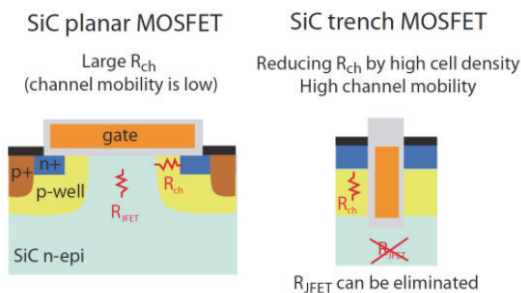


Fig. 1: Schematic view of the planar and trench MOSFET cross-sections with the corresponding resistance components for each of the microscopic device cell-architectures.

In contrast, the channel, accumulation and drift-region resistance components of the U-shape trench-gate MOSFET architecture (UMOSFET) are well established in silicon technology. Thus, this architecture benefits from a reduction in cell pitch

size and from the complete elimination of the junction-FET resistance [3].

Hence, the combination of the superior material properties of 4H-SiC together with the advantages of the UMOSFET design is the topic of investigation in this project. This will offer a unique potential for the next generation of power semiconductor devices. In the first year of the project, the focus was set on device simulation and trench fabrication, both reported here.

Device performance simulations

Simulated transconductance curves have been used to benchmark our trench designs against the planar designs in terms of channel-mobilities. This numerical comparison was performed under the constraint of avoiding localized peaks of the electric field distribution during the reverse bias operation of the device. Field-crowding at the anode-areas would lead to a premature breakdown of the device already at low voltages applied in the blocking direction. This undesired effect can be circumvented by the introduction of rounded trench corners at the bottom of the trench. Additional boundary conditions on the trench geometry were set by our lithographic and manufacturing tools. For our numerical simulations we therefore varied the trench widths from 500 nm up to 3 μm while we kept the trench depth constant at 3 μm .

To simulate transport properties occurring in three-terminal MOS devices, a 50 nm thin insulating layer and a highly-doped-gate were added. The p -type doping concentration of our SiC-epitaxial-layer was 10^{16} cm^{-3} . Dopant concentrations in the drain and source areas were a few orders of magnitude higher.

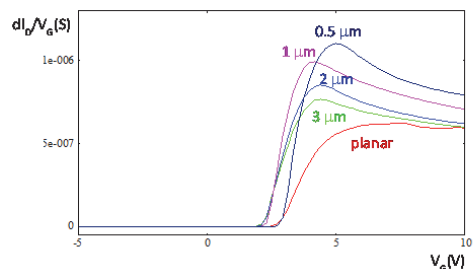


Fig. 2: Comparison of the transconductance curves for different trench widths benchmarked against a planar SiC MOSFET.

Fig. 2 shows the dI/dV_G curves for different trench widths $w_t=500 \text{ nm}$, 1 μm , 2 μm and 3 μm . It can be

seen that the transconductance of the devices clearly depends on the width of the structures and is found to be optimal for the smallest trench width of 500 nm. Furthermore, the trench MOSFET design benefits from a threshold voltage shift towards lower gate voltages. A similar effect could also be achieved by reducing the thickness of the gate insulator [4]. The channel mobilities, which are directly proportional to the $dI/dV-V_G$ signal, therefore increase for decreasing trench widths. It can be concluded that the power losses in the ON-state may be reduced by the utilization of a trench MOSFET design as compared to the planar devices. The origin of the better performance of the nano trenches is finally related to the physics of the channel mobility. The bulk mobility of 4H-SiC(0001) is $950 \text{ cm}^2/\text{Vs}$, but the channel-mobility is drastically reduced due to a number of scattering mechanisms at the 4H-SiC/insulator interface. The mobility of SiC-MOSFETs is reduced by impurity scattering, as well as acoustic phonon scattering and by a high surface roughness. Mainly a high electrical field perpendicular to the 4H-SiC/insulator interface limits the device performance.

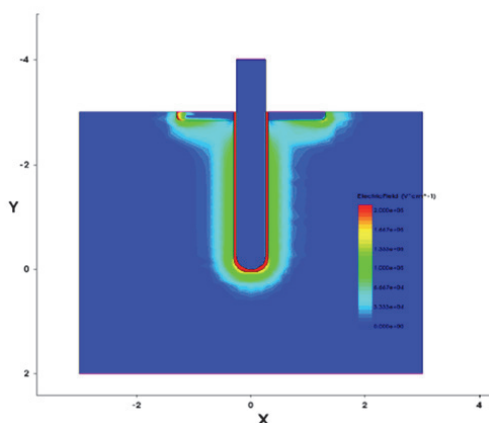


Fig. 3: Electric field distribution for the 500 nm wide trench at 6.3 V gate voltage. At the corners of the source wells and the trench the electric field gets reduced compared to a homogeneous field distribution for planar devices.

As shown in Fig. 3, it is found that the trenches have, as compared to planar devices, reduced electrical fields in the vicinity of the drain and source regions, thus leading to an improvement of the channel mobility and transconduction as determined by our numerical simulations.

Dry-etching of 4H-SiC trenches

For inductively-coupled plasma (ICP) etching of 3 μm deep trenches in 4H-SiC, special test structures for chip sizes of 10 mm x 11 mm have been designed and fabricated by electron-beam lithography. As a hard mask material, chromium has been chosen since it can easily be deposited by electron-beam evaporation and because it offers a high enough selectivity to etch 3 μm deep trenches. The fabrication consisted of the following process sequence: Electron-beam evaporation of 100 nm of Cr, spin coating of 270 nm PMMA (950k 4 %) on top

of the hard mask, electron-beam writing of the trench test structures into the PMMA layer, PMMA development, selective opening of the Cr hard mask by a reactive ion-etching (RIE) process using a plasma consisting of a Cl_2/O_2 gas mixture.

As a starting point for the ICP dry-etching a SF_6 -based process has been used whose parameters have been optimized according to a recent result by J. Biscarrat et al. [5]. This process was able to etch high aspect ratio trenches into 4H-SiC without any microtrenching effects. Furthermore, almost vertical sidewalls with sufficiently high etching rates could be achieved (Fig. 4).

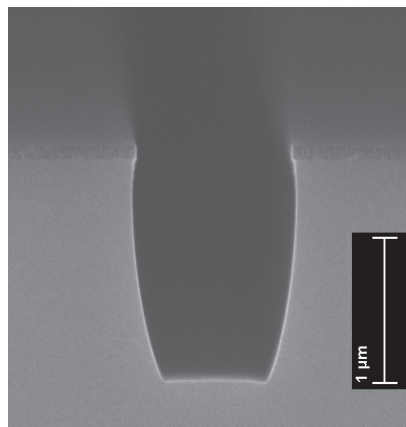


Fig. 4: SEM cross sectional view of the etched trench profile of the 1 μm wide trench.

Conclusion

Our numerical simulations clearly show that the U-shaped trench MOSFET is able to outperform planar MOSFETs.

Regarding the fabrication, we have shown that Cr is suitable as a hard mask material to etch microtrenching-free high-aspect-ratio trenches. Additionally, our process is able to reach almost perfect vertical sidewalls which support high mobilities along the channel.

The project will continue in 2015 toward the fabrication of 4H-SiC Nano Trench MOSFET.

References for Project A9.7:

- [1] H. Bartolf et al., IEEE Transactions on Semiconductor Manufacturing, 26, 4, 529 (2013)
- [2] M. Östling, Proc. 23rd Int. Symp. Power Semicond. Devices ICs, 10 (2011)
- [3] J. Baglia, Fundamentals of Power Semiconductor Devices, Springer, New York, USA (2008)
- [4] H. R. Rossmann et al., submitted to Microelectron. Eng. (2014).
- [5] J. Biscarrat et al., Materials Science Forum Vols. 740-742, 825 (2013)

NANOzyme: Nanobiocatalysts based on artificial metalloenzymes

Project A9.9 NANOzyme: (FHNW, University of Basel, INOFEA GmbH Basel)

Project Leader: P. Shahgaldian (FHNW)

Collaborators: P. Corvini (FHNW), T. Ward, Martina Hesticová (Uni Basel), A. Cumbo (INOFEA GmbH Basel)

Introduction

Catalysis plays a crucial role in synthetic organic chemistry^[1]. Given this importance, a wide range of different systems, such as organocatalysts, heterogeneous solids, metal complexes and enzymes, have been implemented. Transition metal catalysts and enzymes possess complementary properties that can be combined towards the synthesis of enantiopure high-added value products^[2].

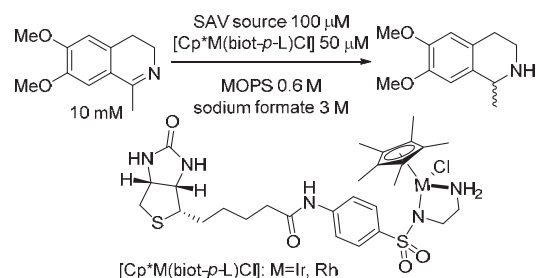
An artificial metalloenzyme (ArM) is created upon non-covalent incorporation of an organometallic cofactor within a host protein^[3]. A versatile system based on the biotin-streptavidin technology combines enzymatic and organometallic catalysis under near physiological conditions. With the aim of immobilizing artificial transfer hydrogenase (ATHase) on silica nanoparticles (SNP) and performing NAD⁺ regeneration *in situ*, we have selected the enantioselective transfer hydrogenation of cyclic imines catalyzed by biotinylated pianostool iridium and rhodium complexes as a model reaction^[4].

Results and discussion

Initial experiments were performed on 1-phenyl-3,4-dihydroisoquinoline (PDQ), using a biotinylated iridium or rhodium cofactor combined with 23 different streptavidin (SAV) isoforms mutated at positions S112 and/or K121. The rhodium catalyst did not perform as well as the iridium-based catalyst, and was thus not further investigated. Subsequently, we screened the reduction of 6,7-dimethoxy-1-methyl-3,4-dihydroisoquinoline (the salsolidine precursor), in the presence of 8 SAV mutants. The streptavidin host protein was used as purified protein, cell free extract (CFE) or cell lysate (CL) respectively.

The selected results are summarized in Fig. 1. Best results were achieved with S112A and S112A-K121A ((*R*)-selective); and S112K and K121A ((*S*)-selective) mutants. These were subsequently selected for immobilization within SNPs. The lyophilized SAV isoforms were dissolved in water and pre-incubated with the biotinylated iridium cofactor for one hour. The solutions were then lyophilized to obtain the functional artificial metalloenzymes. The

most promising ArMs were embedded within a protective organosilica layer (Fig. 2) in collaboration with the group of Professor Shahgaldian.



Entry	M in cofactor	SAV isoform	ee (%)	Conv. (%)	TON
1	Rh	S112A	74	77	154
2		S112K	-31	20	40
3		S112A	81	89	178
4		S112K	-39	39	78
5	Ir	S112A-K121A	57	99	200
6		K121A	-30	98	199
7		S112A + GSH ^a	86	60	120
8		S112K + GSH ^a	-40	11	22
9		S112A CFE ^b	90	81	162
10		S112K CFE ^b	-51	17	34
11		S112A CL ^c	88	59	118
12		S112K CL ^c	-64	19	38

Fig. 1: ATHase of Salsolidine precursor. Reactions were performed using ^apurified proteins spiked with GSH and 2.5 mM CuSO₄, ^bCell free extracts spiked with 5 mM CuSO₄, ^cCell lysate spiked with 7.5 mM CuSO₄.

The activity of ArMs-functionalized nanoparticles towards NAD⁺ regeneration and transfer hydrogenation of the salsolidine precursor was determined. Gratifyingly, the activity of the SNPs for NAD⁺ reduction is retained.

The results of ATHase of the salsolidine precursor are collected in Figure 3. Reduction using Cp*Ir S112A yielded a total TON of 19,724 after 2 days. The immobilized Cp*Ir S112A-K121A yielded even better results, with TON approaching 30,000 (i.e. full conversion) after 3 days. Complete conversion with other mutants was reached after 7 days. Despite the very high activity, a slight erosion in enantioselectivity was observed.

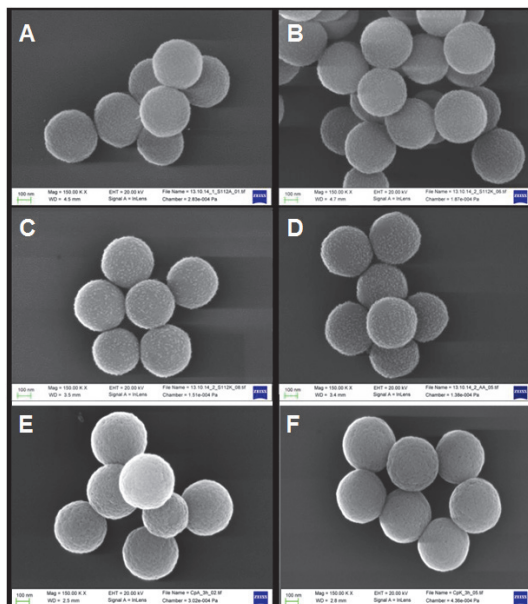


Fig. 2: Scanning electron micrographs of the SNPs. A: S112A; B: S112K; C: Cp*Ir K121A; D: Cp*Ir S112A-K121A; E: Cp*Ir S112A; F: Cp*Ir S112K.

Next, the protective role of the SNPs against cellular debris was investigated. For this purpose, immobilized ATHase SNPs were tested in the presence of empty vector cell free extract to mimic a cellular environment. Up to 1000 TON with Cp*Ir S112A and 300 TON by using Cp*Ir S112K was achieved. In the former case however, the salsolidine product was racemic.

entry	SNP	reaction time	ee (%)	Conv. (%)	TON
1	Cp*Ir S112A	1	53	46	13949
2		2	53	66	19724
3		3	51	62	18661
4		7	50	93	27991
5	Cp*Ir S112K	1	-43	6	1909
6		2	-40	8	2378
7		3	-40	7	2201
8		7	-34	22	6917
9	Cp*Ir K121A	1	-13	54	16242
10		2	-12	76	22964
11		3	-26	99	29692
12		7	-11	96	28778
13	Cp*Ir S112A-K121A	1	9	98	29369
14		2	5	96	28977
15		3	3	100	29988
16		7	0	100	30025
17	Cp*Ir S112A + empty vector CFE	1	1	3	993
18	Cp*Ir S112K + empty vector CFE	1	-65	1	321
19	S112A + Ir	2	20	1	189
20	S112K + Ir	2	-60	1	248

Fig. 3: Asymmetric transfer hydrogenation of the salsolidine precursor (30 mg SNPs/100 μ l reaction mixture).

To test whether the biotinylated Ir-cofactor can diffuse into the silica shell, the SNPs containing only the SAV isoform (no metal cofactor) were mixed with the iridium cofactor. Following this procedure, up to 200 TON for both SAV isoforms were obtained, thus demonstrating the ability of the iridium cofactor to diffuse through the protective organosilica layer into the binding pocket of SAV.

We have also performed experiments to determine recyclability of the SNPs. Each type of catalyst shows 3- to 5-fold decrease of catalytic activity in the terms of conversion, and a marked decrease in selectivity.

Outlook

We have successfully developed an artificial biocatalyst consisting of a pnanostool iridium cofactor within SAV immobilized in SNPs. These nanoparticles display remarkable catalytic activity with TON > 30,000 under optimized conditions.

Next steps include optimization of recyclability, enhancement of enantioselectivity, and engineering enzyme cascades incorporating natural and artificial metalloenzymes.

References for project A9.9:

- [1] F. Swiegers, "Mechanical catalysis: Methods of enzymatic, homogenous, and heterogeneous catalysis", Jon Wiley and sons: New York (2008).
- [2] J.C. Lewis, "Artificial metalloenzymes and metalloprotein catalysts for organic synthesis", ACS Catal. 3, 2954 (2013).
- [3] T.R.Ward, "Artificial metalloenzymes based on the biotin-avidin technology: enantio-selective catalysis and beyond", Acc. Chem. Res. 44, 47 (2011).
- [4] M. Dürrenberger, T. Heinisch, Y. M. Wilson, T. Rossel, E. Noguiera, L. Knör, A. Mutschler, K. Kersten, M. J. Zimbron, J. Pieron, T. Schirmer, T. R. Ward, "Artificial transfer hydrogenases for the enantioselective reduction of cyclic imines", Angew. Chem. Int. Ed., 50 (2011).

Targeting selective cell response by topographical structuring of resorbable polymer implants

Project A9.10 PATCELL (FHNW, PSI, Synthes GmbH Oberdorf)

Project Leader: P. M. Kristiansen

Collaborators: C. Rytka, S. Neuhaus, U. Bruggisser (FHNW-INKA), J. Köser (FHNW-ICB), J. Lungershausen*, R. Holtz (FHNW-IPPE), V. Guzenko (PSI), Oliver Schneider*, S. Beck (Synthes GmbH)

* former team members (JL now at LASAG, OS now at Biotronik)

Motivation

Beneath a number of other factors, the surface properties of a biomaterial are responsible for its acceptance in a host tissue. An implant surface tailored to better interact and to attract the favored cellular tissue, e.g. a bony or a soft tissue, will more easily integrate into the host tissue. A better assimilated biomaterial is generally considered to be more successful and allows for an uneventful use according to its application. This is especially true for resorbable polymer implants.

For this purpose, the effect of surface structuring on different length scales on the cell response to such topographically modified polymer implant materials is investigated.

Master and mold insert manufacturing

A large variety of master structures covering the feature size range from 300 nm to 100 μm were manufactured for screening purposes. This involved *photolithography* for the preparation of binary gratings, pillar arrays and more complex patterns in the size range of 1-10 μm with varying depth, the use of *Talbot displacement lithography* for creation of large area nanopillar arrays, as well as *pulsed laser ablation* to produce semi-spherical holes and posts in the size range of 10-100 μm with variation of diameter, height and period. Full topographical analysis of all master structures was carried out by means of laser scanning confocal microscopy (LSCM) and atomic force microscopy (AFM) for submicron-sized surface patterns.

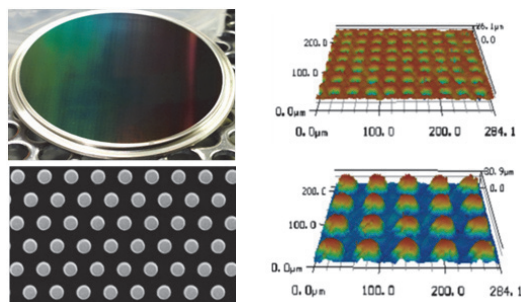


Fig. 1: Examples of master structures and mold inserts (from left to right): a) Nickel mold ($\varnothing = 45 \text{ mm}$, 300 nm pillars, period 600 nm) prepared from a silicon master structured by Talbot displacement lithography (SEM picture shown underneath), b) laser scanning confocal micrographs of mold insert structured by pulsed laser ablation (top) and of replica prepared by injection compression molding (bottom).

Surface structuring of polymers

Master structures with features $< 10 \mu\text{m}$ were successfully replicated into 250 μm films of PLGA by *hot embossing* and fully characterized by LSCM. Comparison of the topographical characterization of master and replica, respectively, revealed that high fidelity replication was achieved.

Laser machined mold inserts made of stainless steel were used to replicate circular pillar structures ($\varnothing = 10\text{-}100 \mu\text{m}$; height = half diameter and varying distances between the pillars) into PLGA plaques by *injection compression molding*. Topography analysis by means of LSCM revealed high fidelity replication and a high level of reproducibility also for the injection compression molding process.

Substrate wettability

The influence of surface patterns on the wettability of substrates was thoroughly characterized revealing distinct differences in the wettability, particularly for structural features in the size range 1-10 μm , whereas surface patterning with larger feature dimensions did not result in substantial changes in the wettability.

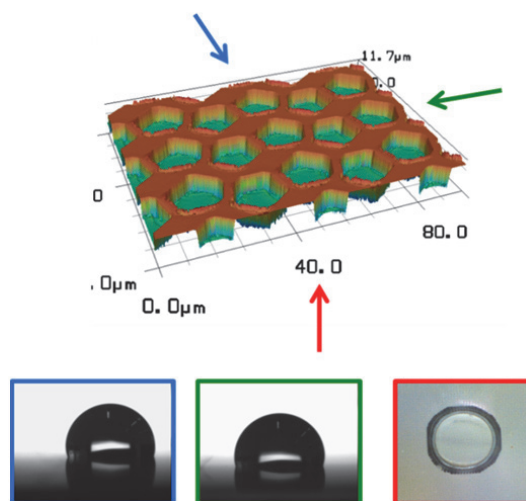


Fig. 2: Wettability of microstructured PLGA films exemplified for one particular surface structure. The water contact angle was determined along different directions of the surface pattern (laser scanning confocal micrographs displayed on top) as indicated by blue and green arrows. In addition, the water drop footprint (red box) was determined to judge the anisotropy of wetting.

Temperature and hydrolytic stability

Sufficient thermal and hydrolytic stability was demonstrated for virtually all surface patterns. Only minor geometrical variations were observed after exposure to application-relevant treatments.

It could be shown that most surface patterns displayed < 10 % reduction in structure height after short-term immersion in hot water (used in clinical application to render the implant deformable). Also, storage of the structured samples in phosphate buffered saline (PBS) solution at room temperature overnight showed similar or even smaller changes.

Cell response to structured surfaces

Different cell lines have different characteristics and may, thus, display variable response to patterned polymer samples. The following cell lines were initially chosen for cell response testing throughout the present project:

Osteoblasts:

- i) *MG63* (human, sarcoma),
- ii) *MC3T3-E1 subclone4* (mouse, preosteoblast)

Fibroblasts:

- i) *NIH3T3* (mouse, embryonal fibroblast)
- ii) *L-M(TK-)* (mouse, subcutan. connective tissue)
- iii) *rat2* (rat, fibroblast)

Although it is at present too early to draw definite conclusions, some important findings were discovered throughout the first year of the project:

- The *surface coverage and morphology* of osteoblasts showed strong dependencies on the underlying surface patterns.
- *Alignment of cells* was observed for a series of surface topographies in the 1-10 μm size range. Whether this alignment has positive or negative effects on the cell proliferation still needs to be investigated.
- *Surface pattern depth* was decisive on whether cells remained on top of the structures (structure depths of 2 μm and less) or "squeezed" between structural features (frequently observed for structure depths of 5 μm and more)
- Some surface patterns displayed substantial reduction in the number of osteoblast cells attached. These findings need to be confirmed for fibroblasts, for which this effect would be desired.

Complementary to the above findings, several methodologies were developed to optimize the investigations of cell response to different surface patterns, i.e. staining of nuclei for more accurate determination of surface coverage, and actin filament staining for visualization of cytoskeleton and quantification of the number of cell attachment points.

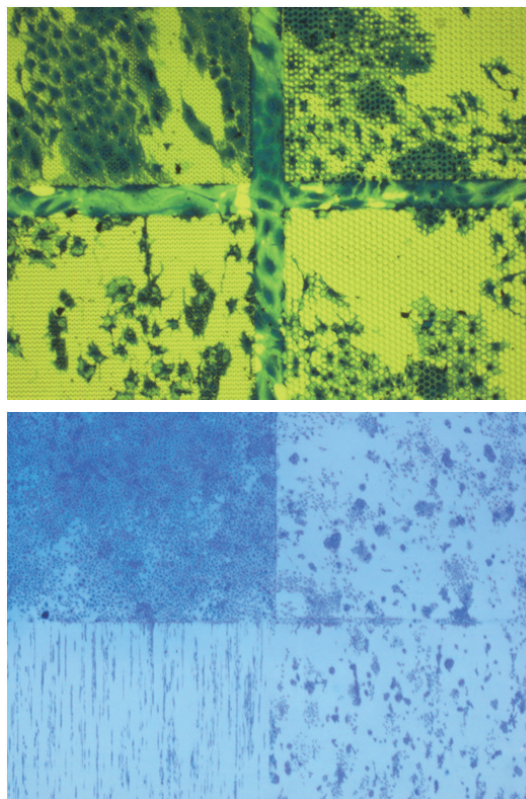


Fig. 3: Variation in cell response of osteoblasts (here *MC3T3*) to different surface patterns, observed in phase contrast microscopy (top) and optical microscopy (bottom) after staining with Comassie blue. Specification of the underlying surface patterns is avoided upon request of the industry partner.

Conclusions and Outlook

A large variety of surface structured PLGA films were successfully prepared throughout the first year of the project. The largest potential for industrial scale-up is expected for laser manufactured surface structures. Additionally, conventional surface structuring techniques will be investigated.

Preliminary findings in context with cell response to structured PLGA surfaces were obtained mainly with osteoblast cells (*MC3T3*). Cell response testing is being extended to other cell lines as indicated in the previous section.

References for Project A9.10

- [1] P.M. Kristiansen, "Targeting selective cell response through topographical surface structuring of resorbable polymer implants", invited talk at the SNI annual meeting, Lenzerheide, Sept. 11-12, 2014.

Single-cell nanoanalytics

Project A9.12 SCeNA (University of Basel, FHNW, F. Hoffmann-La Roche AG Basel)

Project Leader: T. Braun

Collaborators: Hans-Peter Lang (SNI), Götz Schlotterbeck (FHNW), Gregor Dernick (Roche)

Introduction

Biological cells are the basic building-blocks of life. Their phenotype is formed by stochastic protein-interaction networks within the cell's genetic predisposition (Fig. 1). Classical methods study these interaction networks examining populations of cells, normally in the order of 10^6 cells per experiment. However, these bulk analyses interfere with the stochastic nature of biological interaction networks, also known as “biological noise”: (i) Rare network paths are diluted below the detection limits of the employed analysis methods; (ii) similar interaction paths lead to overlapping signals and are averaged. These barriers can be overcome by performing the analysis on single-cell level.

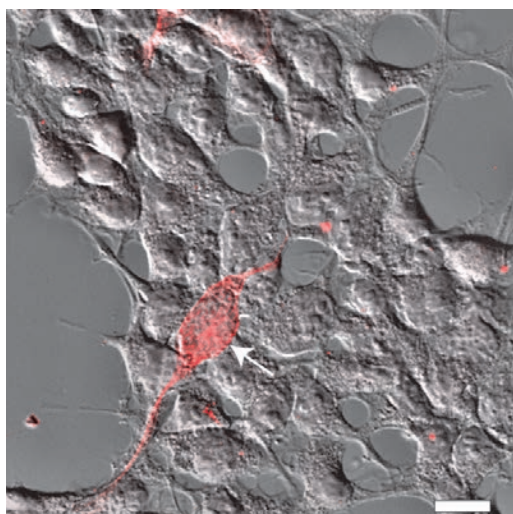


Fig. 1: Typical example of “biological noise”. Wild-type HEK-293 cells were visualized in light microscopy (LM). Differential interference contrast (DIC) LM is overlaid with the immunofluorescence labeling of tubulin-Beta-III channel (red). Around 2 % of the cells started to express tubulin-Beta-III (white arrow), a typical differentiation marker for neuronal cells. Note that it is a genetically identical clone and all cells were treated the same. Tubulin-Beta-III expressing cells and “normal” cells exhibit the same shape and grow behavior than the others and grow only few μm apart. Scale bar: 10 μm .

The specific aim of the SCeNA project is to combine a cell culturing and single-cell lysis device with various bioanalysis methods that characterize different aspects of the cell status (Fig. 2): (A) label and amplification free transcriptomics using nanomechanical viscosity sensors; (B) protein detection by enhanced reverse phase protein microarrays; (C) visual proteomics by visually analyzing the cytosolic proteins using high-speed atomic force microscopy; (D) metabolomics by mass spectrometry.

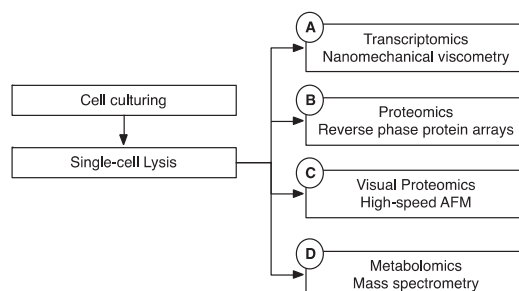


Fig. 2: Different single-cell analysis modules of the SCeNA project. A single-cell culturing and lysis device allows the growth of eukaryotic cells and their observation by live cell imaging. At specific time-points, the cells are lysed (picked) and transferred to a microfluidic system for further processing and/or conditioning. Hand-over-systems to the different analysis modules A-D are currently developed.

Single-cell lysis and handling platform

We developed a second generation cell-culturing and single-cell harvesting device (Fig. 3), based on the technology developed before [1]. Adherent eukaryotic cells are grown on functionalized interfaces and microstructures (see also project P1201, p. 2). An individual cell can be targeted in the light-microscope (Fig. 3 A1) and lysed by electroporation and simultaneous aspiration of the cell contents (Fig. 3 A2). Subsequently, the cell content can be condi-

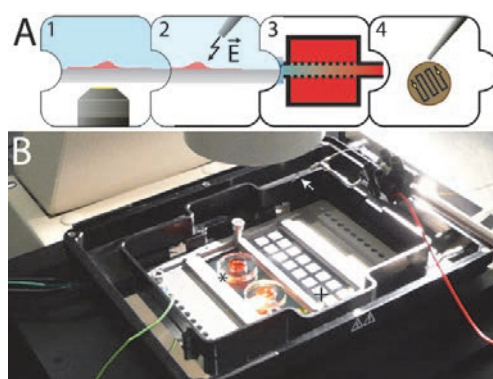


Fig. 3: The single-cell cultivation, lysis and sample preparation platform. A) Microfluidic pipeline for cell conditioning and hand-over. (1) Live cell imaging of adherent cells. (2) Cell lysis by electroporation and simultaneous aspiration. (3) Sample conditioning. (4) Hand-over, e.g., onto electron-microscopy grids for subsequent analysis by “single-cell visual proteomics” as shown before project start [1]. B) Cell incubation chamber for long term cell-cultivation. Adherent eukaryotic cells are grown in miniaturized cell-culturing plates (*) and monitored by time-lapse LM. The nozzle (arrow) is used for the lysis of individual cells by electroporation with simultaneous aspiration into the microcapillary (Volume: ~ 5 nL) as well as to dispense the conditioned sample onto carriers, e.g., nitrocellulose pads for reverse phase protein arrays (+).

tioned (Fig. 3 A3) and dispensed by a hand-over mechanism for later analysis. Conditioning and hand-over depend on the chosen analysis method (modules A-D, Fig. 2). The entire setup can be automated using the openBEB scripting language [2].

Single-cell visual proteomics by EM

An example of single-cell lysis, conditioning and analysis by visual proteomics [1] is shown in Fig. 4. An individual cell (HEK-293) was lysed, conditioned with heavy metal salt and dispensed on an EM grid [1]. Subsequently, the cell lysate was imaged in the transmission EM. Large structures can be recognized by eye, such as actin filaments or vaults. In this project, we will employ high-speed AFM instead of EM for visualization.

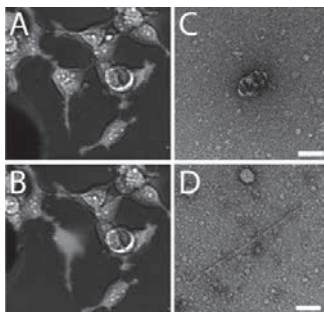


Fig. 4: Lysis of an individual cell and analysis by "single-cell visual proteomics" by EM [1]. A&B) Single-cell lysis. Cell before (A) and after lysis (B). Scale bar: 50 μm . C&D) The cell lysate was conditioned by desalting and staining in heavy metal salt by a micro-dialysis conditioning module (see Fig. 3 A3). Inspection in transmission EM revealed typical cytosolic structures, such as vaults (C) or actin filaments (D). Scale bars: 50 nm.

Single-cell reverse-phase protein arrays

In reverse phase protein arrays (RPPA) entire sets of complex biological samples, e.g., cell lysates, are immobilized on a surface as spots and then probed by specific antibodies for particular proteins (Fig. 5). Only a very small amount of sample is needed, e.g., the lysate of an individual cell. The small amount of samples deposited also allows the creation of many copies of a sample. In this way, the relative abundance of several proteins in a large number of samples can be probed in one experiment. RPPA complements other techniques, such as the

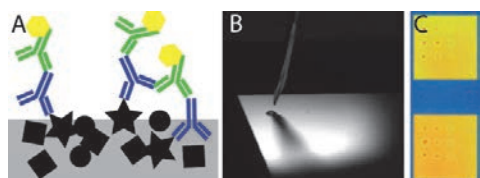


Fig. 5: Reverse phase protein arrays. A) Principles: The cell lysate proteins (black) are dispensed onto a nitrocellulose pad (gray) and dried. Subsequently, the pad is incubated with a primary antibody (blue), which itself is recognized by a fluorescence labeled (yellow) secondary antibody (green). B) Lysis nozzle dispensing a 5 nl droplet on the pad. C) Fluorescence image of disposed cell lysate droplets after processing the nitrocellulose slide.

enzyme-linked immunosorbent assay (ELISA), and has achieved sensitivities that allow the detection of a particular protein in samples containing only the equivalent of half a cell or less (data not shown).

To test the performance of the single-cell lysis set-up, we compared the RPPA signal of actin (an abundant house-keeping protein) of individually lysed cells with the signal of dilution series of batch-lysed cells (Fig. 6). The signal of the individually lysed cells exhibits a linear response, and extrapolation of the line well describes the signal of batch lysed cells, before signal saturation is observed. This demonstrates the efficiency of the single-cell lysis procedure and sample uptake, as well as the linear response of the RPPA method.

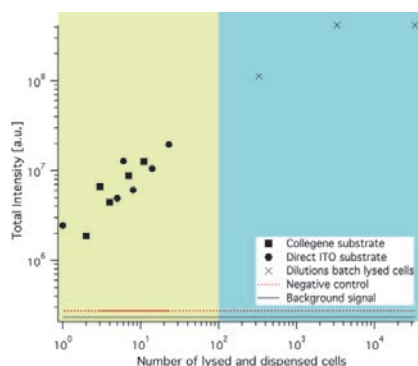


Fig. 6: Reverse phase protein array repeatedly spotted by the single-cell lysis set-up. Individual cells were lysed and dispensed as spots on a nitrocellulose pad (green area, dots and squares). Alternatively, cells were grown in flasks, detached from their substrate, counted, lysed and dispensed (blue area, crosses). After incubation with an anti-actin antibody and a fluorescently labeled secondary antibody the slide was scanned. The total fluorescence intensity was plotted against the number of lysed cells dispensed in each spot [1].

Outlook

Currently, sample conditioning and hand-over systems are developed for high-speed AFM (visual proteomics), mass spectrometry (metabolomics) and nanomechanical viscometry (transcriptomics). The RPPA hand-over is further optimized and less abundant protein detection and sample splitting of individual cells is tested.

Involved scientists: Stefan Arnold, Andrej Bieri, Benjamin Bircher, Philipp Fischer, Rosmarie Sütterlin (C-CINA, Biozentrum); François Huber (SNI); Christian Berchtold (FHNW).

References for Project A9.12:

- [1] Arnold SA and Kemmerling S, et al., "Single-cell lysis for visual analysis by electron microscopy". *J Struct Biol.* 2013; 183(3): 467–73.
- [2] Ramakrishnan C, et al., "openBEB: open biological experiment browser for correlative measurements". *BMC Bioinformatics.* 2014; 15(1): 1–14.

SINAPIS – Slurry injection of nano-scale particles into implant surfaces

Project A9.15 SINAPIS (FHNW, University of Basel, WATERjet Robotics AG Oftringen)

Project Leader: R. Schumacher

Collaborators: A.M. Rohner, A. Melzner, M. de Wild, O. Braissant, M. Straubhaar

Introduction

Total hip and knee arthroplasties are considered as key treatments in medical technology with more than 200'000 hip replacements implanted in Germany every year. The number of implanted artificial joints is increasing while the age of patients is decreasing. Therefore, it has become necessary to increase the implant's lifetime of currently 15 to 20 years and to further improve anchoring in the bone.

On one hand, research is focusing on the contact between implant and bone and attempts to maximize the fixation by applying open porous surface structures for better bone attachment. On the other hand, research is addressing the decrease of wear of the articulating surfaces which are made of plastics such as UHMW-PE, ceramics such as Al_2O_3 or metals such as CoCrMo in various combinations and with varying success. The latter goal is the main topic of this very ambitious and innovative research project.

Material and Methods

In this project, we are aiming for the structuring and functionalization of surfaces of implants, respectively their articulating areas, by mechanical treatment and incorporation of nanoparticles into the implant material. For these purposes, we are using a novel implant surface treating process provided and operated by our industry partner. This process uses a low-pressure liquid forming a suspension to functionalize surfaces of implant materials (Fig. 1).

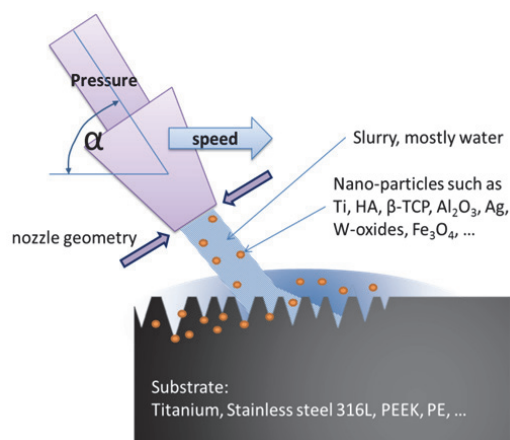


Fig. 1: Scheme of slurry injection process.

As a first step, we investigate the ability of structuring biomaterials such as titanium grade 5, PEEK and also PE. We are using small specimens of 14 mm in diameter and 1 mm in thickness. All titanium specimen surfaces are treated with a standardized electro-polishing method which provides a very fine and constant surface roughness.

In a second step we investigate the incorporation of biologically interesting nano-scale particles into the implant material. As an example we used hydroxyapatite HA, Al_2O_3 and other small items with potentially positive effects on implant surfaces.

Before treating sample surfaces were analysed their roughness and their morphology. For the tactile roughness measurement, the Rugosurf G90 was used. To analyse the surface structure and evaluate if particles could be deposited in the material or on the surface, SEM/EDX analysis were performed. For SEM/EDX analysis, the Hitachi TM-1000 with a back-scattered electron detector was used.

Results

This project was initiated one year ago, and initial results already show some promising effects. This new slurry injection method could be used for structuring biomaterials in different manner and with potentially different effects.

In the evaluation phase of the relevant process, parameters such as speed of the injection nozzle, selection of the right substrate materials or the choice of slurry medium needed to be investigated with a series of slurry treated samples.

In these first trials we could demonstrate how the carrying medium without any particles have an effect on the surface treatment. We could show that the surface can be structured in a wide range from smooth to rough in dependence within the different adjustable parameters mentioned above. By variation of the injection type, a huge increase of the roughness of Ti samples was achieved.

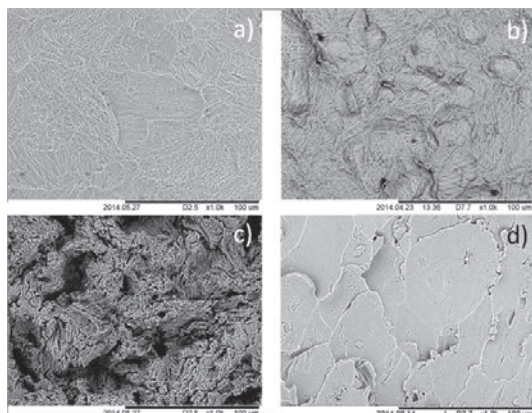


Fig. 2: SEM pictures of Ti samples after the first trial: a) electropolished Ti surface showing smooth topography; b) slurry (without particles) injection structured surface with a little impact on surface roughness; c) slurry (without particles) injection structured surface with clear impact on roughness; d) compacted and flattened Ti surface treated with ZrO_2 under a small angle α

In addition to this, investigations on the deposition of small added particles have shown that at least a certain amount is remaining on the surface of the substrate samples. The structuring of these samples with ZrO_2 showed that we can induce an additional compaction of the surface by depositing particles on the surface. By treating the samples under a small angle α , the surface can be compacted and smoothed at the same time (Fig. 2 (b)).

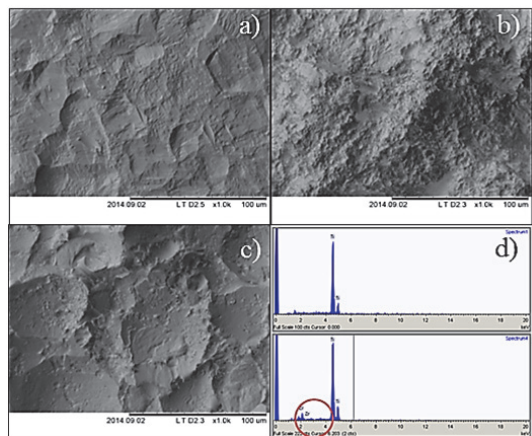


Fig. 3: SEM pictures of Ti samples and EDX spectrum to analyse elemental composition: a) electropolished Ti surface showing smooth topography b) slurry injection structured Ti surface with clear impact on surface roughness; c) Zr particles doped and slurry injected Ti surface; d) EDX spectrum of sample c, showing a clear deposition of Zr particles on the surface.

The analysis of injection-treated polymers has shown that the elasticity of substrate material has a significant effect on the structuring of the substrate

for depositing particles on the surface. By analogy with this effect, for Ti samples it could be determined that the choice of other parameters changes the surface structuring significantly. However, the surface of the treated polymers is flat in the beginning and is more and more frayed by increasing the structuring conditions. It has been found that it is easier to deposit particles on surfaces of denser and stiffer polymers than on more elastic ones.

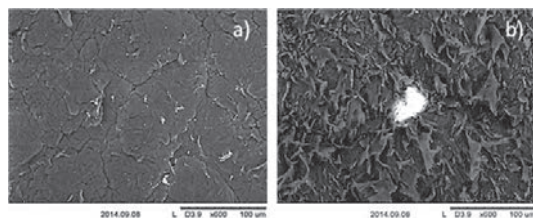


Fig. 4: SEM pictures of polymer samples after treatment with ZrO_2 slurry: a) smooth polymer surface structured with ZrO_2 under subtle structuring conditions; b) rough polymer surface after structuring with intense structuring conditions.

Up to now, the amount of deposited particles, their size and how the surface structure of the different substrates looks like, could be controlled along with some trials. Overall, we can say that, independent on the particle material itself, spherical particles have the potential to compact the substrate surface and sharp-edged particles are more abrasive.

Discussion

By adapting the process parameters, the roughness as well as the morphology of the sample surface could be adjusted. The structured area is always processed homogeneously while, at higher pressure, a mechanical damage of the surrounding area by bounced particles was observed. It is still a challenge to evaluate what the effect of a chosen particle on the surface is and which parameters are needed, because for every particle and every substrate material combination, specific process parameters need to be evaluated.

Until now, not all mutual dependencies are evaluated and understood in detail, but the relevant process parameters are identified.

Within the next studies, we will analyse how the particles are anchored in the substrates. Additionally, the biological effects of such treated surfaces will be investigated along with cell adhesion, proliferation as well as cell differentiation test series.

References for Project A9.15:

- [1] Ralf Schumacher, A.M. Rohner, A. Melzner, M. de Wild, O. Braissant, "SINAPIS - Slurry Injection of Nano-scale Particles into Implant Surfaces" SNI Annual Meeting, Lenzerheide, Switzerland, 2014



**Educating
Talents**
since 1460.

Universität Basel
Petersplatz 1
Postfach 2148
4001 Basel
Switzerland
www.unibas.ch